FULLY NONLINEAR WAVE-BODY INTERACTIONS BY A 2D POTENTIAL NUMERICAL WAVE TANK

A Dissertation

by

WEONCHEOL KOO

Submitted to the Office of Graduate Studies of
Texas A&M University
in partial fulfillment of the requirements for the degree of

DOCTOR OF PHILOSOPHY

August 2003

Major Subject: Ocean Engineering

FULLY NONLINEAR WAVE-BODY INTERACTIONS BY A 2D POTENTIAL NUMERICAL WAVE TANK

A Dissertation

by

WEONCHEOL KOO

Submitted to Texas A&M University
in partial fulfillment of the requirements
for the degree of

DOCTOR OF PHILOSOPHY

Approved as to style and content by:

Moo-Hyun Kim
(Chair of Committee)

Cheung Hun Kim
(Member)

Jun Zhang
(Member)

Robert O. Reid
(Member)

Paul N. Roschke
(Head of Department)

August 2003

Major Subject: Ocean Engineering

ABSTRACT

Fully Nonlinear Wave-Body Interactions by
A 2D Potential Numerical Wave Tank. (August 2003)
Weoncheol Koo, B.S., Seoul National University, Korea;
M.S., Texas A&M University
Chair of Advisory Committee: Dr. Moo-Hyun Kim

A 2D fully nonlinear Numerical Wave Tank (NWT) is developed based on the potential theory, mixed Eulerian-Lagrangian (MEL) time marching scheme, and boundary element method (BEM). Nonlinear Wave deformation and wave forces on stationary and freely floating bodies are calculated using the NWT. For verification, the computed mean, 1st, 2nd, and 3rd order wave forces on a single submerged cylinder are compared with those of Chaplin's experiment, Ogilvie's 2nd-order theory, and other nonlinear computation called high-order spectral method. Similar calculations for dual submerged cylinders are also conducted. The developed fully nonlinear NWT is also applied to the calculations of the nonlinear pressure and force of surface piercing barge type structures and these obtained results agree with experimental and theoretical results. Nonlinear waves generated by prescribed body motions, such as wedge type wave maker or land sliding in the coastal slope area, can also be simulated by the developed NWT. The generated waves are in agreement with published experimental and numerical results. Added mass and damping coefficients can also be calculated from the simulation in time domain. For the simulation of freely floating barge-type structure, only fully nonlinear time-stepping scheme can accurately produce nonlinear body motions with large floating body simulations. The acceleration potential method, which was developed by Tanizawa (1996), is known to be the most accurate, consistent and stable. Using acceleration potential method, in the present study, the series of motions and drift forces were calculated over a wide range of incident wave frequencies including resonance region. To guarantitatively compare the nonlinear contribution of free-surface and body-boundary conditions, the body-nonlinear-only case with linearized free-surface condition is separately simulated. All the floating body motions and forces are in agreement with experimental results. Finally, the NWT is extended to fully nonlinear wave-body-current interactions of freely floating bodies, which has not been published in the open literature until now.

ACKNOWLEDGMENTS

First of all, I wish to thank God for his continuous help and support.

I would like to give my sincere gratitude to my advisor Dr. Moo-Hyun Kim for the guidance, inspiration, assistance and supervision he has shown in helping me complete this research. The patience and encouragement when various problems occurred, are much appreciated. I also want to thank Dr. Cheung Hun Kim, Dr. Jun Zhang and Professor Robert O. Reid for their helpful advice and willingness to serve on my advisory committee. I offer my thanks to all other faculty members and students in the ocean engineering program for being good friends.

I owe a debt of deep gratitude to my family; my wife Dawoon Jung, my son Chang-hyun and my daughter Ja-hyun. I also give my deep appreciation to my parents. Without their love, sacrifice, constant support and prayer, I could never have come this far.

TABLE OF CONTENTS

CHAPTER

Page

LIST OF FIGURES

FIGURE Page

FIGURE Page

FIGURE Page

FIGURE Page

FIGURE Page

FIGURE Page

FIGURE Page

LIST OF TABLES

TABLE Page

CHAPTER I

INTRODUCTION

1.1. Background

It is of great interest to investigate nonlinear wave-body interactions in various ocean engineering projects. Recently, many floating vessels and production units have been used for oil and gas exploration and production. In addition to it, barge-type structure has been utilized extensively to transport industrial product and material. A number of researchers and scientists have studied the interaction of wave and barge-type structures such as stationary or forced motion structures. These studies are useful for calculating wave loads and radiation damping on a body. However, to analyze real situations like floating barge-type structure with incoming waves, freely floating body simulation should be considered.

The complete study of freely floating body motion induced by incoming waves is not yet popular, because of the complexity involved in solving motion equation and fluid particle movement simultaneously. Most of the works have been simplified, even if the floating body analyses have been published. Only a few authors have done a 2D freely floating body simulation.

In this research, a 2D fully nonlinear Numerical Wave Tank (NWT) is utilized to analyze nonlinear wave-body interactions. The NWT is developed on the basis of potential theory, mixed Eulerian-Lagrangian (MEL) time marching scheme, and boundary element method (BEM). For fully nonlinear time domain simulation, Runge-Kutta 4th order (RK4) time marching is used. In order to calculate wave force on a floating body, acceleration potential method was used for obtaining the time derivative of velocity potential on a body.

This Dissertation follows the style and format of *Journal of Fluid Mechanics*.

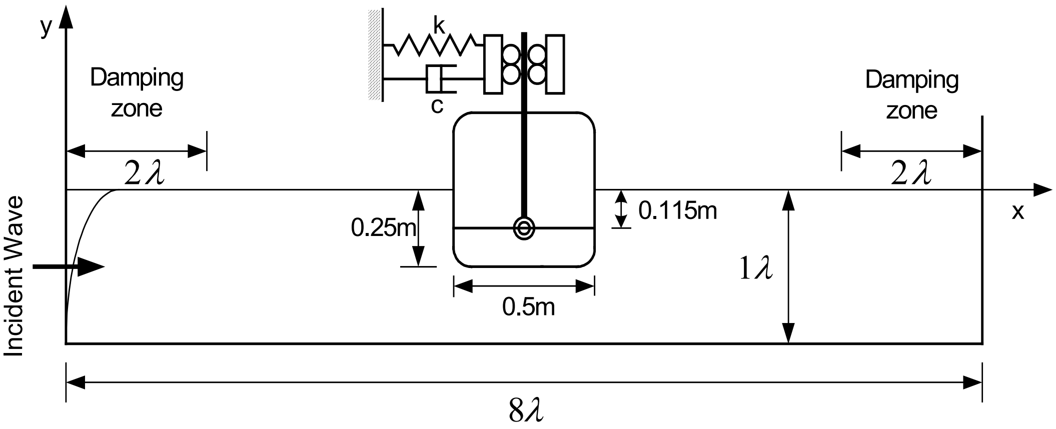

Figure 1. Plan view of a 2D Numerical Wave Tank for floating body simulation

1.2. Literature review

A variety of NWT schemes have been developed for nonlinear waves, wave forces, and motions of floating structures. Several authors have published numerical calculations and available schemes for freely floating body motion analysis. Figure 1 shows the view of 2D NWT for floating body simulation.

For the floating-body motion, ϕ_t has to be obtained correctly in order to calculate body force. The simplest way is to use backward finite difference scheme in time. However, the scheme is inherently unstable. An alternative to the scheme is to solve the boundary value problem for the ϕ_t, which was first introduced by Vinje and Brevig (1981). Vinge et. al. decomposed the acceleration field into 4 modes corresponding to the unit acceleration of 3 body motions such as sway, heave, and roll and centripetal-like acceleration coming from velocity field. Having decomposed the acceleration field into 4 modes, they solved the boundary value problem corresponding to each mode.

Tanizawa and Sawada (1990) proposed a more rational method to solve motion equation and water particle movement simultaneously in the acceleration fields. They introduced an 'implicit boundary condition' derived from the kinematic boundary condition of the body and motion equations. They further showed that simultaneous equations of ideal fluid and floating body motions could be solved without decomposition. Tanizawa (1995, 1996) introduced the nonlinear acceleration potential and derived the exact body boundary condition for the acceleration field. Using the exact body boundary conditions, he simulated free vertical motion (heave) in a closed domain. The confirmed simulated wave field well satisfies with conservation laws of volume, momentum and energy.

Cointe et. al (1990) simulated the linear and nonlinear motions of a barge-type structure in a 2D NWT. The computational domain had a numerical beach and a wave maker absorber. The authors damped the reflected wave from the floating body before the waves could reach the wavemaker.

Sen (1993) computed ship motion in waves in a fully nonlinear method. He used a semi-lagrangian approach for simulating free surface and Orlanski radiation boundary condition. He encountered numerical instabilities, so called saw-tooth instabilities, in the area of wavemaker-free surface and wave-body surface. He found that the use of backward finite difference scheme for the time derivative of velocity potential (ϕ_t) is the main source of error for divergence. To overcome the instabilities, iterative way of finite difference method for obtaining ϕ_t was used.

Contento (1996) simulated the 2D ship motions in his NWT. The procedure employs a flap-type wavemaker, the Orlanski open-boundary condition, a semi-Lagrangian scheme, and a long wave tank to avoid undesirable reflection. The ϕ_t was obtained from the computation of the material derivative of velocity potential.

Tanizawa and Naito (1997) studied the parametric roll motion of a ship in NWT. The NWT developed by Tanizawa (1995, 1996), employing MEL procedure, a piston-type wavemaker, absorbing beach and wavemaker absorber. The paper did not have the saw-tooth instability. They found qualitative and quantitative agreements with their experiments.

Wu and Eatock-Taylor (1996) proposed a new technique to solve the velocity and acceleration field simultaneously instead of computing velocity and acceleration field separately. Kashiwagi (1998) called this method as new indirect method and used it in the 2D NWT. The merit of this method lies in computing motion faster than that of Tanizawa, While the disadvantage of this method is that it cannot compute the wave pressure on a body surface.

To obtain floating body boundary condition for acceleration field, four methods have been developed. These methods are summarized once again; iterative method by Sen (1993) and Cao et. al. (1994), mode decomposition method by Vinge and Brevig (1981) and Cointe et. al.(1990), indirect method by Kashiwagi et. al. (1998), and implicit boundary method by Tanizawa (1995). Other research and development works for NWT are well described by Kim. et. al. (1999).

For saving computational effort, the frozen coefficient method, which uses frozen influence matrix for updating internal RK4 step, can be used and its validity has made been for forced body motion and fixed structure (Ferrant, 1998). However, for the freely floating body motion simulation, influence matrix should be updated in the internal RK4 step during time marching. Comparison of these two methods is demonstrated and explained in this study.

1.3. Organization

In Chapter II, the boundary value problem for the wave-body-current interaction has been formulated. Full descriptions of each boundary conditions including fully nonlinear free surface boundary conditions, body boundary conditions, input boundary, and rigid boundaries on entire domain are made. Boundary integral equation and its procedure of solving with matrix form are also presented and explained.

In Chapter III, all the numerical procedures used in the computer program are discussed in sequence. The detailed procedures for fully nonlinear NWT and time-domain simulation are presented. The concept and numerical implementation of the acceleration potential method is also discussed.

In Chapter IV, Numerical results for the several applications are presented. Nonlinear wave generation and propagation with finite depth are shown and compared with experimental results. Wave deformation and force for fully submerged single and dual cylinders are computed. A series of force components for surface piercing fixed single/dual barge-type structures are computed and their interactions with waves are also considered. Freely floating barge motions and forces on the body are presented and compared with experimental results. Large motions of floating body due to resonance wave frequency are investigated. Free surface elevations near the body are also shown. Long wave generation due to land sliding is computed and motion of sliding mass is described. Finally, freely floating body motions and forces induced by wave and current are newly calculated and their phenomena are described.

CHAPTER II

MATHEMATICAL FORMULATION

2.1. Boundary-value problem

2.1.1. Governing equation

An ideal fluid is assumed so that the fluid velocity can be described by the gradient of velocity potential ϕ. A Cartesian coordinate system is chosen such that the z=0 corresponds to the calm water level and z is positive upwards. Then the governing equation of the velocity potential is given by

$$\nabla^2\phi = 0 \qquad \text{in the fluid domain} \tag{1}$$

2.1.2. Free surface boundary conditions

- Fully nonlinear dynamic free surface condition can be written as

$$\frac{\partial \phi}{\partial t} = -g\eta - \frac{1}{2}\left|\nabla\phi\right|^2 - \frac{P_a}{\rho} \tag{2}$$

where P_a is the pressure on the free surface, and is assumed to be zero from now on.

- Fully nonlinear kinematic free surface condition can be written as

$$\frac{\partial \eta}{\partial t} = -\nabla\phi \cdot \nabla\eta + \frac{\partial \phi}{\partial z} \tag{3}$$

Both dynamic and kinematic free surface boundary conditions are satisfied on the exact free surface.

2.1.3. Input boundary conditions

At the inflow boundary, a theoretical particle velocity profile along the vertical input boundary is fed in this paper. The exact velocity profile of a true nonlinear wave under the given condition is not known a priori. Therefore, the best thing we can do is to input the best theoretical wave along the input boundary. Since the fully nonlinear free-surface condition is applied in the computational domain, the input wave immediately takes the feature of fully nonlinear waves. However, the mismatch between input velocity profiles and real water particle velocity causes unnecessary spurious waves (e.g. 2nd order free waves) inside the domain.

For example, when a linear or 2nd-order Stokes regular waves are prescribed, the following equations are used.

$$\begin{aligned}\frac{\partial\phi}{\partial n} &= n_x\frac{\partial\phi}{\partial x} = n_x\frac{gAk}{\omega}\frac{\cosh k(z+h)}{\cosh kh}\cos(kx-\omega t)\ \text{(Linear)}\\ &+n_x\frac{3}{8}A^2\omega(2k)\frac{\cosh 2k(z+h)}{\sinh^4 kh}\cos 2(kx-\omega t)\ \text{(Stokes' 2nd)}\end{aligned} \tag{4}$$

where *A, w, k,* and *h* are wave amplitude, frequency, wave number, and water depth respectively.

2.1.4. Rigid boundary conditions

No normal-flux condition is applied on rigid cylinders, bottom, and at the vertical end-wall of numerical beach.

$$\frac{\partial\phi}{\partial n} = 0 \tag{5}$$

2.1.5. Body boundary conditions

The body boundary condition is written as

$$\frac{\partial\phi}{\partial n} = V\cdot n \tag{6}$$

where, V and n are body velocity with respect to body center (i.e. gravity center) and body surface normal vector respectively.

- **Fixed (not moving) body case**

When the body does not move, i.e. the body velocity is zero, the condition of body surface is rigid boundary. Therefore, the body boundary condition is $\frac{\partial\phi}{\partial n} = V\cdot n = 0$

- **Floating (moving) body case**

If the body is not stationary, body boundary condition should be updated during the time simulation. There are two kinds of moving body. One is a prescribed body motion and the other is a floating body motion induced by incident waves. A prescribed motion means that we forced the body to move with prescribed velocity, which is so called radiation problem for calculating added mass and radiation damping coefficients. We can design body velocity and motion amplitude depending on situations. Therefore, body velocity is known and is fed on the body boundary condition at every time step.

Freely floating body motion is the body motion induced by incoming waves so that body velocity should be calculated every time step. The calculation of body velocity is obtained by solving equation of motion. Body acceleration can be obtained after wave force on the body surface has been solved. Body velocity is calculated by integrating body acceleration. The details of numerical procedure are described in Chapter III.

2.2. Steady current problem

For surface wave propagation problem with a steady uniform current along with x location, the total velocity, which includes current effect in the entire fluid, can be expressed as

$$\tilde{\phi} = U_0 x + \phi(x,z,t) \tag{7}$$

where, the steady uniform current U_0 and total potential $\tilde{\phi}$ satisfy the Laplace equation.

The entire boundary can be expressed by either total potential $\tilde{\phi}$ or ϕ. For convenience in the present study, all boundary conditions may be described by ϕ.

Body boundary condition is given by

$$\frac{\partial \tilde{\phi}}{\partial n} = \frac{\partial (U_0 x + \phi)}{\partial n} = V \cdot n \quad \text{and} \quad \frac{\partial \phi}{\partial n} = V \cdot n - U_0 \frac{\partial x}{\partial n} \tag{8}$$

On the rigid boundary, no flux condition is applied and written as

$$\frac{\partial\tilde{\phi}}{\partial n}=\frac{\partial(U_0x+\phi)}{\partial n}=U_0\frac{\partial x}{\partial n} \quad \text{and} \quad \frac{\partial\phi}{\partial n}=0 \tag{9}$$

For the Input boundary, incident wave profiles are distributed in the vertical direction.

$$\frac{\partial\tilde{\phi}}{\partial n}=\frac{\partial(U_0x+\phi)}{\partial n}=U_0\frac{\partial x}{\partial n}+\frac{\partial\phi_w}{\partial n} \quad \text{and} \quad \frac{\partial\phi}{\partial n}=\frac{\partial\phi_w}{\partial n}=\frac{\partial\phi_w}{\partial x}n_x \tag{10}$$

where, $\phi_w=\frac{gA}{\omega}\frac{\cosh k(z+h)}{\cosh kh}\sin(kx-\omega t)$ is incident velocity potential, k should be obtained by new dispersion relation, $(\omega-kU_0)^2=gk\tanh kh$.

On the free surface, kinematic free surface condition is described as

$$\frac{\partial\eta}{\partial t}=\frac{\partial\tilde{\phi}}{\partial z}-\nabla\tilde{\phi}\cdot\nabla\eta=\frac{\partial\phi}{\partial z}-\nabla\phi\cdot\nabla\eta-U_0\frac{\partial\eta}{\partial x} \tag{11}$$

and the dynamic free surface condition is

$$\frac{\partial\tilde{\phi}}{\partial t}=-g\eta-\frac{1}{2}\left|\nabla\tilde{\phi}\right|^2-\frac{P_a}{\rho}$$

$$\frac{1}{2}\left|\nabla\tilde{\phi}\right|^2=\frac{1}{2}\left|\nabla\phi\right|^2+U_0\frac{\partial\phi}{\partial x}+\frac{1}{2}{U_0}^2$$

$$\frac{\partial\phi}{\partial t}=-g\eta-\frac{1}{2}\left|\nabla\phi\right|^2-U_0\frac{\partial\phi}{\partial x}-\frac{1}{2}{U_0}^2 \tag{12}$$

2.3. Boundary integral equation

At each time step, the velocity potential and the corresponding free surface profiles are obtained by solving the discretized form of the following integral equation.

$$\alpha\phi_i=\iint_{\Omega}(G_{ij}\frac{\partial\phi_j}{\partial n}-\phi_j\frac{\partial G_{ij}}{\partial n})ds \tag{13}$$

where, G is the Green function satisfying Laplace equation and α is a solid angle (α =0.5 when singularities are on the boundary). For two-dimensional problems, the simple source G is given by

$$G(x,z,x_i,z_i)=\ln R_1 \tag{14}$$

where, R_1 is the distance between the source (x_i, z_i) and the field points (x, z) (Brebbia and Dominguez, 1992).

The integrals are calculated by 4-point Gaussian quadrature method and the discretized form of the boundary integral equation is given by

$$\frac{1}{2}\phi_i + \sum_{j=1}^{N} \hat{H}_{ij}\phi_j = \sum_{j=1}^{N} G_{ij} \frac{\partial \phi_j}{\partial n} \tag{15}$$

Let H_{ij} be denoted as

$$H_{ij} = \begin{cases} \hat{H}_{ij} & \text{when } i \neq j \\ \hat{H}_{ij} + \frac{1}{2} & \text{when } i = j \end{cases} \tag{16}$$

The entire set of equations for each discretized segment can be simplified by following the matrix form.

$$\sum_{j=1}^{N} H_{ij}\phi_j = \sum_{j=1}^{N} G_{ij} \frac{\partial \phi_j}{\partial n} \tag{17}$$

Each boundary condition can be expressed by either ϕ or ϕ_n and employed in equation (17). After employing all boundary conditions, ϕ or ϕ_n is known and the other variables are unknown which can be determined by solving equation (17). For instance, on the body surface, boundary condition is expressed by ϕ_n and the solution of equation (17) is ϕ. In order to solve the equation, H and G matrix should be rearranged by sorting the known terms and unknown terms. On passing all the known terms to the right-hand side and the unknown terms to the left-hand side, the matrix form can be written as

$$HX = GF \tag{18}$$

where, H, G are the rearranged H_{ij} and G_{ij} matrices, X, F are the matrix form of unknown terms and known terms respectively.

Finally, we can obtain X by multiplying the inverted H matrix with GF matrix form.

$$X = H^{-1}GF \tag{19}$$

Note that the inverting calculation of H matrix is the most time-consuming procedure for solving boundary integral equation. However, computer power has greatly increased since two decades and thus the matrix inversion has become faster.

CHAPTER III

NUMERICAL METHODS

3.1. Mixed Eulerian-Lagrangian (MEL)

In order to represent free surface elevation with distributed nodes on the boundary, Mixed Eulerian-Lagrangian method (MEL) is employed. The use of fully nonlinear, free-surface time-stepping method for 2D waves by MEL technique was first introduced by Longuet Higgins and Cokelet (1976). The time marching scheme requires at each time step the following procedure: (i) solving the Laplace equation in the Eulerian frame, and (ii) updating the moving boundary points and values in Lagrangian manner. Total derivative is used for free surface boundary condition and is written as $\frac{\delta}{\delta t}=\frac{\partial}{\partial t}+\vec{v}\cdot\nabla$

Considering $\frac{\delta}{\delta t}=\frac{\partial}{\partial t}+\vec{v}\cdot\nabla$, the fully nonlinear free-surface conditions can be modified in the Lagrangian frame as follows

$$\frac{\delta\phi}{\delta t}=-g\eta-\frac{1}{2}\left|\nabla\phi\right|^{2}+\nabla\phi\cdot\vec{v} \tag{20}$$

$$\frac{\delta\eta}{\delta t}=\frac{\partial\phi}{\partial z}-(\nabla\phi-\vec{v})\cdot\nabla\eta \tag{21}$$

where, v and η are node velocity and surface elevation respectively.

Two MEL methods have been developed so far. One of the method is material node approach and the other is semi-lagrangian method.

3.1.1. Material node approach

In material node approach, the nodes or collocation points on the free surface follow the individual water particle velocity, i.e. $v=\nabla\phi$, where node velocity (v) is the same as water particle velocity ($\nabla\phi$). Therefore, nonlinear free surface boundary conditions are written as

$$\frac{\delta\phi}{\delta t} = -g\eta + \frac{1}{2}\left|\nabla\phi\right|^2 \tag{22}$$

$$\frac{\delta\eta}{\delta t} = \frac{\partial\phi}{\partial z} \tag{23}$$

Equation (23) is the vertical movement of free surface node. Total movement of nodes is described by

$$\frac{\delta\vec{x}}{\delta t} = \nabla\phi \tag{24}$$

where, $\vec{x}$ is node location (x, z)

From equation (22) and (24), free surface boundary conditions become very simple. But the nodes should be rearranged after several time steps but should not be filed up, which is called regriding. For convenience and better numerical stability of this study, regriding process is executed for every time step.

3.1.2. Semi-Lagrangian method

If the node has prescribed motion, we call it semi-lagrangian method. Most common prescribed motion, for instance, is when node moves only in the vertical direction regardless of horizontal movement of water particles, i.e. nodal velocity $\vec{v} = (0, \frac{\delta\eta}{\delta t})$. Free surface boundary conditions (equation 2, 3) are thus modified as follows

$$\frac{\delta\phi}{\delta t} = -g\eta - \frac{1}{2}\left|\nabla\phi\right|^2 + \frac{\partial\phi}{\partial z}\frac{\delta\eta}{\delta t} \tag{25}$$

$$\frac{\delta\eta}{\delta t} = \frac{\partial\phi}{\partial z} - \frac{\partial\phi}{\partial x}\frac{\partial\eta}{\partial x} - \frac{\partial\phi}{\partial y}\frac{\partial\eta}{\partial y} \tag{26}$$

Compared to material node approach, modified free surface boundary conditions of semi-lagrangian method are complicated but regriding process is not required.

Depending on the problem, either material node approach or semi-lagrangian method is easier to apply. For example, material node approach is suitable to use for the freely floating body motion problem because node moves corresponding to the body movement. However, semi-lagrangian method is easily applied for fixed piercing body or fully submerged structures as the computational free surface domain does not change during the simulation.

3.1.3. Steady current case

When a steady current is applied in the entire computational domain, free surface boundary conditions (equation 11 and 12) can be modified by MEL method and can be given as

$$\frac{\delta\eta}{\delta t}=\frac{\partial\phi}{\partial z}+(\upsilon-\nabla\phi)\cdot\nabla\eta-U_0\frac{\partial\eta}{\partial x} \tag{27}$$

$$\frac{\delta\phi}{\delta t}=-g\eta-\frac{1}{2}|\nabla\phi|^2+\upsilon\cdot\nabla\phi-U_0\frac{\partial\phi}{\partial x}-\frac{1}{2}U_0^{\,2} \tag{28}$$

In the present study, material node approach is used for steady current problem ($\upsilon=\nabla\tilde{\phi}$) and the final forms of free surface boundary conditions are

$$\upsilon=\frac{\delta\vec{X}}{\delta t}=\nabla\tilde{\phi}=U_0 i+\nabla\phi \tag{29}$$

Kinematic free surface boundary condition can be simplified in the equation (30) with material node approach and its result supports equation (29).

$$\frac{\delta\eta}{\delta t}=\frac{\partial\phi}{\partial z}+(\nabla\tilde{\phi}-\nabla\phi)\cdot\nabla\eta-U_0\frac{\partial\eta}{\partial x}=\frac{\partial\phi}{\partial z} \tag{30}$$

Dynamic free surface boundary condition is modified as

$$\begin{aligned}\frac{\delta\phi}{\delta t}&=-g\eta-\frac{1}{2}|\nabla\phi|^2+\nabla\tilde{\phi}\cdot\nabla\phi-U_0\frac{\partial\phi}{\partial x}-\frac{1}{2}U_0^{\,2}\\&=-g\eta+\frac{1}{2}|\nabla\phi|^2-\frac{1}{2}U_0^{\,2}\end{aligned} \tag{31}$$

3.2 Time marching scheme (Runge-Kutta 4th order)

In the MEL method, the value of potential at each time step is given on the free surface and the value of normal derivative of potential is known on the body surface, the rigid bottom and the rigid wall. The free surface potentials and the elevations are determined by integrating the free surface boundary condition with respect to time stepping. This time stepping procedure is called time marching scheme. In this study, Runge-Kutta 4th order scheme as a time marching is used for fully nonlinear simulation. Runge-Kutta 4th order scheme is a sub-step method using mid step value within one time step. This method is the most stable for calculating fully nonlinear simulation.

3.3. Ramp function

When the simulation is started, a ramp-function at the input boundary is applied. The ramp function prevents the impulse-like behavior of wavemaker to reduce the corresponding transient waves. It makes the simulation more stable and reach the steady state earlier. In this paper, the ramp function is applied in 2T or 4T (wave period) depending on input wave height. Ramp function is given by

$$r(t) = \begin{cases} 1 & \text{, for t > 2T} \\ \{1 - \cos(\pi \frac{t}{2T})\}/2 & \text{, for t} \le \text{2T} \end{cases} \tag{32}$$

3.4. Numerical beach (Artificial damping zone)

Towards the end of the computational domain, an artificial damping zone was applied so that the wave energy is gradually dissipated in the direction of wave propagation. The profile and magnitude of the artificial damping has to be designed to minimize the possible wave reflection at the entrance of the damping zone and to maximize wave energy dissipation. After comprehensive tests, the length of the damping zone (l_d) was determined to be at least 2 wavelengths. In general, longer l_d is needed for highly nonlinear waves. In this paper, both ϕ_n & η-type damping terms were added to the fully-nonlinear dynamic and kinematic free-surface conditions.

$$\frac{\delta\phi}{\delta t} = -g\eta + \frac{1}{2}\left|\nabla\phi\right|^2 + \mu_1\frac{\partial\phi}{\partial n} \tag{33}$$

$$\frac{\delta\eta}{\delta t} = \frac{\partial\phi}{\partial z} + \mu_2\eta \tag{34}$$

where, $\mu_i = \begin{cases} \mu_{0i}[1-\cos\{\frac{\pi}{2}\left(\frac{x-l}{l_d}\right)\}] & \text{for x} > l \\ 0 & \text{for x} \le l \end{cases}$

l is the length of computational domain (no damping zone) and l_d is the length of damping zone.

The damping is designed to grow gradually to the target constant value to minimize wave reflection against the entrance of the damping zone. Through linear stability analysis, the target value (optimized damping coefficient) was obtained (i.e. $\mu_{01} = 1.5$ and $\mu_{02} = k\mu_{01}$), which minimizes the dispersion error at the discontinuity (entrance of damping zone). The performance and efficiency of the artificial damping coefficients used was numerically tested and confirmed.

3.5. Damping for incident wave zone

When long time simulations are required and a body is present causing reflected waves, re-reflection from the wave maker have to be controlled and eliminated to best represent the open sea condition. When simulating the physical wave tank, the same phenomenon (re-reflection) by the wave maker occurs and no control is needed. In the present study, a special damping scheme in front of the wave maker is employed to prevent the re-reflection from the wave maker. This damping scheme has to be designed to damp not the incident waves but the reflected waves.

$$\frac{\delta\phi}{\delta t} = -g\eta + \frac{1}{2}\left|\nabla\phi\right|^2 + \mu_1\left(\frac{\partial\phi}{\partial n} - \frac{\partial\phi}{\partial n}*\right) \tag{35}$$

$$\frac{\delta\eta}{\delta t} = \frac{\partial\phi}{\partial z} + \mu_2(\eta - \eta*) \tag{36}$$

where, $$\mu_i = \begin{cases} \mu_{01}[1-\cos\{\frac{\pi}{2}\left(\frac{l-x}{l_d}\right)\} & \text{for x } \le l \\ 0 & \text{for x } > l \end{cases}$$

$\frac{\partial \phi}{\partial n}*$, $\eta*$ are the solutions in the absence of bodies. l is the length of computational domain (no damping zone) and l_d is the length of damping zone.

The reference values of $\frac{\partial \phi}{\partial n}*$ and $\eta*$ can be computed by the same computational condition under no body assumption. When the incident waves are moderately nonlinear and computational efficiency is of concern, proper analytic solutions (e.g. 2nd order stokes wave in case of nonlinear simulation) can be used. In the present study, 2nd-order Stokes' waves are used for $\frac{\partial \phi}{\partial n}*$ and $\eta*$, and the efficiency is also tested. For the practical purpose, even the linear analytic solution can be used. Tanizawa (1997) showed that linear analytic solution works even for higher wave steepness. The shape of the artificial damping in front of the wave maker is similar to that of the damping zone by the same performance consideration. Only the direction of growth is opposite since reflected waves from the body have to be eliminated.

3.6. Smoothing scheme

It is well known that the so-called saw-tooth instability may occur on the free surface during the simulation of highly nonlinear waves. It is caused either by variable mesh size/high-order aliasing or inherent singular behavior at the wavemaker and free-surface intersection. To avoid the non-physical saw-tooth numerical problem, a Chebyshev 5-point smoothing scheme was used along the free surface during time marching. The smoothing scheme was applied at every 5 time step. It is confirmed that the smoothing scheme has little affect on the higher-order components up to third order. Chebyshev 5-pt smoothing scheme for evenly space node was first introduced by Longuet-Higgins & Cokelet (1976). In this paper, the scheme is modified and extended to variable-node-space cases (Sung, 1999) (See APPENDIX C).

3.7. Time derivative of velocity potential

The accurate calculation of time derivative of velocity potential is very important to obtain correct pressure and force on the body surface. There are several ways to obtain this important value. Backward difference is the simplest way, which subtracts the potential value of previous time step from the present potential value. However, this method is unstable in most cases. The useful methods for nonlinear simulation are finite difference method and usage of acceleration potential.

3.7.1. Finite difference way

Time derivative of velocity potential can be obtained by using sub step values of velocity potential in a time step. A special form of finite difference formula developed by Hong and Kim (1999) is used. This formula utilizes the mid-step values of the present time marching scheme (Runge Kutta 4th order) as follows:

$$\frac{\delta\phi(t_0+\Delta t)}{\delta t}=\frac{1}{4\Delta t}\left(10\phi(t_0+\Delta t)-2\phi(t_0)-4\phi^{(1)}(t_0+\frac{\Delta t}{2})-4\phi^{(2)}(t_0+\frac{\Delta t}{2})\right)-\frac{1}{2}\frac{\delta\phi(t_0)}{\delta t} \tag{37}$$

where, superscripts (1) and (2) denote the first and second mid-step in Runge-Kutta 4th scheme, respectively.

This finite difference formula is good for surface piecing fixed structure and force motion body. In case of freely floating body induced by incoming waves, the finite difference way is not valid because the time derivative of velocity potential should be obtained at the same time as the moving body. For freely floating body motion, the usage of acceleration potential is the solution for calculation of time derivative of velocity potential.

3.7.2. Usage of acceleration potential

The gradient of the acceleration potential is defined as acceleration like the gradient of velocity potential represents velocity. Using the acceleration potential, the time derivative of velocity potential can be obtained directly from boundary integral equation. Although many methods have been developed so far, acceleration potential method has been known to be the most accurate and consistent way to obtain time derivative of velocity potential for the floating body motion. To calculate floating body motion, the equation of fluid particle and body motion should be solved simultaneously. The details of the acceleration potential are explained in Chapter 3.11.

3.8. Pressure on the instantaneous wetted surface

After obtaining the time derivative of velocity potential, the nonlinear body pressure can be calculated by using the following Bernoulli's equation:

$$P = -\rho g z - \rho \frac{\partial \phi}{\partial t} - \frac{1}{2} \rho \left| \nabla \phi \right|^2 \tag{38}$$

In MEL method,

$$P = -\rho g z - \rho \frac{\delta \phi}{\delta t} - \frac{1}{2} \rho \left| \nabla \phi \right|^2 + \rho \nabla \phi \cdot \vec{v} \tag{39}$$

where, $\vec{v}$ is node velocity. It can be zero for fully submerged fixed bodies.

3.9. Force on a floating body surface

Wave force on the body surface can be calculated by integrating Bernoulli's pressure over the instantaneous wetted surface. Including gravitational force and horizontal restoring force due to weak spring designed for making the body not to float too much, the total force in the i-th direction can be given as

$$F_i = \int_{S_B} -\rho(\phi_t + \frac{1}{2}\left|\nabla\phi\right|^2 + gz)\cdot n_i ds - kx\delta_{i1} - W\delta_{i2} \tag{40}$$

where, k is spring constant, x is sway motion, W is the weight of body(=mg), and δ_{ij} denotes the Kronecker delta function, equal to 1 when i=j.

3.10. Body nonlinear simulation

To calculate the motion of floating body, there are three methods for employing boundary condition on the entire domain. Linear simulation is the simplest way to obtain the potential on the body and surface elevation. It is assumed that the fluid particle and body motions are sinusoidal so that discretized nodes of entire domain place on the mean position during the simulation, i.e. fixed node. Linear free surface boundary condition is also used for linear simulation. So, the influence matrix should be calculated only once and used it for the entire simulation. For body force calculation, only 1st order term can be considered in this linear simulation.

Fully nonlinear simulation means all boundaries employ nonlinear boundary conditions including body boundary condition. For the free surface, nodes are fluctuating with fluid particles. Free surface nodes and nodes on the body surface are updated corresponding to fluid particles and body motion at every time step. Due to the node fluctuation, the influence matrix has to be calculated every time step and the computational cost is much expensive as compared to the linear one.

Body nonlinear simulation is combined with linear boundary condition. This method can be employed in linear free surface and nonlinear body boundary conditions so that the descretized free surface nodes are stationary and nodes on the body surface are updated every time. The influence matrix has to be obtained at every time step because of moving body nodes even if free surface nodes are not fluctuating. This method can be used for evaluation of nonlinear wave effect against body motion. This simplification may be useful when near the resonance condition and the change of body geometry is significant near the mean position. Because linear waves with nonlinear body boundary condition have been used, we can clearly see the nonlinear wave effect on the floating/moving body as compared with linear wave effect. All the comparison of linear and nonlinear wave effect against body motion will be shown in figure 73-77.

3.11. Acceleration potential

To calculate the time derivative of velocity potential, the acceleration potential method is used in the present study. The acceleration potential means that the fluid particle acceleration can be determined by the gradient of acceleration potential.

$$\vec{a} = \nabla \Phi \tag{41}$$

where, Φ is acceleration potential

whereas, velocity potential is defined as

$$\vec{V} = \nabla \phi \tag{42}$$

The acceleration is the total time derivative of the fluid velocity

$$\vec{a} = \frac{\delta \vec{V}}{\delta t} = \frac{\partial \vec{V}}{\partial t} + \vec{V} \cdot \nabla \vec{V} \tag{43}$$

Combining equations (42) and (43),

$$\vec{a} = \frac{\partial \nabla \phi}{\partial t} + (\nabla \phi \cdot \nabla) \nabla \phi = \nabla \left(\frac{\partial \phi}{\partial t} + \frac{1}{2} |\nabla \phi|^2 \right) \tag{44}$$

Therefore, acceleration potential is defined as

$$\Phi = \frac{\partial \phi}{\partial t} + \frac{1}{2} |\nabla \phi|^2 \tag{45}$$

Note that the acceleration potential does not satisfy Laplace equation ($\nabla^2 \Phi \neq 0$), because of the nonlinear term ($\frac{1}{2} |\nabla \phi|^2$) (Tanizawa, 1995). From the point of view of numerical application, this nonlinear term can be explicitly calculated by the solution of velocity field equation. So, we don't need to solve Φ directly, instead we solve for ϕ_t.

$$\phi_t = \frac{\partial \phi}{\partial t} = \Phi - \frac{1}{2} |\nabla \phi|^2 \tag{46}$$

Then ϕ_t can be solved in the entire fluid domain since ϕ_t satisfies Laplace equation.

3.12. Body boundary condition for acceleration field

The kinematic body boundary conditions for velocity and acceleration potentials are

$$\frac{\partial \phi}{\partial n} = \vec{V} \cdot \vec{n} = \nabla \phi \cdot \vec{n} \tag{47}$$

$$\frac{\partial \Phi}{\partial n} = \vec{a} \cdot \vec{n} = \nabla \Phi \cdot \vec{n} \tag{48}$$

where, $\vec{n} = n_x i + n_z k$ is the unit normal vector of the body surface.

The kinematic boundary condition for the acceleration on the body surface can be described as follows,

$$\frac{\partial \Phi}{\partial n} = \vec{n} \cdot (a_0 + \dot{\omega} \times r) + \vec{n} \cdot \omega \times (\omega \times r) - k_n (\nabla \phi - \upsilon_0 - \omega \times r)^2 + \vec{n} \cdot 2\omega \times (\nabla \phi - \upsilon_0 - \omega \times r) \tag{49}$$

where, a_0, and $\dot{\omega}$ are the translational, and the angular accelerations, υ_0, and ω the translational, and angular velocities of the body respectively. The origin of the motion is set to the center of gravity of the body in the present study. So, these motions are observed with respect to the space-fixed frame at the center of gravity of the body. r is the position vector from the center of gravity of the body to the body surface. k_n is normal curvature of the body surface along the path of fluid ($k_n = -\frac{1}{\rho^*}$, where ρ^* is radius of local center).

First term in equation (49) can be rearranged in the following form, $a_x n_x + a_z n_z + a_5 n_5$, where subscript 5 means roll acceleration and roll normal vector. Other terms can be defined as a q term. Therefore,

$$q = \vec{n} \cdot \omega \times (\omega \times r) - k_n (\nabla \phi - \upsilon_0 - \omega \times r)^2 + \vec{n} \cdot 2\omega \times (\nabla \phi - \upsilon_0 - \omega \times r) \tag{50}$$

From equations (46), (49), and (50), body boundary condition for acceleration field can be expressed as,

$$\frac{\partial \phi_t}{\partial n} = \frac{\partial}{\partial n}\left(\Phi - \frac{1}{2}\left|\nabla \phi\right|^2 \right) = \frac{\partial \Phi}{\partial n} - \frac{\partial}{\partial n}\left(\frac{1}{2}\left|\nabla \phi\right|^2 \right) = \vec{n} \cdot (a_0 + \dot{\omega} \times r) + q - \frac{\partial}{\partial n}\left(\frac{1}{2}\left|\nabla \phi\right|^2 \right) \tag{51}$$

$$\frac{\partial \phi_t}{\partial n} = \vec{n} \cdot (a_0 + \dot{\omega} \times r) + q_B \tag{52}$$

where, $q_B = q - \frac{\partial}{\partial n}\left(\frac{1}{2}|\nabla\phi|^2\right)$

The second term of q_B can then be written as (Tanizawa, 1995)

$$\frac{\partial}{\partial n}\left(\frac{1}{2}|\nabla\phi|^2\right) = -k|\nabla\phi|^2 - \frac{\partial\phi}{\partial n}\left(\frac{\partial^2\phi}{\partial s^2}\right) + \frac{\partial\phi}{\partial s}\frac{\partial}{\partial s}\left(\frac{\partial\phi}{\partial n}\right) \tag{53}$$

where, n and s are normal and tangential direction of unit vector and local curvature along the s direction $k = -\frac{1}{\rho^*}$.

In summary, q_B term can be written for a 2D simulation as

$$\begin{aligned} q_B = {} & n_x(\omega^2 x_P + 2\omega\left(\frac{\partial\phi}{\partial z} - \upsilon_Z\right)) + n_z(\omega^2 z_P - 2\omega\left(\frac{\partial\phi}{\partial x} - \upsilon_X\right)) \\ & - k_n\left[\left(\frac{\partial\phi}{\partial x} - \upsilon_X - \omega z_P\right)^2 + \left(\frac{\partial\phi}{\partial z} - \upsilon_Z + \omega x_P\right)^2\right] \\ & + k_n\left[\left(\frac{\partial\phi}{\partial x}\right)^2 + \left(\frac{\partial\phi}{\partial z}\right)^2\right] + \frac{\partial\phi}{\partial n}\left(\frac{\partial^2\phi}{\partial s^2}\right) - \frac{\partial\phi}{\partial s}\frac{\partial}{\partial s}\left(\frac{\partial\phi}{\partial n}\right) \end{aligned} \tag{54}$$

Therefore, the body boundary condition for acceleration potential field can be described from equation (52) and (54) completely. q_B represents the contribution of the velocity field to the acceleration field and all terms are determined explicitly after velocity field is calculated i.e. ϕ and $\frac{\partial\phi}{\partial n}$ are determined on all boundaries by boundary integral equation.

To calculate acceleration field, all the boundary conditions of boundary integral equation contain time derivative terms i.e. ϕ_t and $\frac{\partial\phi_t}{\partial n}$. The time derivative of velocity potential is obtained by solving the discretized form of the following integral equation.

$$\alpha\phi_{ti} = \iint_{\Omega} (G_{ij}\frac{\partial\phi_{tj}}{\partial n} - \phi_{tj}\frac{\partial G_{ij}}{\partial n})ds \tag{55}$$

where, G is the Green function and α is the solid angle (α =0.5 when singularities are on the boundary)

The time derivative of velocity potential can be obtained by solving implicit loop of acceleration and velocity field equation simultaneously. To calculate this implicit relation, there are several methods developed such as iterative (Cao et. al. (1994), sen, (1993)), mode decomposition (Vinje and Brevig, (1981), Cointe et. al., (1990)), indirect method (Wu & Eatock Taylor, (1996), Kashiwagi, (1998)), and implicit boundary condition method (Tanizawa, (1997)). In the present study, modal decomposition method has been used among these schemes.

3.13. Mode decomposition method

Mode decomposition method was first developed by Vinje and Brevig (1981). They developed 2D Numerical Wave Tank by using complex potential. In their 2D NWT, the acceleration field is decomposed into four modes corresponding to three unit accelerations such as sway, heave, roll and acceleration due to the velocity field. Each mode can be obtained by solving independent boundary integral equation. Using these four modes and motion equation of body, body acceleration can be determined.

The time derivative of velocity potential of the body has the combination of three-unit acceleration field and acceleration due to velocity field.

$$\phi_t = \sum_{i=1}^{3} a_i \varphi_i + \varphi_4 \tag{56}$$

where, a_i is the i th mode component of generalized body acceleration.

Body surface boundary condition for each mode is

$$\frac{\partial \varphi_i}{\partial n} = \left\{ \begin{array}{ll} n_i, & i = 1 \sim 3 \\ q_B, & i = 4 \end{array} \right\} \tag{57}$$

Free surface boundary condition is

$$\varphi_i = \begin{cases} 0, & i = 1 \sim 3 \\ -g\eta - \frac{1}{2}|\nabla\phi|^2, & i = 4 \end{cases} \tag{58}$$

Input boundary condition is

$$\frac{\partial \varphi_i}{\partial n} = \begin{cases} 0, & i = 1 \sim 3 \\ \frac{\partial \phi_t}{\partial n}, & i = 4 \end{cases} \tag{59}$$

Other rigid boundary condition is

$$\frac{\partial \varphi_i}{\partial n} = \{0, \quad i = 1 \sim 4\} \tag{60}$$

After solving the boundary integral equation (55) with those inputs, φ_i (on the body surface), $\frac{\partial \varphi_i}{\partial n}$ (on the free surface), and φ_i (on the rigid boundary) are obtained. Then, the remaining unknown values in the equation (56) are a_i only.

In order to calculate the generalized acceleration for each motion (sway, heave, and roll), wave force equation, which integrate Bernoulli's pressure over the instantaneous wetted surface, should be combined with Newton's 2nd law. Including the gravitational force and horizontal restoring force due to weak spring, which was designed so that the body does not float too much, the total force in the ith direction can be calculated as follows:

$$P = -\rho(a_1\varphi_1 + a_2\varphi_2 + a_3\varphi_3 + \varphi_4 + gz + \frac{1}{2}|\nabla\phi|^2)$$

$$F_x = \int_{S_B} P \cdot n_x ds - kx$$

$$F_z = \int_{S_B} P \cdot n_z ds - W$$

$$M = \int_{S_B} P \cdot n_5 ds \tag{61}$$

$$ma_1 = F_x$$

$$ma_2 = F_z$$

$$ma_3 = M \tag{62}$$

where, k is the spring constant, x is the sway motion and W is the weight of body (=mg)

From equations (61) and (62), we can determine the generalized acceleration of each mode. And equation (56) can be determined completely. After time derivative of velocity potential is obtained from equation (56), the nonlinear wave forces on a body can be obtained by integrating the nonlinear pressure over the instantaneous wetted body surface at each time step.

$$F = \int_{S_B} \rho(-\frac{\partial\phi}{\partial t} - \frac{1}{2}\left|\nabla\phi\right|^2 - gz) \cdot \vec{n}ds \tag{63}$$

where, S_B is body surface

The body acceleration can be obtained either from equation (61) and (62) directly or from equation (62) after wave forces are determined by equation (63). Both ways are same as the force equation (63) of the body surface. Then, using Runge-Kutta-Nystrom 4th order method (see Appendix), body velocities and displacements are determined. Body displacements such as sway (horizontal), heave (vertical), and roll (rotational) motion will be used for updating body geometry and next time step calculation will be processed.

3.14. Indirect method

In linear theory, Haskind-Newmann relation can be utilized to calculate hydrodynamic force from the radiation problem results. Wu & Eatock Taylor (1996) introduced the same idea to calculate acceleration field. Kashiwagi (1998) called this method as a ‘new indirect method’ and used it in the 2D NWT. This method skips calculation of φ_4, the integral term in the equation (61). Instead, φ_4 can be obtained by using φ_i (i=1,2,3) term indirectly.

Green’s second identity was applied to φ_4 and φ_i (i=1,2,3)

$$\int_{\Omega}\left[\varphi_4\nabla^2\varphi_i-\varphi_i\nabla^2\varphi_4\right]d\Omega=\int_S\left[\varphi_4\frac{\partial\varphi_i}{\partial n}-\varphi_i\frac{\partial\varphi_4}{\partial n}\right]dS \tag{64}$$

Since $\nabla^2\varphi_i$ =0 and $\nabla^2\varphi_4$ =0, equation (64) is

$$\int_{S_B+S_F+S_A+S_R}\left[\varphi_4\frac{\partial\varphi_i}{\partial n}-\varphi_i\frac{\partial\varphi_4}{\partial n}\right]dl=0 \tag{65}$$

where, S_B, S_F, S_A, and S_R are body surface, free surface, input boundary, and rigid boundary respectively.

Equation (65) can be divided into each mode and the formulation is written as

$$\int_{S_B}\varphi_4\frac{\partial\varphi_i}{\partial n}dS=\int_{S_B}\varphi_i\frac{\partial\varphi_4}{\partial n}dS-\int_{S_F+S_A+S_R}\varphi_4\frac{\partial\varphi_i}{\partial n}dS+\int_{S_F+S_A+S_R}\varphi_i\frac{\partial\varphi_4}{\partial n}dS \tag{66}$$

From the equation (57)-(60)

$\frac{\partial\varphi_4}{\partial n}=q_B$ on the S_B

$\varphi_4=-gz-\frac{1}{2}\left|\nabla\phi\right|^2$ and φ_i (i=1,2,3)=0 on the S_F

$\frac{\partial\varphi_i}{\partial n}$=0 and $\frac{\partial\varphi_4}{\partial n}=\frac{\partial\phi_t}{\partial n}$ on the S_A

$\frac{\partial\varphi_i}{\partial n}$=0 and φ_i =0 on the S_R

Equation (66) can be written as

$$\int_{S_B}\varphi_4\frac{\partial\varphi_i}{\partial n}dS=\int_{S_B}\varphi_i q_B dS-\int_{S_F}\left(-gz-\frac{1}{2}\left|\nabla\phi\right|^2\right)\frac{\partial\varphi_i}{\partial n}dS+\int_{S_A}\varphi_i\frac{\partial\phi_t}{\partial n}dS \tag{67}$$

When we calculate body force by using equation (61), φ_4 integral term can be replaced by equation (67). Therefore, the computational time is reduced because φ_4 integral process can be omitted from boundary integral equation (55). In other words, on comparing to mode decomposition method, only 3 acceleration terms should be solved instead of 4 terms. When we use indirect method, however, body surface pressure can’t be obtained, because the time derivative of velocity potential (equation (56)) cannot be solved directly. This indirect method can solve body force only. The disadvantage of the indirect method is that the body pressure is not obtained.

Basically mode decomposition method and indirect method have the same mathematical formulation, except that φ_4 integral term can be replaced by other terms. In order to verify mode decomposition method used in this paper, comparison between both methods is carried out and shown in the figure 105.

3.15. Frozen coefficient method

When we use Runge-Kutta 4th order scheme as a time marching, this scheme requires 3 internal sub-step calculations for all boundary conditions such as free surface, floating body, and input boundaries. As a result of these internal step calculations, internal body displacements, i.e. body geometry information can be updated during internal step. For the complete Runge-Kutta 4th order scheme, the body geometry should be determined and new influence matrix should be calculated and inverted for every internal sub-step. So, the effort in calculation of Runge-Kutta 4th order scheme requires four times more computing power in order to accomplish one time step compared with other conventional scheme such as Adams-Bashford-Molton scheme or leap-frog method.

During the internal sub-step, the change of boundary shape is supposed to be small and the change of influence matrix is assumed to be small. From this assumption, we can skip update boundary shape and boundary conditions in the sub-step i.e. same influence matrix can be used within one time step. It is so called Frozen coefficient method. Using this scheme, calculation effort for one time step is much less because influence matrix can be inverted only once during internal sub time step. Frozen coefficient scheme can be a good substitution for reducing calculation time and can be valid for fixed body and prescribed body motion calculation.

However, for the freely floating body simulation, frozen coefficient scheme is not valid for some wave conditions especially in case of relatively large body displacement. Small difference of influence matrix affects wave force on the moving body slightly. So, the resulting body displacement cannot be determined correctly. As we mentioned earlier, for the floating body calculation, the equation of fluid particle and body motion equation should be solved simultaneously and the calculation has to be consistent for instantaneous time step. For instance, wave particle motion affects pressure on the body surface directly and resulting body force will make the body geometry, the body velocity, and the acceleration to change. Therefore, even if the difference in the body geometry is small, it will affect next time step input slightly and will result in a little different in the body motion. These phenomena and comparison of frozen coefficient and fully updated method will be shown in the Figure (79 to 81).

CHAPTER IV

NUMERICAL APPLICATIONS AND RESULTS

4.1. Wave generation and propagation

4.1.1. Nonlinear wave evolution (spatial variation) for intermediate depth

Waves generated by wave makers would undergo nonlinear interactions between each harmonics. In particular, the second-order free waves generated due to the mismatch between the particle velocity profile and actual wave maker motion propagate with different phase velocity as compared to the primary wave and thus cause some spatial variation in wave profile. Goda (1998) observed this phenomenon in a 2D physical wave tank and succeeded to reproduce/explain it using the third-order perturbation theory. He claimed that the interaction between the primary wave and the second-order free wave causes the spatial variation of the first- and third-harmonic components. The nonlinear spatial wave evolution investigated by Goda (1998) is reproduced in the present study using fully nonlinear NWT simulations.

Figure 2 shows the spatial variation of each harmonic amplitude when linear wave of period T=1.697s and height H=2.5cm is fed along the input boundary. Computational parameters from Figure 2 to Figure 5 are water depth=0.25m, wavelength=2.5m, free surface (computational domain)=9m, damping zone (artificial beach zone)=6m, delta x on the free surface=0.1m(first 3m) and 0.05m(rest 6m) and delta t is T/64. Figure 3 shows the same case when the piston type wave maker and moving boundary is used instead of feeding velocity profile at the fixed input boundary. The piston-wavemaker results show slightly more spatial variation than the feeding case.

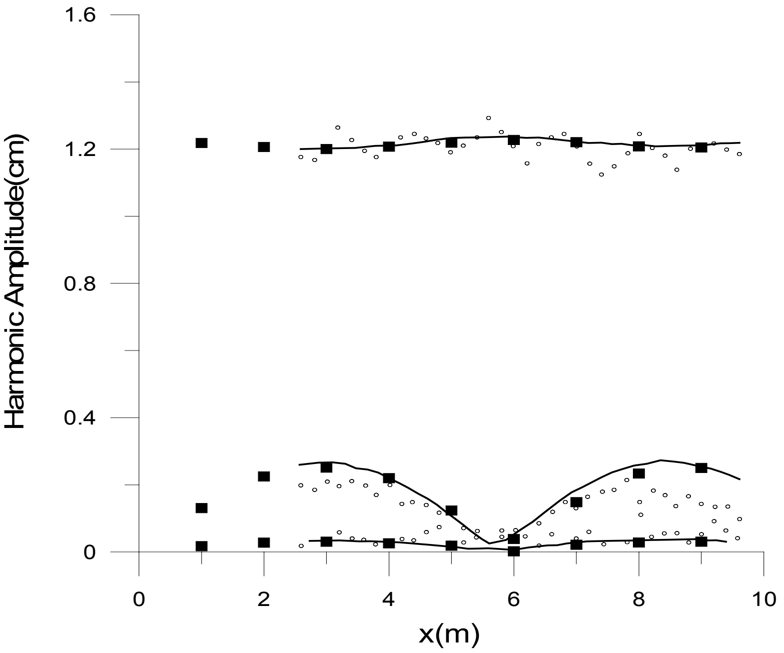

Figure 2. Comparison of spatial variation of fourier amplitudes with numerical results (rectangle), Goda's theoretical (solid line) and experiment (small circle). T=1.697s and height H=2.5cm, water depth=0.25m, wavelength=2.5m and dt=T/64.

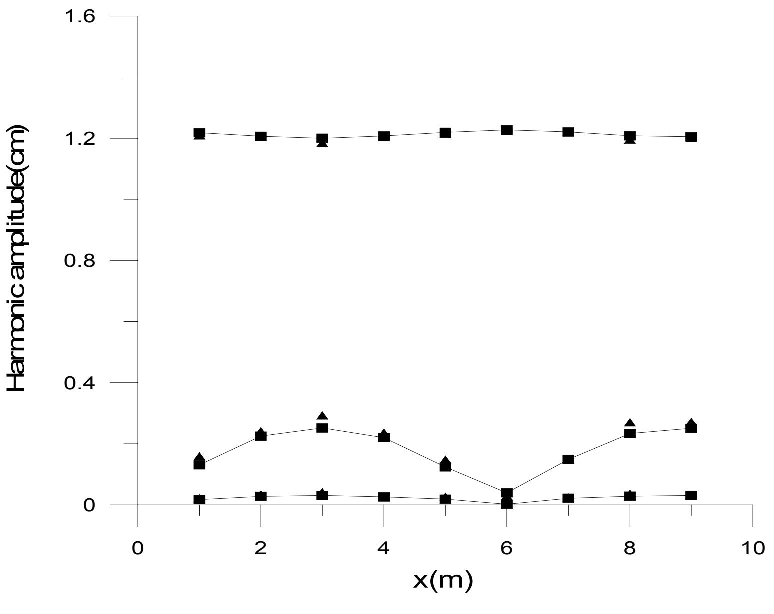

Figure 3. Comparison between feeding velocity profiles (rectangle) and piston type wave maker (triangle) (Same condition as Figure 2).

The difference between the smoothing and non-smoothing cases is shown in Figure 4. The maximum of 1st harmonic amplitude is located around 6m, where the minima of 2nd and 3rd harmonic amplitudes occur.

Figure 5 shows similar plots when wave heights are doubled (H=5.0cm). As wave height increases from 2.5cm to 5.0cm, the 2nd and 3rd harmonic amplitudes grow rapidly and the fluctuation of the 1st harmonic amplitude increases as well. For both wave heights, the present nonlinear NWT results are in good agreement with Goda's theoretical and experimental results. Figure 6 shows the change of wave profiles and corresponding heights at various locations and the appearance/deformation of secondary crest at the trough. The overall pattern is similar to that of experimental measurement by Goda (1998). The secondary crest appears behind the main crest, propagates with slower speed than the main crest, and is overtaken by the next crest as the wave propagates along the wave tank.

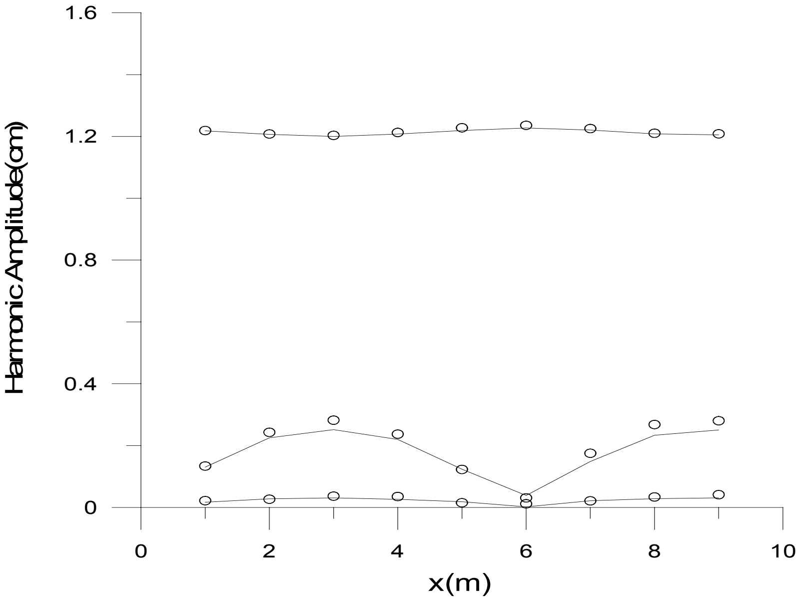

Figure 4. Comparison of spatial variation with smoothing (solid line) and without smoothing (white circle) (See Figure 2).

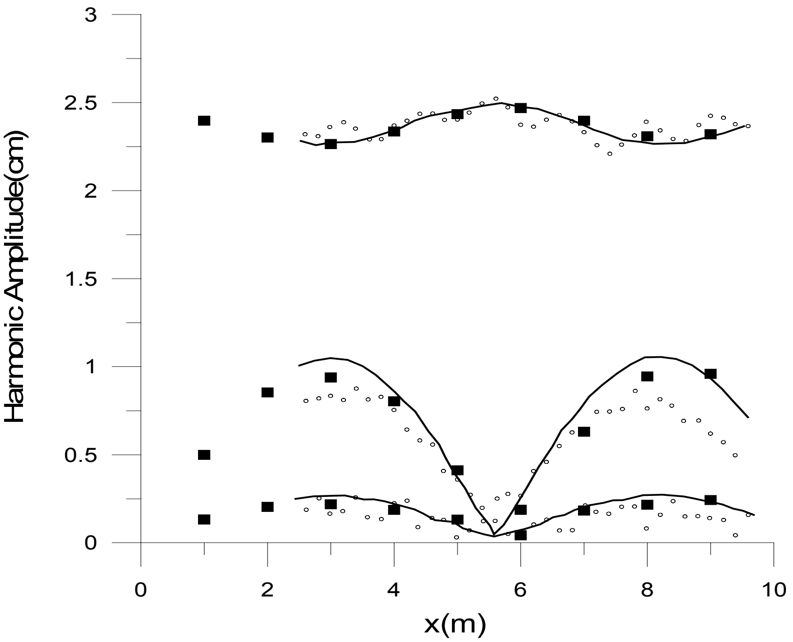

Figure 5. Case of H=5cm (See Figure 2).

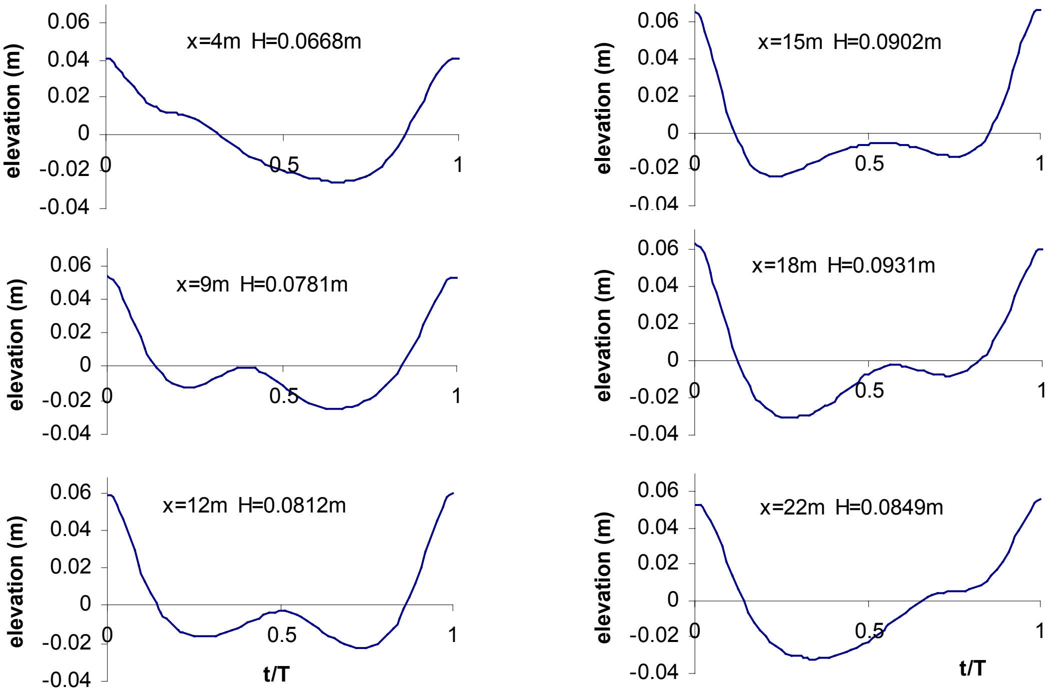

Figure 6. Examples of wave profiles with secondary crests at various locations (water depth=0.32m, T=3.07s, dt=T/64).

The spatial variation of wave profiles along the propagation distance is mainly caused by the generation of second-order free waves due to the mismatch of wave particle velocity profile and actual wave maker motions. If it is true, the phenomenon should disappear by matching the wave maker motion as close as possible to the actual velocity profile of the generated waves. To confirm this fact more clearly, the second-order Stokes wave velocity profile resembling the kinematics of the actual nonlinear wave is fed along the input boundary. The results for H=5cm are shown in Figure 7 and the spatial variation is greatly reduced as expected. Care needs to be taken in interpreting experimental/ simulation data when undesirable second-order free waves are present.

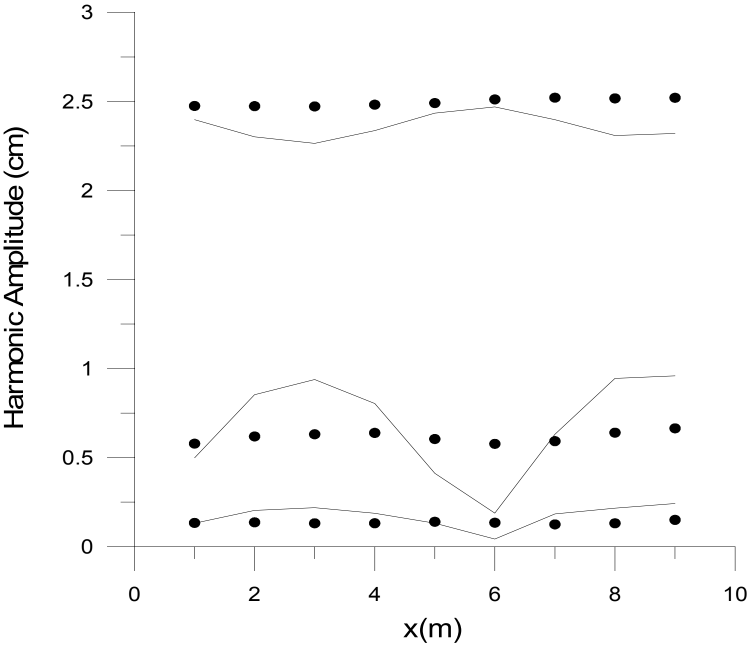

Figure 7. Comparison of spatial variation with linear wave input (solid line) and Stokes 2nd order wave input (black circle) (See Figure 2).

4.1.2. Water particle velocity

Using the fully nonlinear NWT, the wave kinematics of Figure 2 under wave crest are calculated and are presented and compared in Figure 8 with linear and second-order Stokes wave results. For the NWT computation, the 2nd-order Stokes waves are fed along the input boundary. The actual maximum horizontal velocity turned out to be greater than that of Stokes second-order waves. The difference is more pronounced above mean water level. Below mean water level, the maximum horizontal velocity (at crest) is greater than minimum value (at trough) and it causes some mean transport flow in the direction of wave propagation (Figure 8).

Finally, the wave kinematics of deepwater waves of H=9cm and T=0.887 are calculated using the fully nonlinear NWT and the results are compared in Figure 9 with linear theory. The experiment was conducted at Texas A&M University (Choi et al. 2001). It is seen that the NWT simulations agree more reasonably with the lab measurement than the linear theory. It is noticeable that the nonlinear NWT simulations produce small mean negative flow below mean water level (i.e. negative minimum value is larger than positive maximum value) and the phenomenon is also confirmed in the experiments.

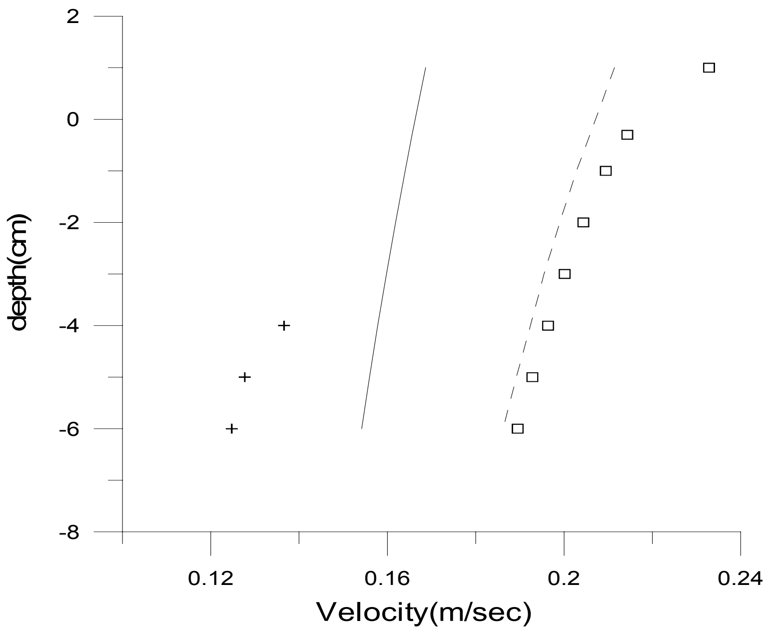

Figure 8. Comparison of crest (maximum) horizontal velocity (white rectangle), trough (minimum) horizontal velocity (cross) with Stokes 2nd order wave velocity (dashed line) and linear wave velocity (solid line).

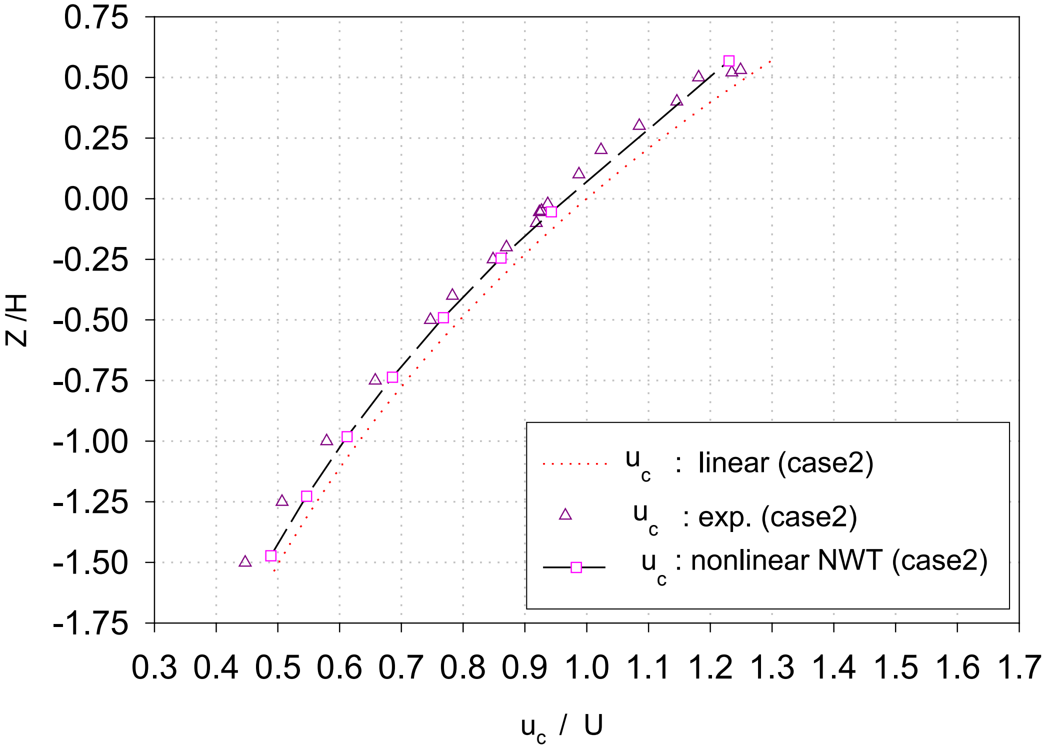

Figure 9. Comparison with wave crest horizontal velocities (U is measured at z=0).

4.1.3. Summary

Both wave profiles and wave kinematics of highly nonlinear waves are calculated using the present, fully nonlinear NWT. It is confirmed that the spatial variation of intermediate-depth waves along the direction of wave propagation is caused by the unintended generation of second-order free waves, which was originally investigated both experimentally and theoretically (3^{rd} order perturbation theory) by Goda. The various phenomena observed by Goda are clearly reproduced by the present NWT. His explanation of pertinent physics is also demonstrated by comparing the simulation results for different wave maker motions. The wave kinematics of nonlinear NWT simulations are compared with the linear, Stokes second-order theory and experimental values. It is shown that the wave kinematics above mean water level can be significantly different from the perturbation-based prediction. It is also found that small mean positive or negative flows can be generated below mean water level depending on the water depth and wave condition. Chapter 4.1 was quoted from Koo & Kim (WAVES 2001, page 1096-1101).

4.2. Fully submerged single and dual cylinders

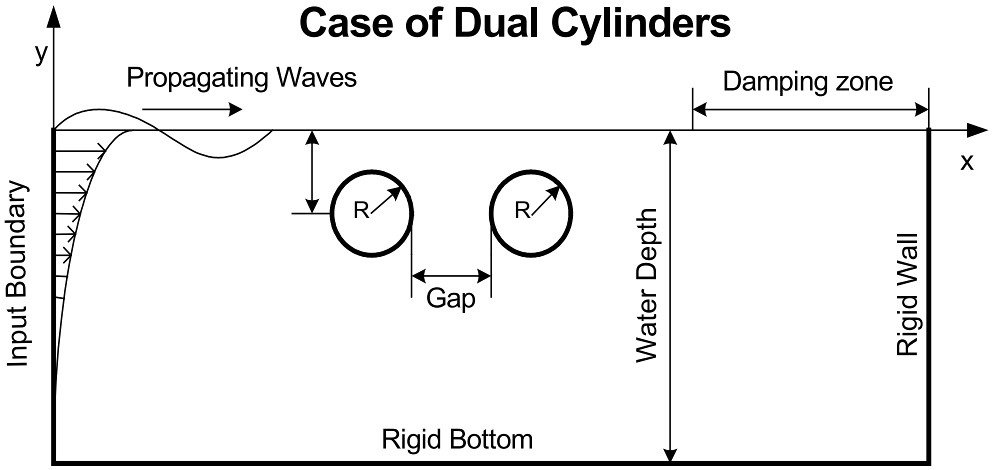

Figure 10. Sketch of Numerical Wave Tank for fully submerged dual cylinders

The developed potential-flow-based NWT is used to calculate the nonlinear wave forces on a fixed submerged circular cylinder. The simulated results are compared up to third order with the 2nd-order theory of Ogilvie (1963), experimental results of Chaplin (1984), and high-order spectral method of Liu et. al. (1992). After this verification, the interaction of submerged dual circular cylinders with fully nonlinear waves is investigated for various gaps and incident wave conditions. In addition, the finite difference method was used to obtain ϕ_t (equation 37) and the node velocity for wave force calculation (equation 39) was set to zero because the submerged cylinders are stationary. Also, body boundary is no-flux condition same as the rigid boundary. Figure 10 shows the sketch of NWT for fully submerged dual cylinders.

4.2.1. A fixed fully submerged cylinder

Fourier analysis was applied to the portion of the steady-state wave-force time series for obtaining respective harmonic components. The mean, 1st, 2nd, and 3rd harmonic wave forces were compared with other theoretical (Ogilvie, 1963), numerical (Liu et. al., 1992), and experimental (Chaplin, 1984) results. Figure 11 shows that the calculated mean vertical forces are in good agreement with both theoretical and experimental results for different KC numbers. It appears that the mean vertical force is linearly proportional to the

KC number with Log scale. The mean horizontal forces (Figure 12) are of smaller magnitude as compared to the mean vertical forces. It is actually zero in the context of second-order wave-body interaction theory. The mean horizontal force is small and negative at KC=0.5, but becomes positive for higher KC (=0.75). Longuett-Higgins attributed the possible mean negative horizontal force on a submerged cylinder to wave breaking. However, the present simulation (also Liu & Yue, 1992) shows that the negative mean force may occur without breaking.

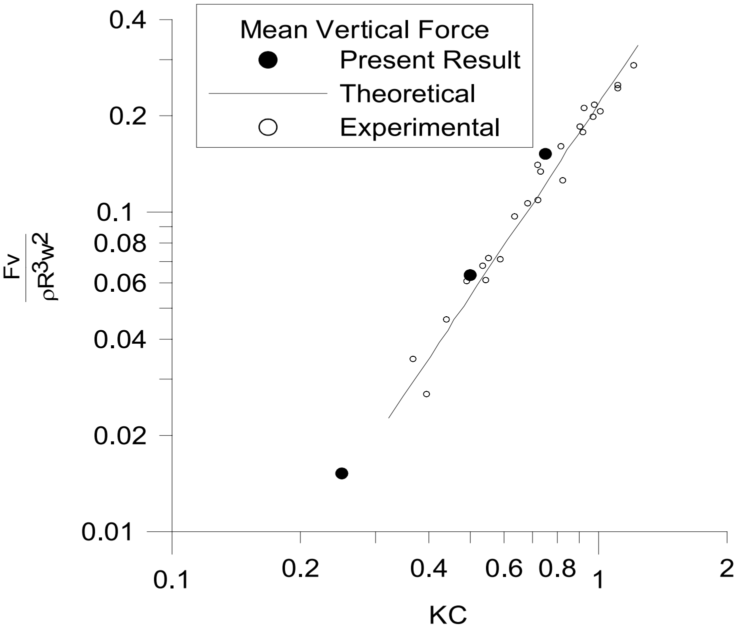

Figure 11. Mean vertical forces against KC values with log scale. Forces are normalized by $\rho\omega^2 R^3$ (water depth=0.85m, diameter(R)=0.102m, center of cylinder=(2m, -R), w=2*pi, dt=T/64).

The 1^{st} harmonic horizontal and vertical forces are shown in Figure 13. They agree well with another potential-based nonlinear calculation by high-order spectral method. However, there exists a big difference between the potential-flow-based nonlinear simulations and Chaplin's experimental results, especially for larger KC values. The discrepancy is mainly due to the viscous effects i.e. the presence of clockwise circulation around the body (Chaplin, 1984). To verify Chaplin's observation, another independently developed viscous-flow-based NWT (Tavassoli and Kim, 2001) was run for the same case. The viscous NWT results actually show the same trend (decrease of 1st harmonic force with KC number) as observed in Chaplin's experiment.

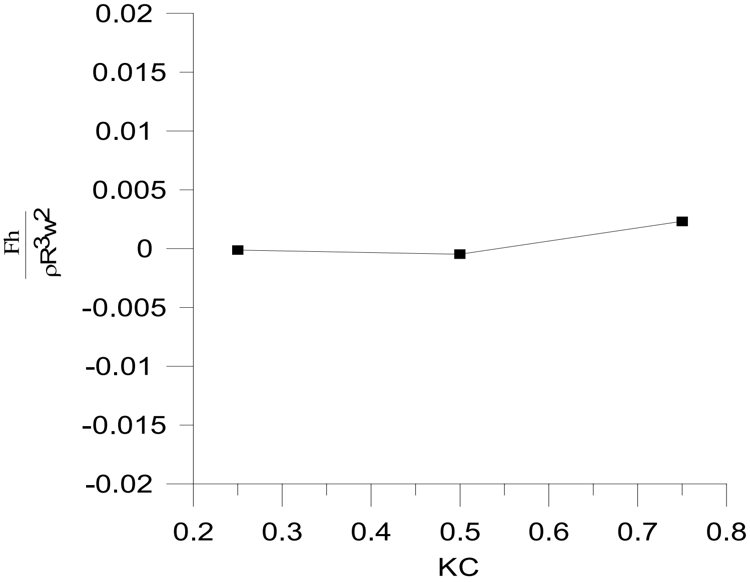

Figure 12. Mean horizontal force (See Figure 11).

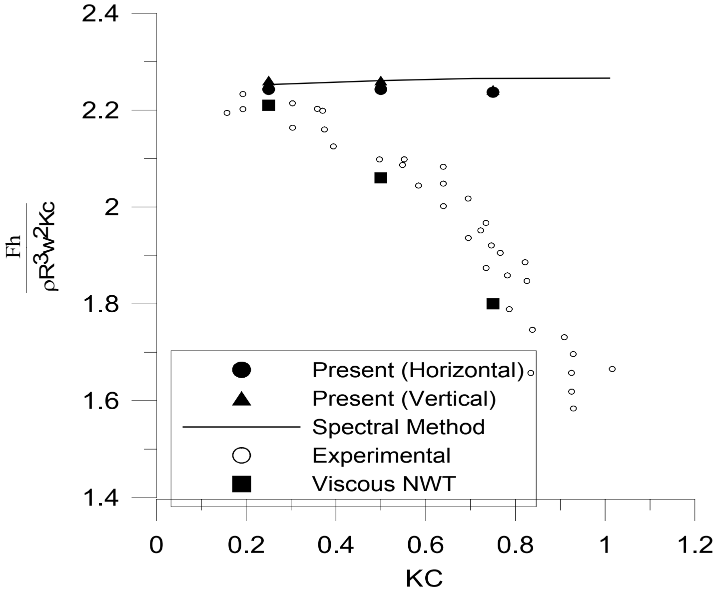

Figure 13. 1st harmonic forces normalized by $\rho\omega^2 R^3 KC$ (See Figure 11).

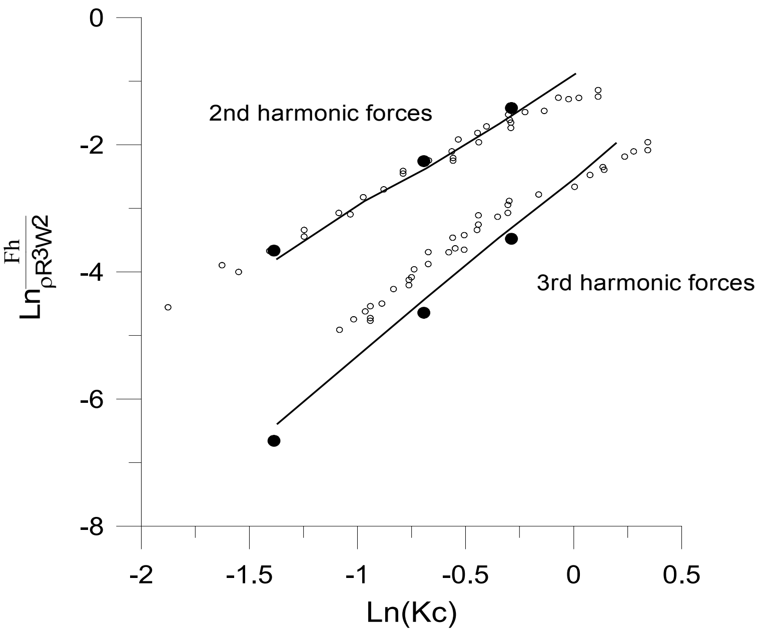

Figure 14. 2nd and 3rd harmonic forces with log scale. Present (2nd & 3rd horizontal-black circle), high order spectral method (2nd & 3rd=solid line), and experiment (small white rectangle) (See Figure 11).

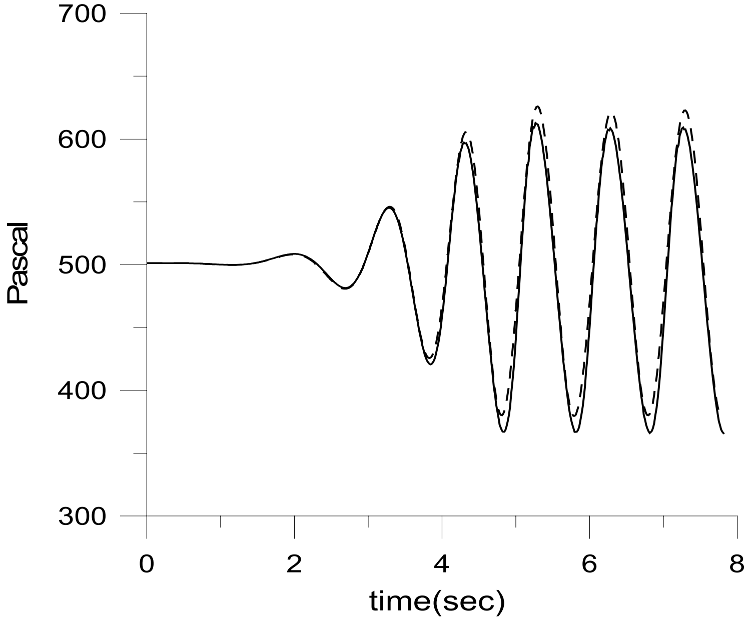

Figure 15. Time series of pressure on the top of the cylinder in case of KC=0.5. Linear (solid line) and nonlinear (dotted line) (See Figure 11).

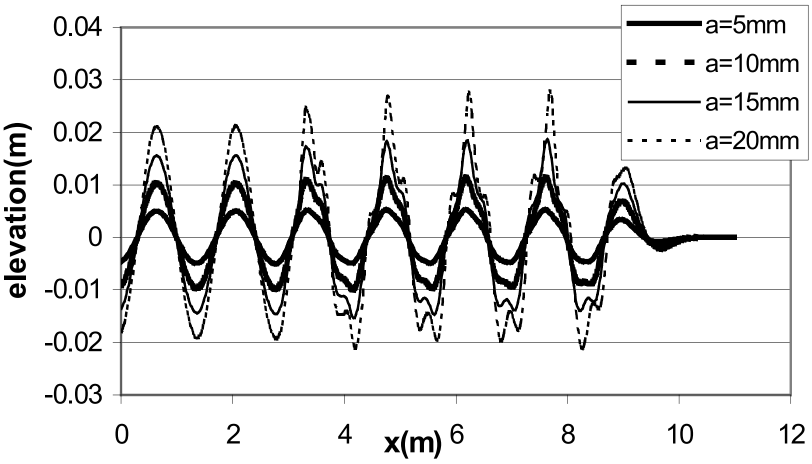

Figure 16. Snapshot of wave elevation for submerged cylinder center located at (3m, -0.2m) (depth=0.85m, w=2pi*1.05, dt=T/64 and cylinder diameter=0.2m).

Figure 14 shows the comparisons of 2nd and 3rd harmonic horizontal and vertical forces among present NWT simulation, high-order spectral method, and Chaplin's experimental results. All the results are in good agreement with one another, which means that viscous effects are not important in the case of force components higher than second order. Figure 15 shows the time series of pressure on the top of the cylinder. The signal has higher crest and shallower trough when compared with the linear pressure.

Figure 16 shows the snapshots of free-surface elevation for various input wave amplitudes over the full range of the NWT. First of all, we can clearly see the effectiveness of the current artificial wave damper regardless of incident wave heights. When input wave amplitude is small, the distortion of the original profile behind the submerged cylinder is small. However, the distortion mainly characterized by higher and narrower crest, becomes more and more pronounced as incident wave amplitude increases. When incident wave amplitude a=2cm (H/L=0.028), the non-linearity profile and distortion are very noticeable behind the submerged cylinder. This can be attributed to the spontaneous generation of higher-harmonic wave components when waves pass over the cylinder. In this case, the energy conservation is checked in all cases. When a significant profile distortion occurs as a=2cm case, the mean drift force cannot be accurately obtained from far-field formulas.

4.2.2. Fully submerged dual cylinder

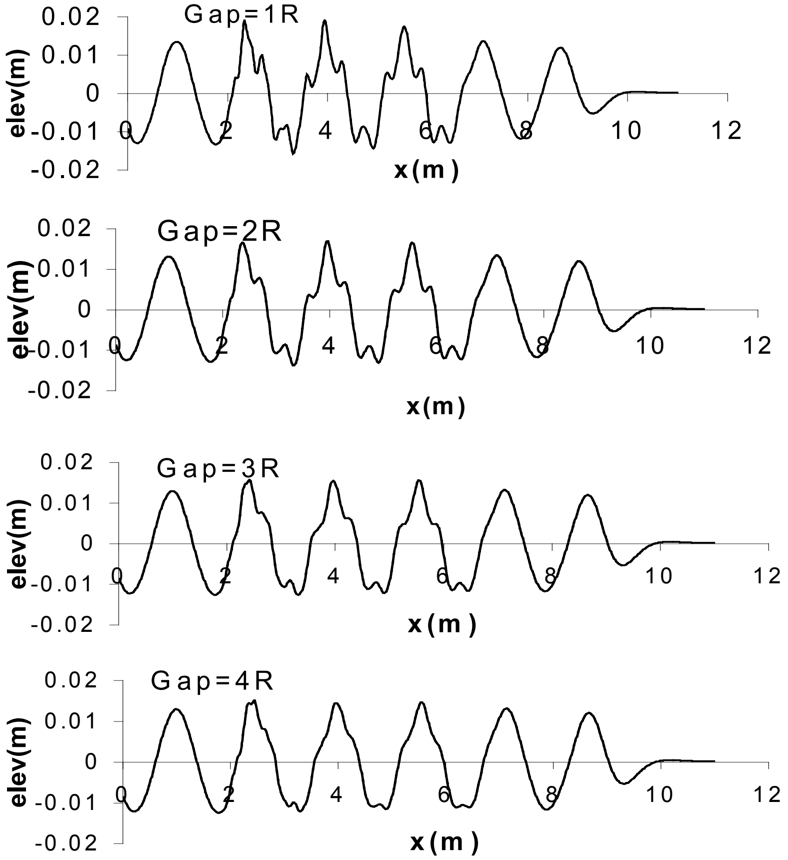

Figure 17. Snapshots of wave elevation for dual submerged cylinders with various gap (Incident amplitude (A)=0.01225m, KC=0.5, T=1sec, dt=T/64, cylinder radius (R)=0.051m, center of 1st cylinder=(2m, -2R), water depth=0.85m).

From now on, we consider nonlinear wave interactions with dual submerged cylinders using the same NWT. It is of great interest to know the variation in nonlinear wave forces on two submerged cylinders against different gap distances. First in Figure 17, the snapshots of wave profiles along the entire range of the NWT are plotted for various gap distances. It is observed that the distortion is the greatest when the gap is smallest. When incident waves propagate over the front cylinder, the noticeable shape deformation occurs. The nonlinear distorted waves then propagate toward the rear cylinder like highly nonlinear incident waves. This is the major reason why higher-harmonic force components are greatly amplified on the rear cylinder. All the results from now on are for KC=0.5

Figure 18 shows the mean horizontal forces on both cylinders against various gaps. Compared to the single-cylinder case, the magnitudes are greatly amplified as a result of interaction particularly when the gap is small. The front cylinder has a positive mean horizontal force, while the rear cylinder has negative value. This means that the two cylinders tend to drift in the opposite direction to reduce the gap. This phenomenon is more pronounced for smaller gaps. This result may have important applications when two submarines navigate side by side close to the free surface in beam waves. It is expected that the intensity of interaction decreases as the gap increases. Eventually, the front-cylinder results should converge to the single-cylinder results when the gap is very large.

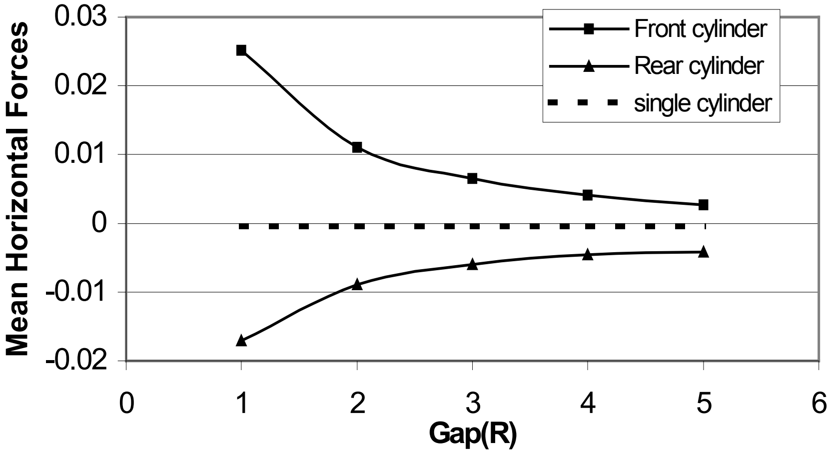

Figure 18. Mean horizontal forces for dual fixed submerged cylinder. Mean forces are normalized by $\rho\omega^2R^3$ (See Figure 17).

Figure 19 shows the variation of mean vertical forces on both cylinders against various gaps. When the gap is equal to the radius, the mean vertical forces on both cylinders are increased by about 40% compared to the single-cylinder case.

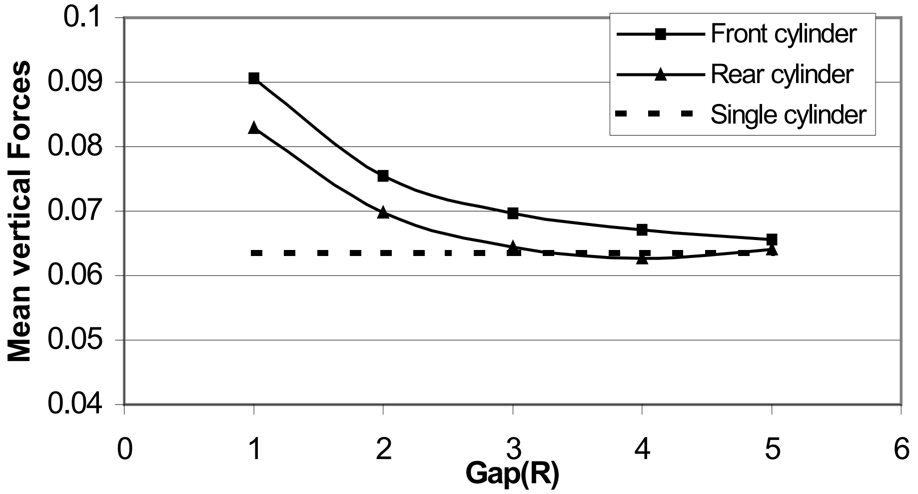

Figure 19. Mean vertical forces (See Figure 17 & Figure 18).

Figure 20 and Figure 21 present 1st-order horizontal and vertical forces on both cylinders against various gaps. The wave-frequency horizontal force on the front cylinder becomes larger and larger as gap decreases, while the opposite trend holds true for the rear cylinder. This observation can be interpreted as a kind of shielding effect. However, we cannot see the same shielding effect for the wave-frequency vertical forces. Interestingly, the shielding effect does not appear in the higher-harmonic force components. The increase of wave-frequency vertical force can be as large as 25% when the gap is the smallest (=radius).

Figure 22 through Figure 25 show very interesting results. The 2nd and 3rd-order horizontal and vertical forces are greatly amplified especially on the rear cylinder compared to the single-cylinder case. Larger amplification at the rear cylinder is due to the distortion of the incident waves by the front cylinder. This trend is more pronounced when gap is small, as was also illustrated in Figure 17.

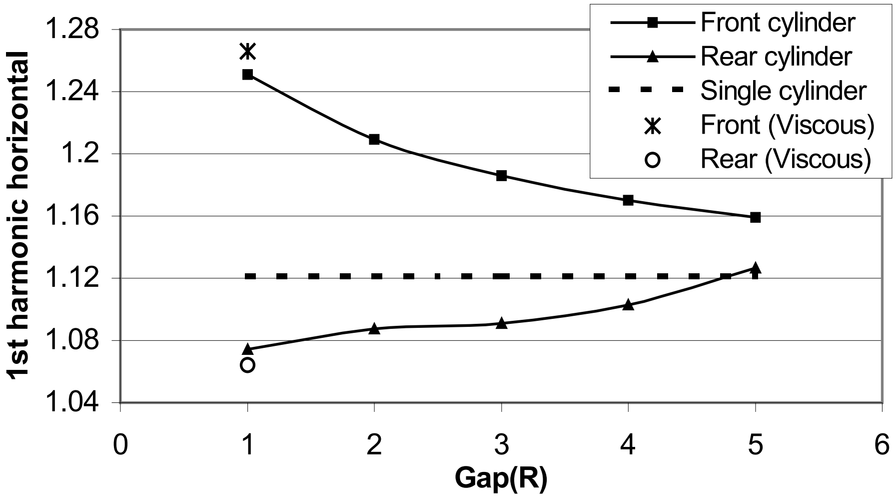

Figure 20. 1st order horizontal forces normalized by $\rho\omega^2R^3$. Viscous NWT results are included (See Figure 17).

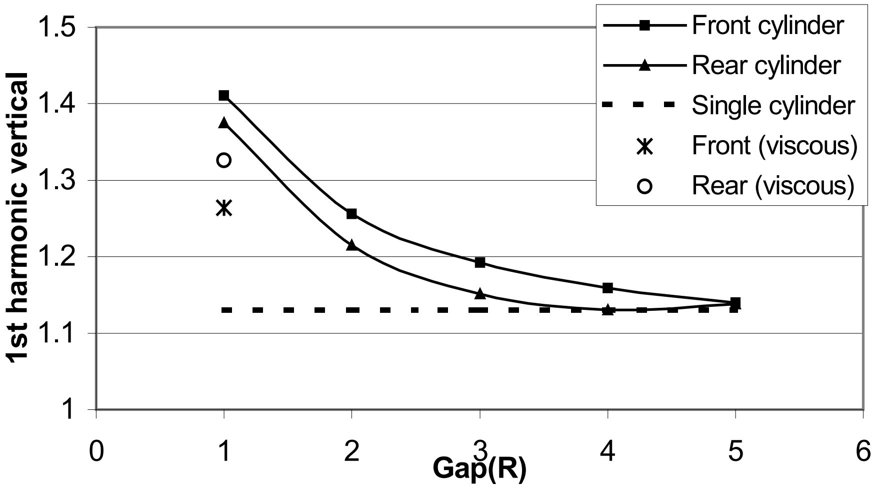

Figure 21. 1st order vertical forces normalized by $\rho\omega^2R^3$ (See Figure 17).

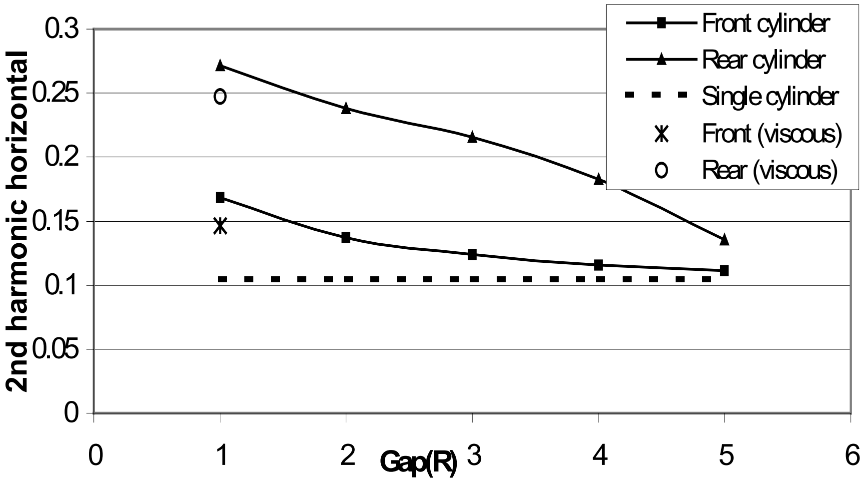

Figure 22. 2nd order horizontal forces normalized by $\rho\omega^2 R^3$ (See Figure 17).

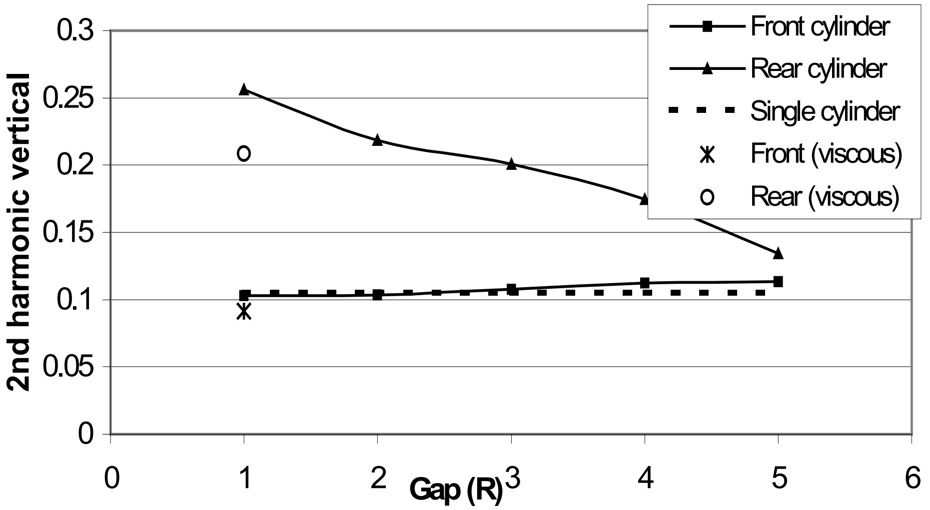

Figure 23. 2nd order vertical forces normalized by $\rho\omega^2 R^3$ (See Figure 17).

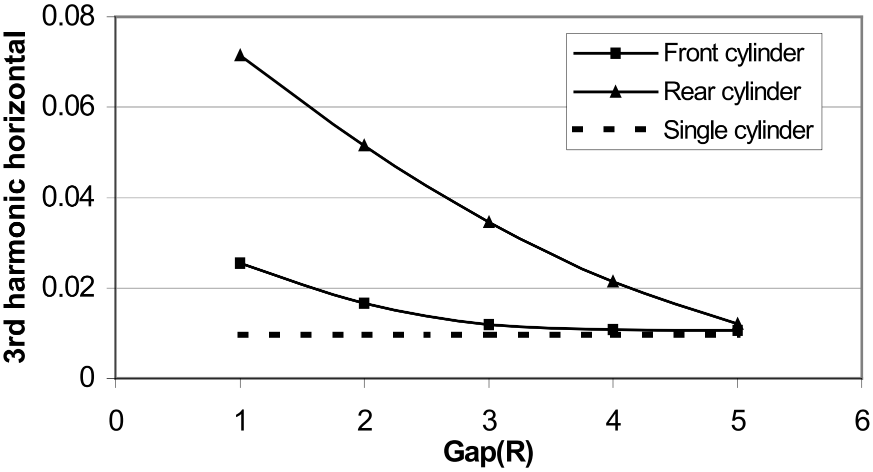

Figure 24. 3rd order horizontal forces normalized by $\rho\omega^2R^3$ (See Figure 17).

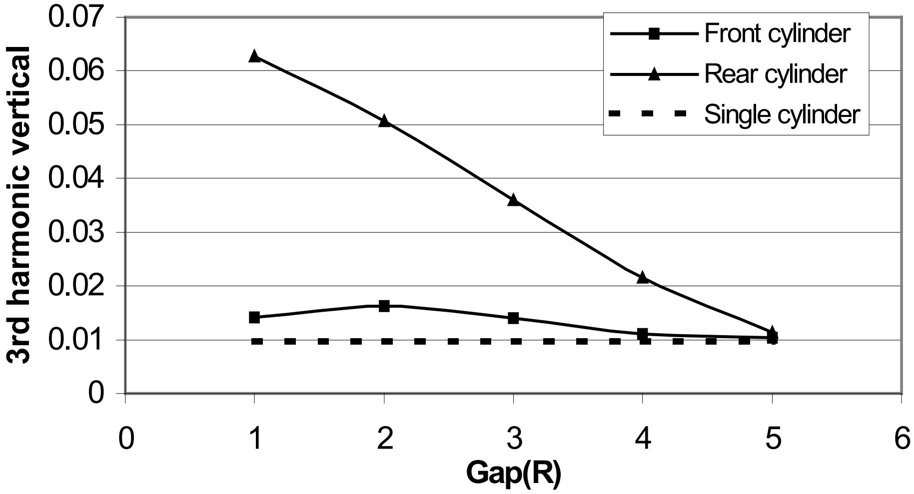

Figure 25. 3rd order vertical forces normalized by $\rho\omega^2R^3$ (See Figure 17).

For example, when gap equals the radius, the 2nd-order horizontal and vertical forces on the rear cylinder are about 60 % and 150 % greater than those on the front cylinder (170% and 150% greater than those of single cylinder). The amplification of 3rd-order forces is even greater so that their magnitudes for the smallest gap are 6-7 times greater than those of single cylinder. When waves propagate over the front cylinder, they start to deform, and the deformation is more intensified above the rear submerged cylinder.

That is why the higher-order force components on the rear body are much greater than those of front body.

So far, we have investigated the interactions of dual submerged cylinders with fully nonlinear waves based on the potential-based NWT. In the single cylinder case, there existed big discrepancy between potential and viscous NWTs only in the 1st harmonic components particularly when the KC number is large. Otherwise, the potential theory gave reasonable results for all the components.

We expect the same kind of KC-number dependency in the case of dual cylinders. In other words, as KC number increases, we expect larger discrepancy between potential theory and viscous-flow simulation. In case of KC=0.5 and gap=radius, we also plotted the results obtained from viscous NWT. The general trend of the amplification of 1st and 2nd-order forces due to interactions by the dual cylinders is similar to that of potential-flow computation.

4.2.3. Summary

Wave deformation and force time series due to fully submerged single cylinder were obtained using the developed NWT. The mean and a series of higher harmonics are then calculated from the time series. The computed mean, 1st-, 2nd-, and 3rd-order force components for a submerged cylinder compare well with those of Chaplin's experiment and Liu & Yue's high-order spectral method. The noticeable discrepancy on the 1st-order wave forces for higher KC numbers is due to the viscous effect (clockwise circulation around the body), as speculated by Chaplin, and was also confirmed by an independently developed viscous-flow-based NWT.

The developed fully nonlinear NWT is next applied to solve wave diffraction by fixed dual submerged cylinders for various gaps. It is clearly seen that the interaction effects become of critical importance when the gap is small, and their magnitudes can be greatly amplified. This trend is more pronounced for the higher harmonic forces on the rear cylinder. When the gap is large, the case of dual-cylinder tends to converge to the single-cylinder case. The directions of the horizontal mean forces on the dual cylinders are opposite to each other, and their magnitudes are appreciably increased as gap decreases. The phenomenon of opposite direction of horizontal mean forces can be applied for real situation such as two submarines near the free surface. These submarines may be dangerous when they operate near the free surface with beam sea conditions.

As for the 2nd and 3rd-order forces, the rear cylinder generally has much bigger horizontal and vertical forces than the front cylinder due to the noticeable free-surface deformation caused by the front one. The trend of the amplification of forces on dual submerged cylinders predicted by the present potential-NWT is qualitatively similar to that of the viscous-NWT results when KC=0.5. Most of the contents in Chapter 4.2 were quoted from Koo & Kim (ISOPE 2003).

4.3. Surface piercing fixed structures

4.3.1. Single barge

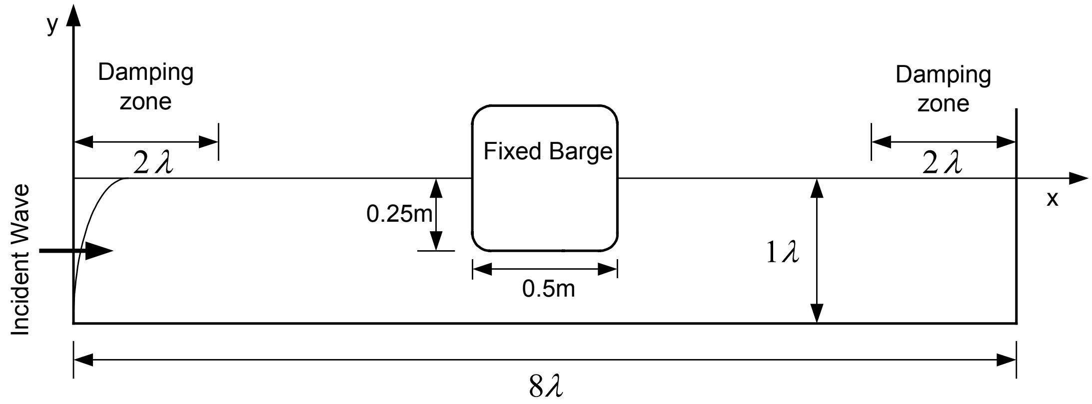

Figure 26. Sketch of surface piercing single barge simulation. Radius of barge round corner=0.064m, B(width)=0.5m, d(draft)=0.25m.

The developed fully nonlinear NWT is utilized to calculate mean drift force and a series of 3-mode wave loads such as sway, heave and roll on a fixed surface piercing barge-type structure. The calculated wave loads on the body are compared with experimental results of Nojiri & Murayama (1975), analytical solution of Maruo (1960), and other numerical results of Tanizawa and Minami (1998). Two different incident wave height results are also compared. Finally, a series of force components is obtained by using time series of force and is compared against incident wave frequencies. Figure 26 shows the sketch of surface piercing single barge simulation and Table 1 indicates all input wave properties.

To calculate wave loads on a fixed surface piercing body, the time derivative of velocity potential should be obtained precisely. The surface piercing body has intersections of body and free surface. These intersections are fluctuating during the time simulation and the body-surface nodes are moving with surface elevation. In the present case, an acceleration potential method was used because this method is useful to overcome the complexity of body-node fluctuation due to the incident waves. It is not easy to evaluate node velocity when we use finite difference method for ϕ_t. However, the acceleration potential method can avoid this problem. ϕ_t can be obtained directly by solving the boundary integral equation for ϕ_t at each time step.

From Figure 27, the calculated drift forces are compared with experimental, analytical, and other numerical results for various incident wave frequencies. Present results are in good agreement with experimental results except some local deviation on high frequency region. This local deviation may be due to the input wave steepness. Input wave steepness is higher as wave frequency increases with constant wave height (H=7cm).

Figure 28 shows the comparison of 1st order horizontal (sway) forces on a fixed barge. The horizontal forces of present study agree well with other results. Figure 29 and Figure 30 show the comparison of heave force and roll moment. All the results from the developed NWT agree well with experimental and other nonlinear results. From this point, we can confirm the numerical results for surface piercing body.

Table 1. Incident wave input with 1 wavelength water depth

ξ (xsi)	**λ (m)**	**Wave Steepness**		$\xi = \frac{\omega^2}{g}\frac{B}{2}$
		H=1cm	H=7cm	
0.25	6.2831	1/628	1/90	
0.40	3.9269	1/393	1/56	
0.60	2.6179	1/262	1/37	1/87(3cm), /52(5cm)
0.65	2.4166	1/242	1/35	
0.75	2.0944	1/209	1/30	
0.82	1.9156	1/192	1/27	
1.00	1.5707	1/157	1/22	
1.25	1.2566	1/126	1/18	
1.50	1.0472	1/105	1/15	

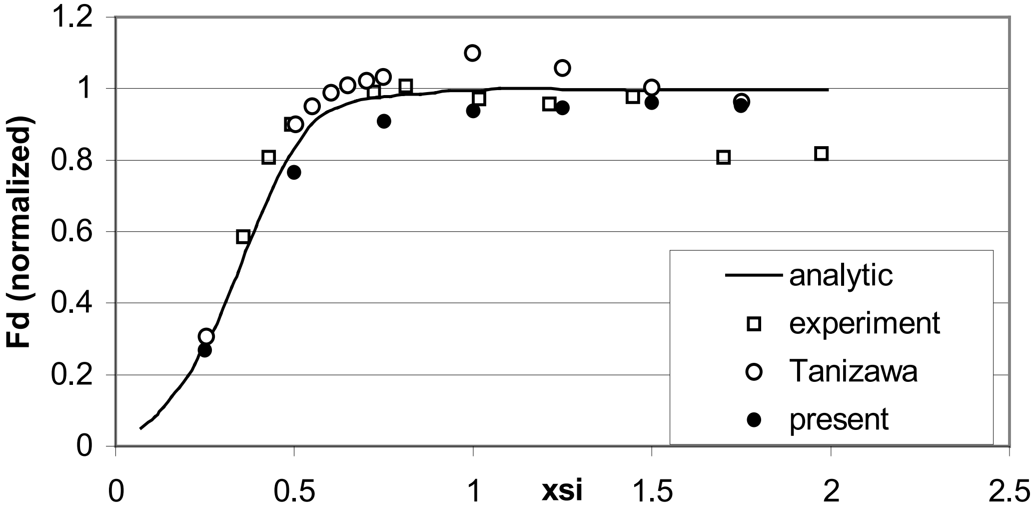

Figure 27. Comparison of drift force of a fixed surface piercing barge against various wavelength with Incident wave height, H=0.07. Fd is normalized by $0.5\rho g L(\frac{H}{2})^2$**, where L=1 (for 2D).**

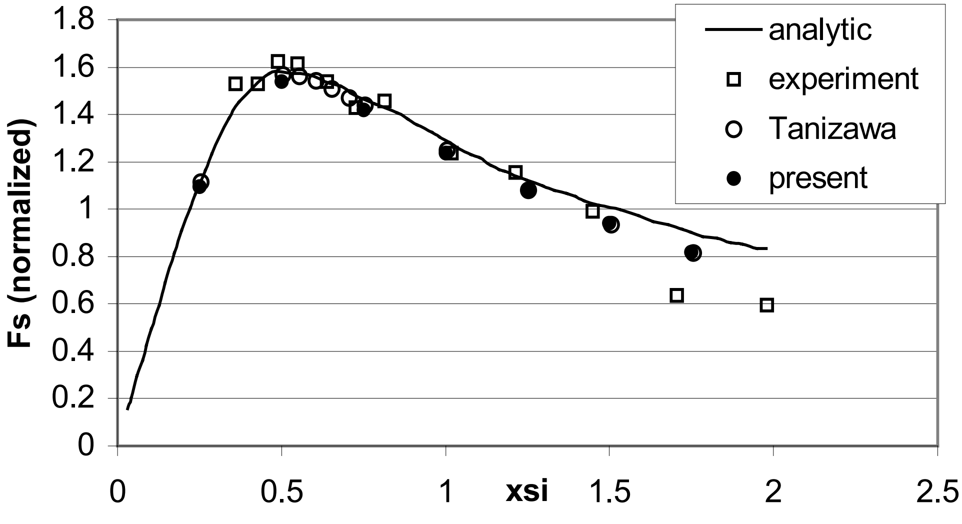

Figure 28. Comparison of sway force normalized by $\rho g L d(\frac{H}{2})$**, (See Figure 27).**

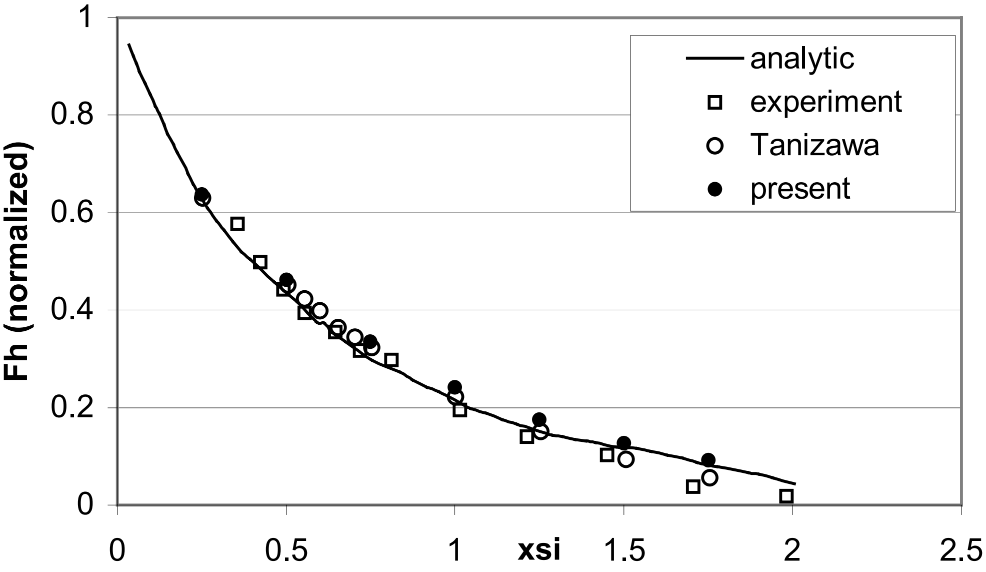

Figure 29. Comparison of heave force normalized by $\rho gLB(\frac{H}{2})$ **(See Figure 27).**

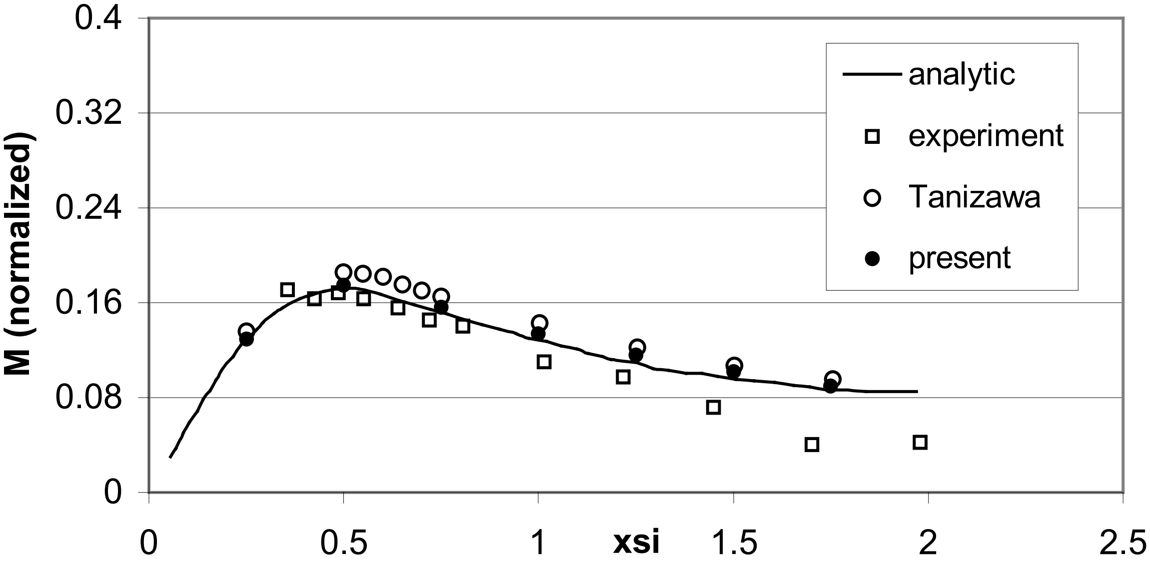

Figure 30. Comparison of roll moment normalized by $\rho gLBd(\frac{H}{2})$**. (See Figure 27).**

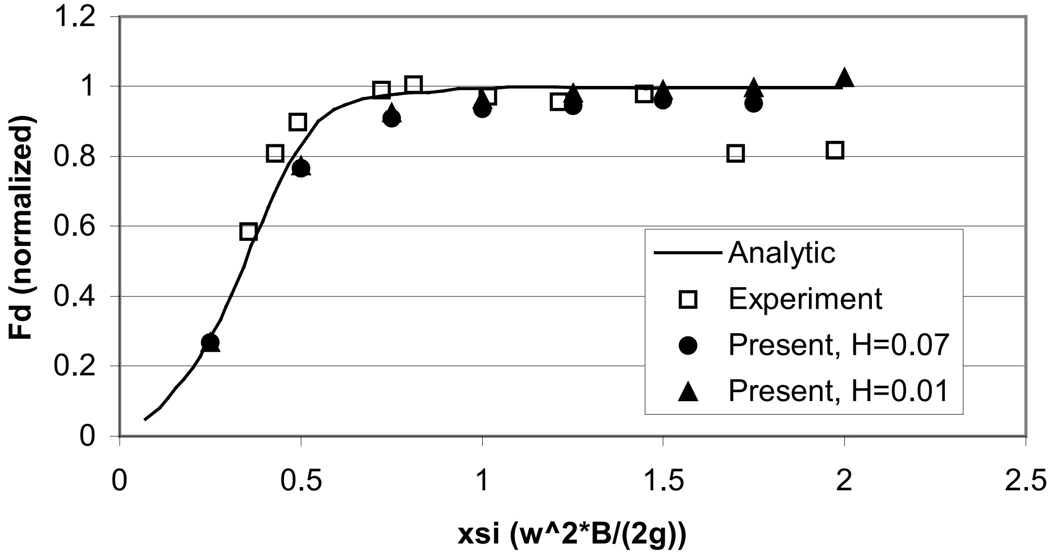

Figure 31. Comparison of drift force for various input heights (See Figure 27).

In the Figure 31, two different incident wave height results are compared with experimental and 2nd order analytic solution. When the incident wave height is 1cm, the calculated drift force is closer to the analytic solution on higher wave frequencies. In the low frequency region, both results (1cm, and 7cm cases) are very close to each other. This phenomenon is more clearly shown to the Figure 32. As the incident wave frequency increases, the difference of the normalized horizontal (sway) forces is larger. This means that wave steepness is very important for fully nonlinear simulation because nonlinearity becomes pronounced as wave steepness increases. Comparison of heave force and roll moment with different incident wave input is shown in the Figure 33 and Figure 34. These results agree well with experimental results.

Figure 35 shows sway force components obtained by time series of the body forces against various wave frequencies. Maximum value of 1st order force is observed at xsi=0.5 (L=3.14m) and the 2nd, 3rd order components have minimum values at the xsi=0.75 (L=2.09m). After that frequency, these high components increase gradually.

For the comparison of vertical force components shown in Figure 36, 2nd order force becomes dominant as frequency increases especially higher than xsi=1.25 (L=1.25m). From this frequency, the magnitude of 2nd order force is even greater than 1st harmonic force. When the incident wave frequency increases with constant wave height, i.e. wave steepness becomes higher, the effect of 1st harmonic horizontal and vertical forces decreases and that of higher harmonic force is pronounced. In particular, 2nd order vertical force for a fixed barge-type structure is greater than 1st order force. It means that the behavior of incoming waves becomes nonlinear as the wave steepness increases making the wave-body interactions dominant. Roll moment components are shown in Figure 37. Interestingly, 2nd and 3rd order components does not increase as wave steepness increases.

In summary, 1st hamonic force would decrease as wave frequency increases. The 2nd order horizontal and vertical forces increase especially in vertical direction as wave steepness increases, while rotational component does not change a lot.

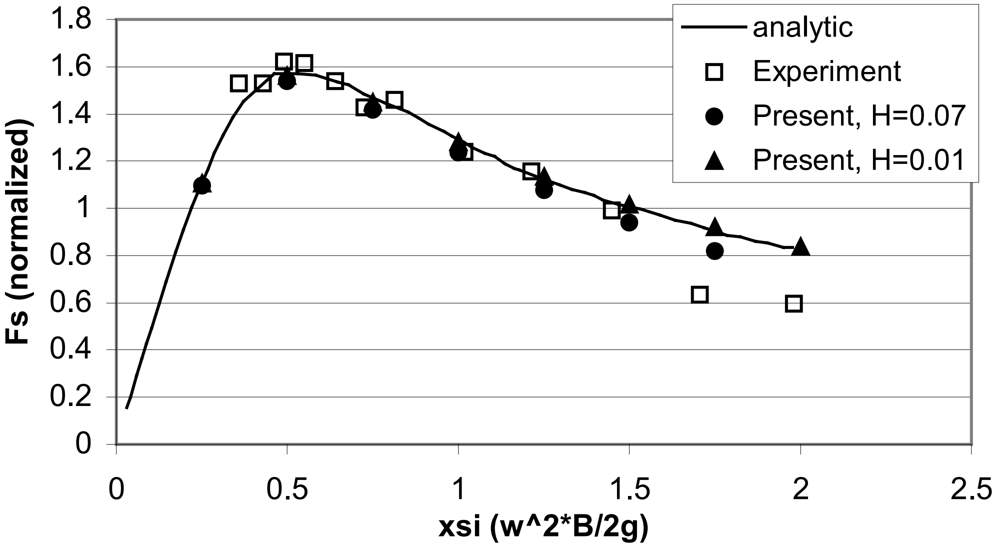

Figure 32. Comparison of sway force for various input heights (See Figure 28).

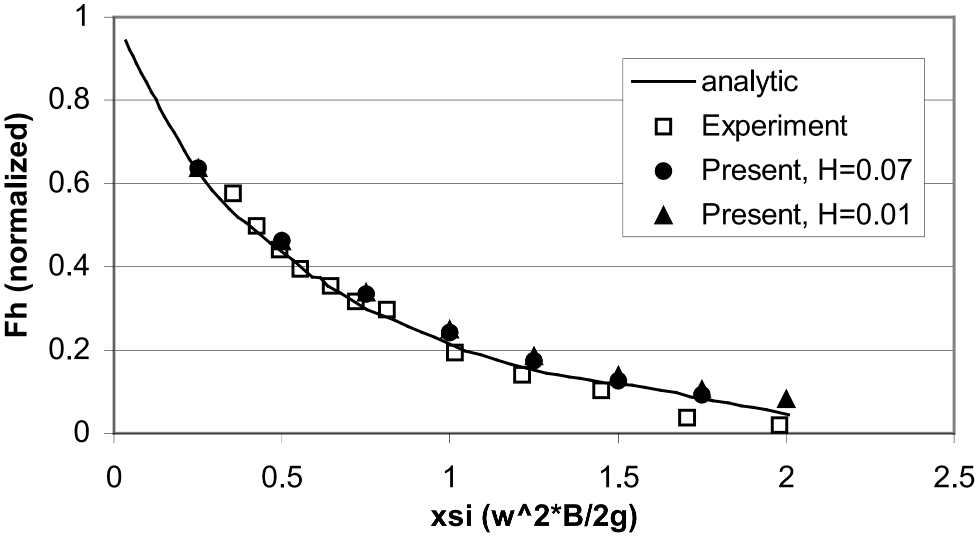

Figure 33. Comparison of heave force for various input heights (See Figure 29).

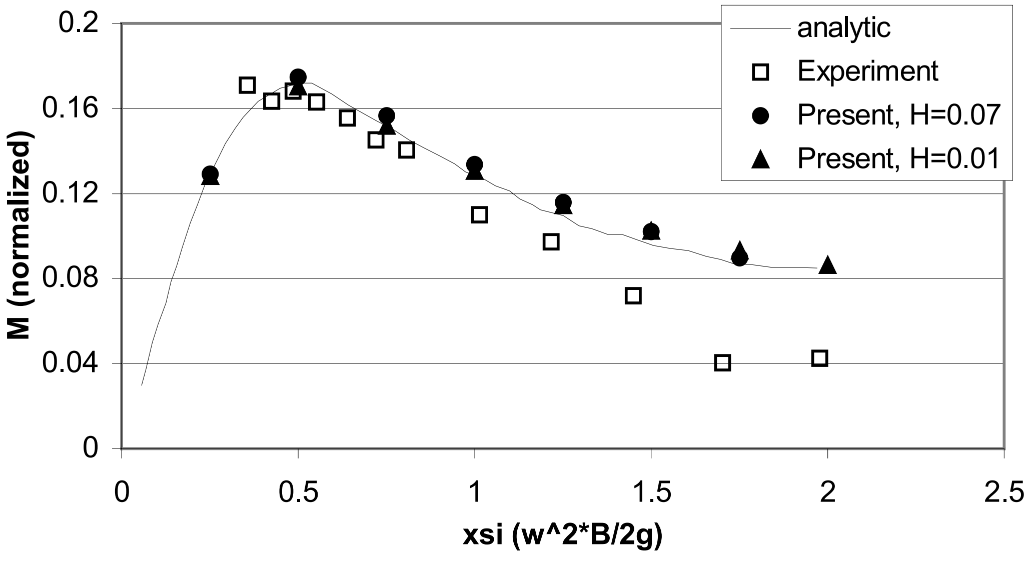

Figure 34. Comparison of roll moment for various input heights (See Figure 30).

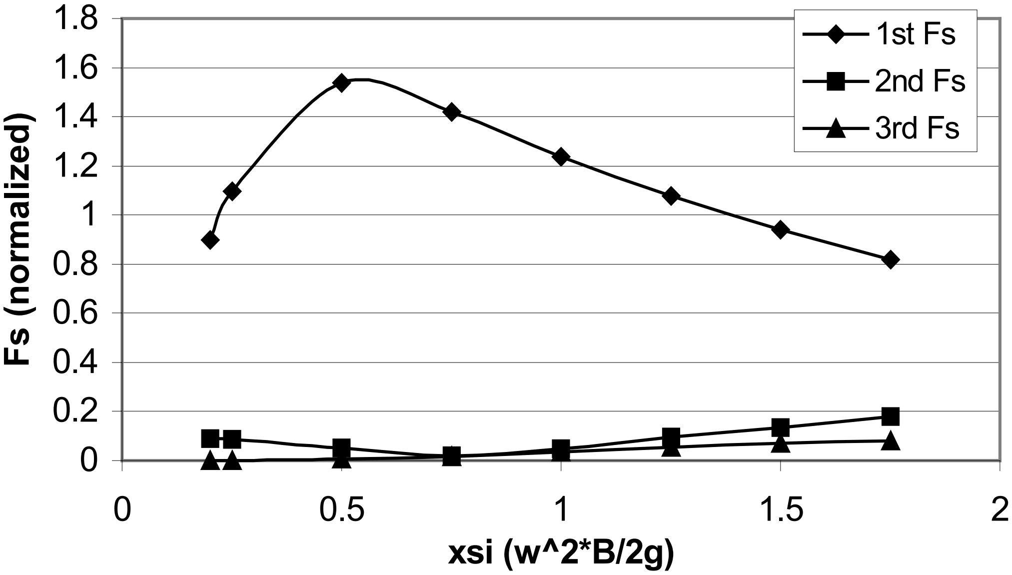

Figure 35. Comparison of sway force components with H=0.07 (See Figure 28).

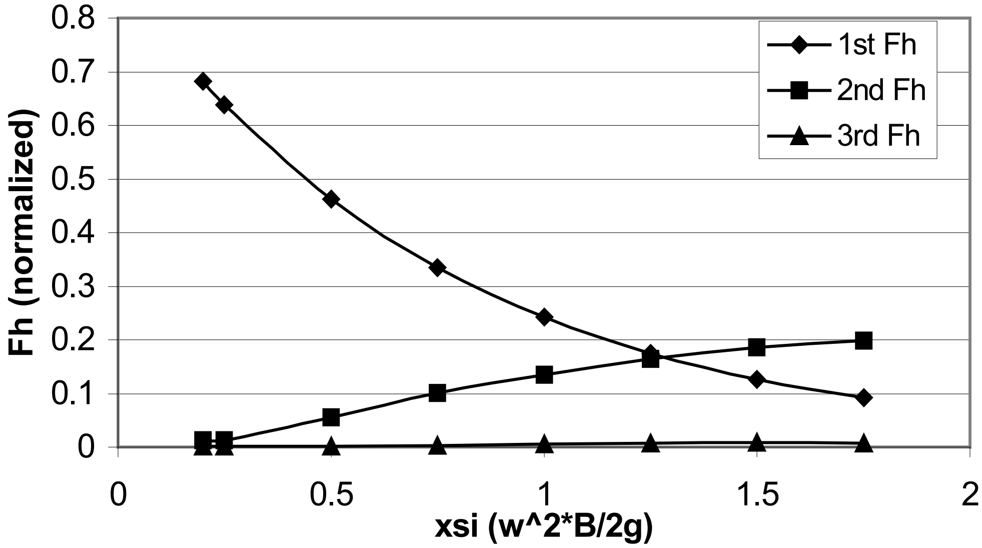

Figure 36. Comparison of heave force components with H=0.07 (See Figure 29).

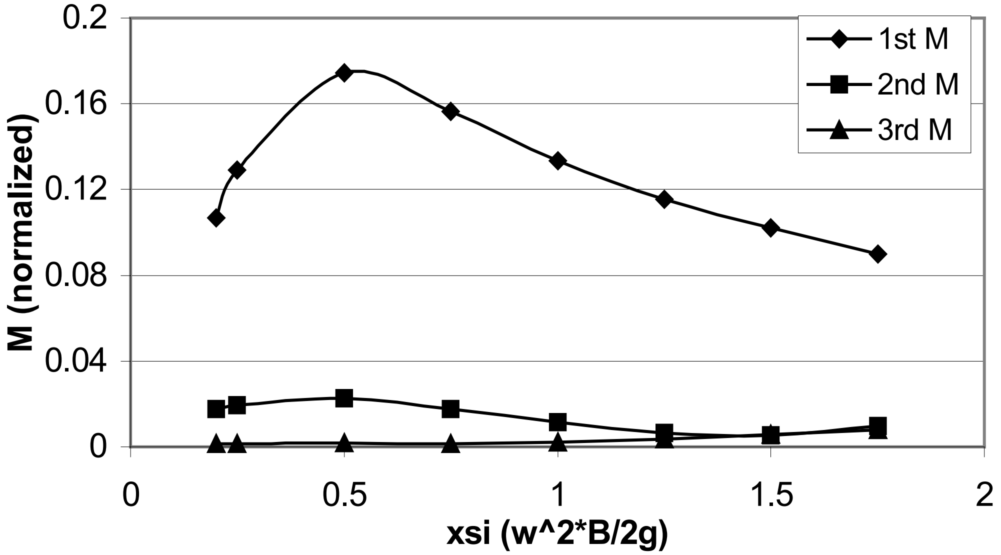

Figure 37. Comparison of roll moment components with H=0.07m (See Figure 30).

4.3.2. Dual barge

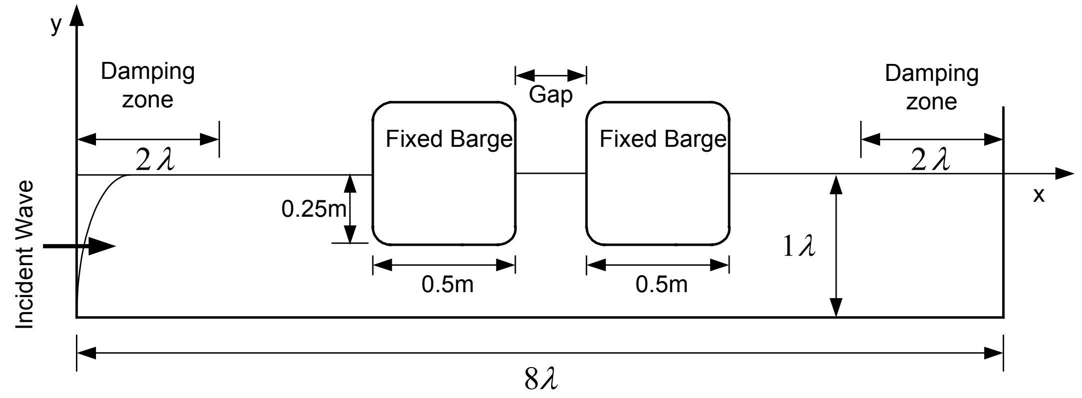

Figure 38. Sketch of surface piercing dual barge simulation

After the confirmation of single fixed barge calculation, we can consider dual fixed barge-type structure with the same condition as single barge case (see Figure 38). This situation is more realistic for production and offloading in offshore and coastal area. Dual structure also represents Tension Leg Platform (TLP), which has two floating columns in 2D.

Figure 39 shows the comparison between the mean horizontal forces for dual barge and the single barge against various incident wave frequency areas. In low frequency region (xsi=0.25), front barge has negative mean horizontal force and rear barge has positive force. As wavelength decreases, i.e. wave frequency increases, the mean force of front barge follows the single body case. This phenomenon may be explained by the interaction of incident wavelength and piercing body width. Surface piercing body can be greatly influenced by incident wavelength so that wave forces for dual barge can be different from single barge case. As incident wavelength decreases, the effect of incoming waves for rear body decreases because of the front body. It means that most of wave energy works with front body in case of short waves. As we observed before, for the fully submerged dual cylinder, front and rear cylinders try to pull each other. Interestingly, surface piercing dual structure case is vice versa.

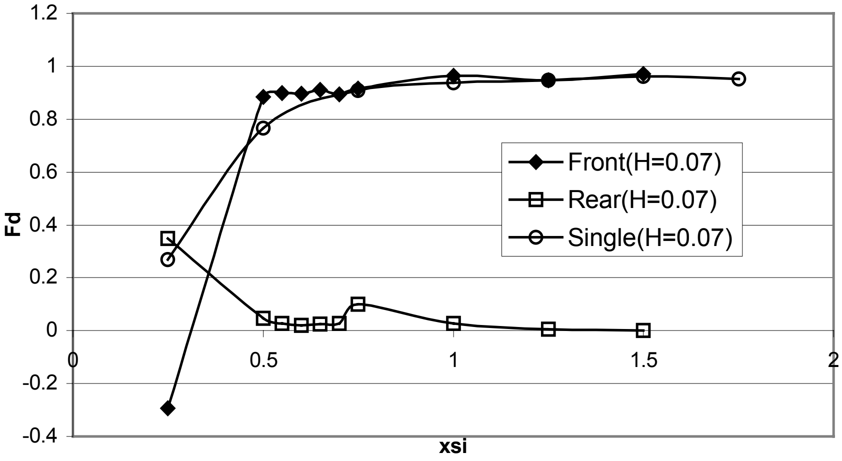

Figure 39. Mean sway force for dual barge with H=0.07m, Gap=2B (1m) (See Figure 27).

Figure 40 shows first harmonic horizontal forces for dual barge plotted against various incident wave frequencies. Rear barge has a bigger horizontal force than the front barge at low frequency (xsi=0.25) and the force of single barge case is placed in between both barges. As the wave frequency increases, front barge force tends to follow single barge case and rear barge force decreases to zero. When wave frequency is between xsi=0.5 and 0.75 (2.1m < L < 3.14m), some interactions of wave and dual body can be observed.

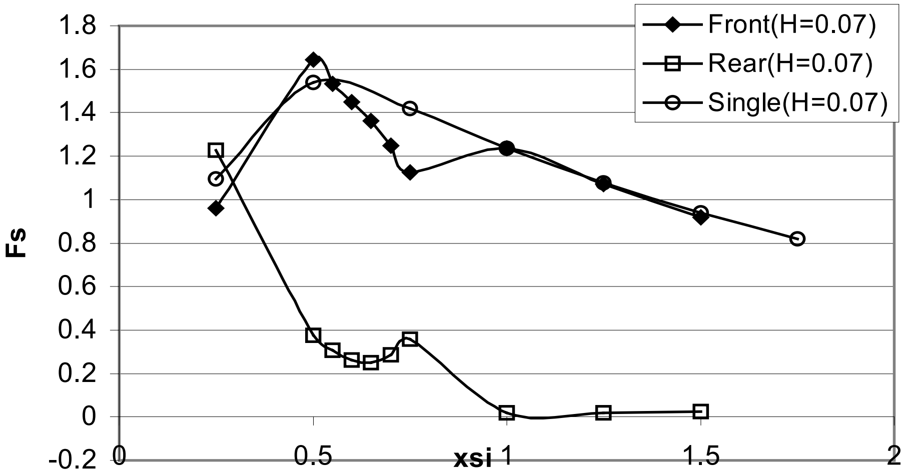

Figure 40. 1st harmonic sway force with H=0.07, Gap=2B (See Figure 28).

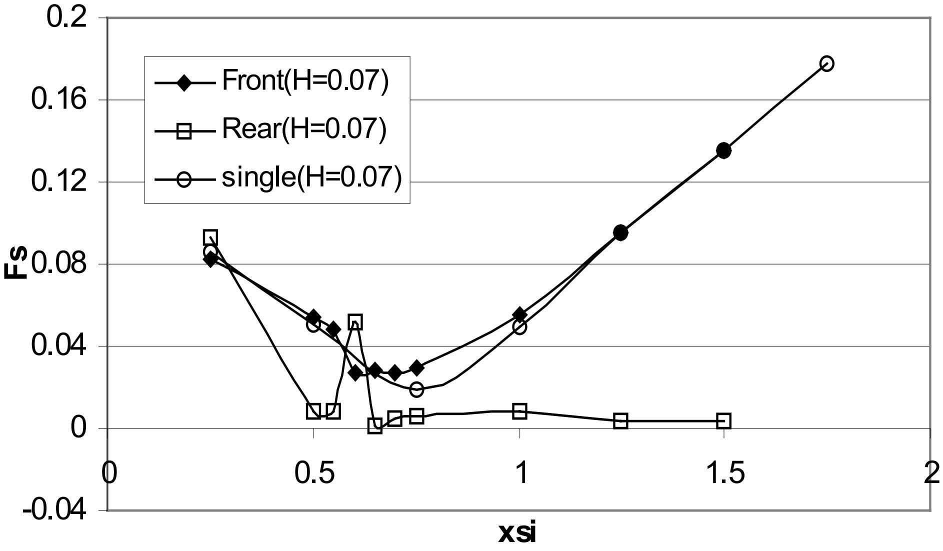

Figure 41. 2nd harmonic sway force of dual barge (See Figure 28).

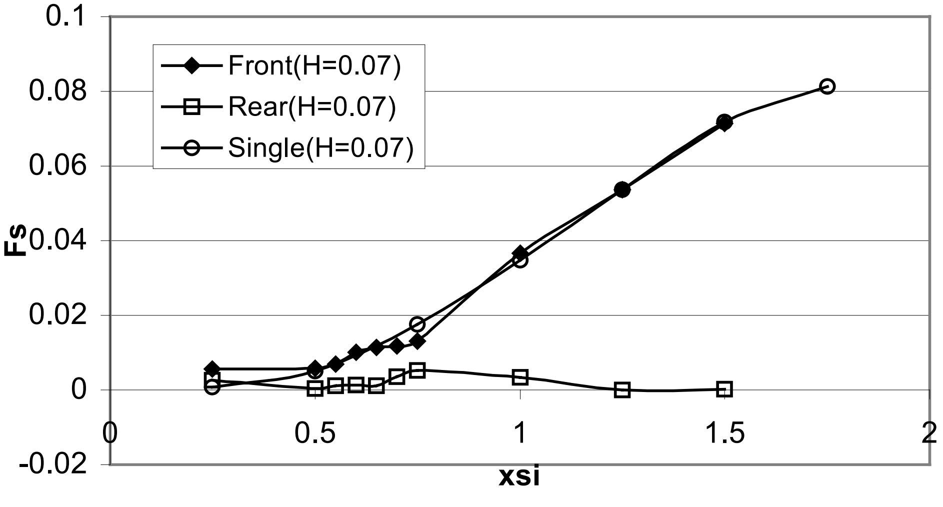

Figure 42. 3rd harmonic sway force of dual barge (See Figure 28).

2nd and 3rd order sway forces are shown in the Figure 41 and Figure 42. For the second harmonic force, rear barge force is bigger than front barge force at xsi=0.6

(L=2.6m). It can be expected that the rear structure is strongly influenced by incident wave at this frequency. As wave frequency increases, 2nd and 3rd harmonic forces of the front body are close to single body and the force of the rear body goes to zero. The incident wave effect can be gradually reduced on the rear structure as the wave frequency increases, i.e. wavelength becomes shorter and most of the incident wave energy can be used on the front structure.

From Figure 43 to Figure 45, a series of heave (vertical) force components for dual barge is plotted and compared with single body case. Similar to horizontal force components, there exists a strong wave-body interaction zone (0.5 < xsi < 0.8). The range of incident wavelength for these frequencies is about 2-3m. Compared to the structure width (each body width=0.5m, and gap=1m), the maximum wave-body interactions occurred when the incident wavelength is about same or 1.5 times bigger than structure width (from first body to rear body). At high frequency area, rear body has been little effected from incident waves, while front body has taken most of the incident wave energy.

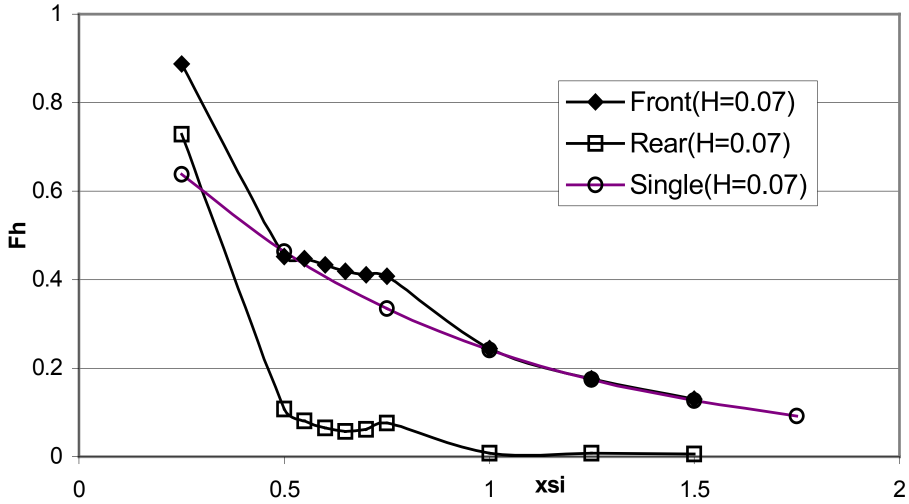

Figure 43. 1st harmonic heave force of dual barge (See Figure 29).

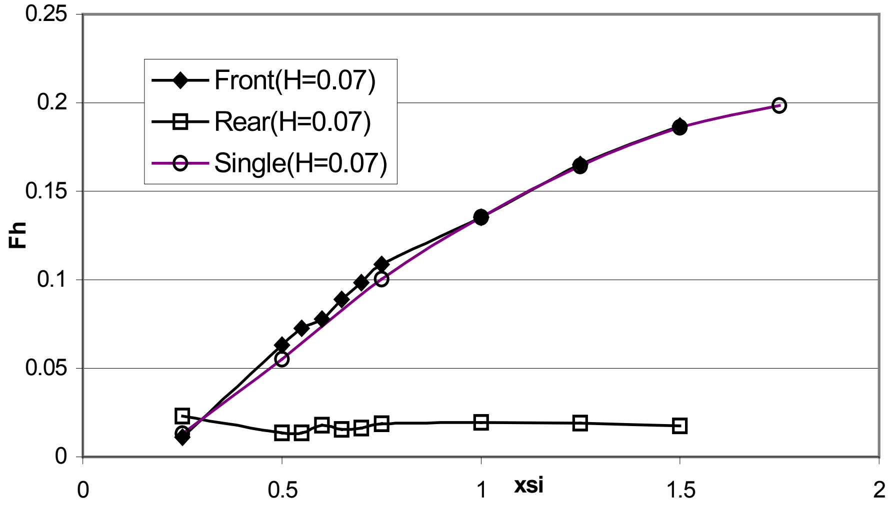

Figure 44. 2nd harmonic heave force of dual barge (See Figure 29).

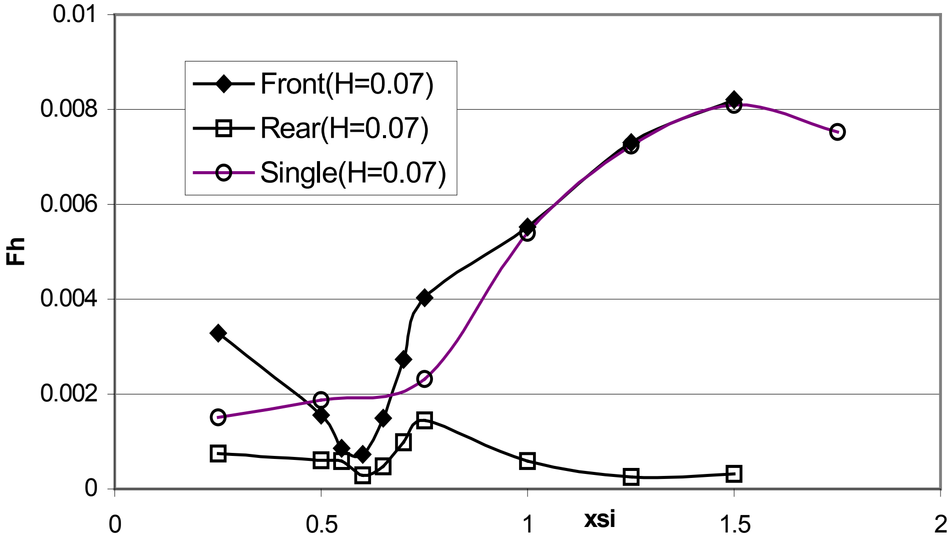

Figure 45. 3rd harmonic heave force of dual barge (See Figure 29).

A series of roll moment component for dual barge is plotted and compared with single body case in Figure 46 through Figure 48. Similar to other force components, a strong wave-body interaction frequency zone (2m < λ < 3m) can be observed. From Figure 49 to Figure 51, mean drift force and a series of horizontal force components are plotted with a certain wave frequency (L=2.09m) against various body gap between front and rear structure. Mean drift force and 1st order force of both barges have some fluctuation in accordance with various gaps. For instance, when the gap is 1m or 2m, 1st order force of front barge has a minimum, where as rear barge has a maximum force. This phenomenon can be explained from the relation of wavelength and structure width. If the gap is 1m and each barge width is 0.5m, the total distance from front barge wall and rear barge wall is about 2m. When the total structure width including gap distance is same as incoming waves (=2m), maximum mean drift force has occurred on the rear structure. The magnitude of 2nd and 3rd harmonic forces for front body fluctuates depending on wavelength. Interestingly, these forces have opposite trend, for instance, maximum value of 2nd order force was observed, when the minimum of 3rd order force occurs.

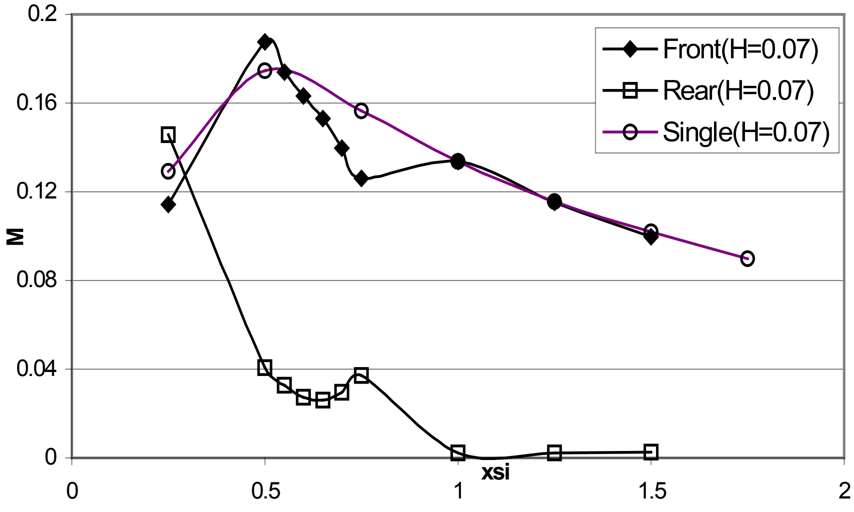

Figure 46. 1st harmonic moment of dual barge (See Figure 30).

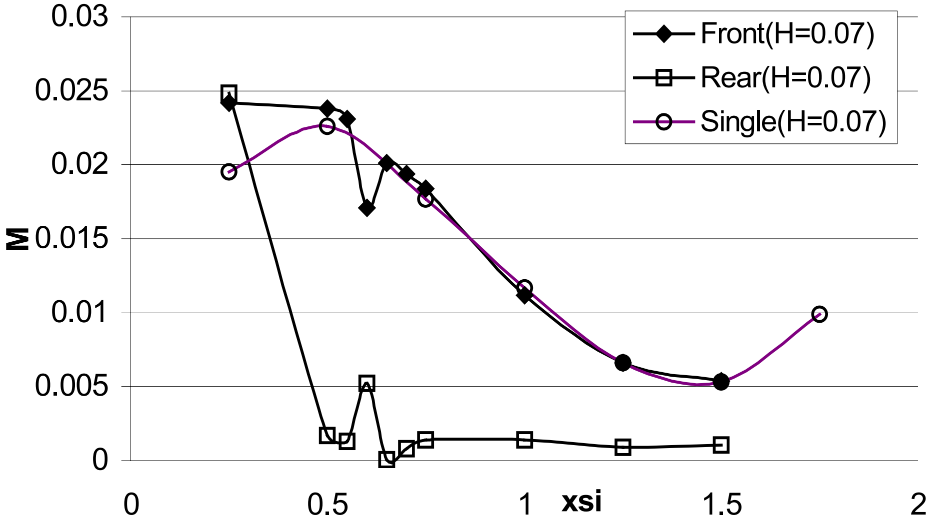

Figure 47. 2nd harmonic moment of dual barge (See Figure 30).

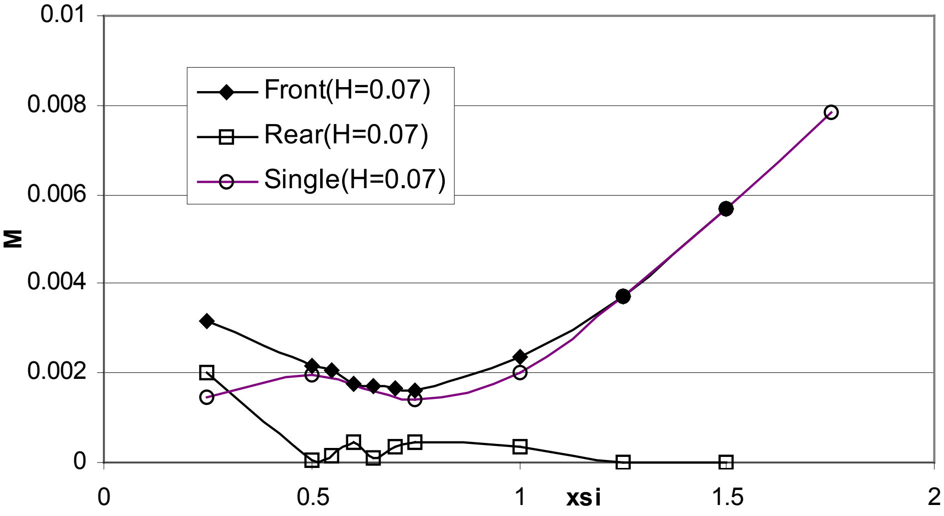

Figure 48. 3rd harmonic moment of dual barge (See Figure 30).

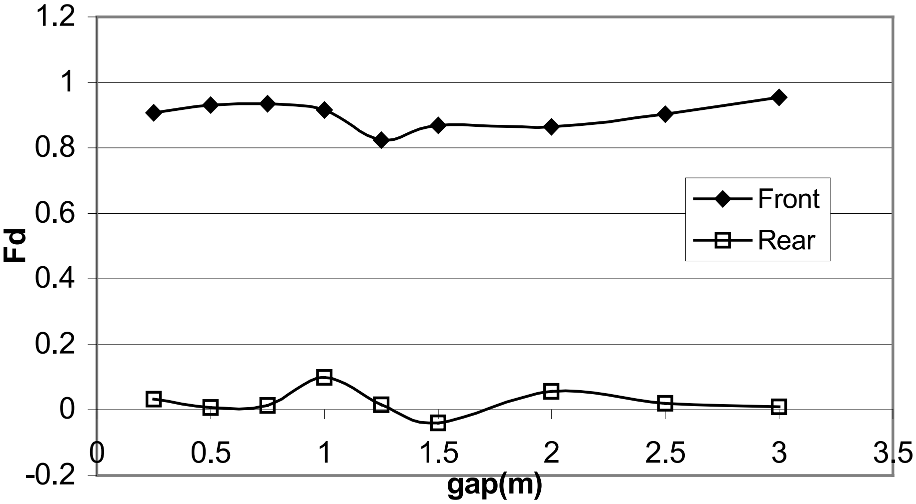

Figure 49. Mean drift force against various gaps with xsi=0.75 (L=2.09m) and H=0.07m. Fd is normalized by $0.5\rho g L(\frac{H}{2})^2$.

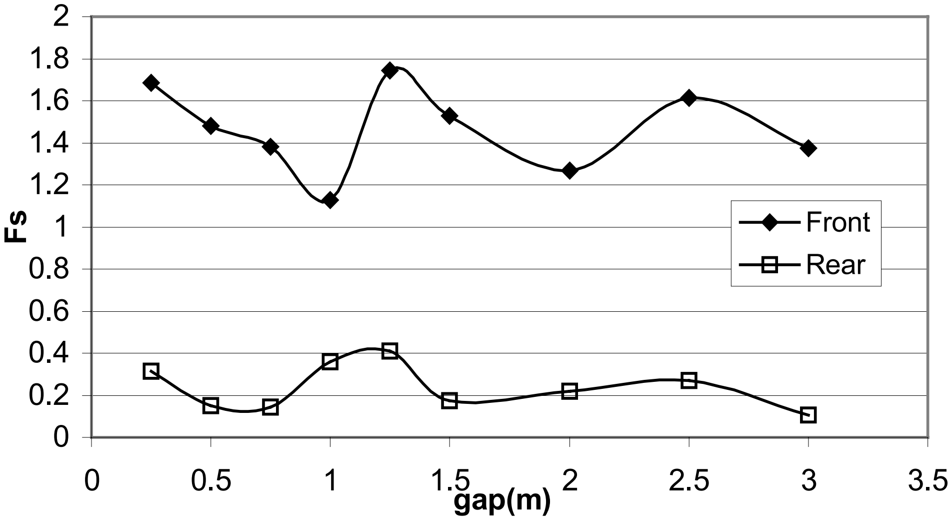

Figure 50. 1st harmonic sway force against various gaps with xsi=0.75 (L=2.09m) and H=0.07m. Fs is normalized by $\rho g L d(\frac{H}{2})$.

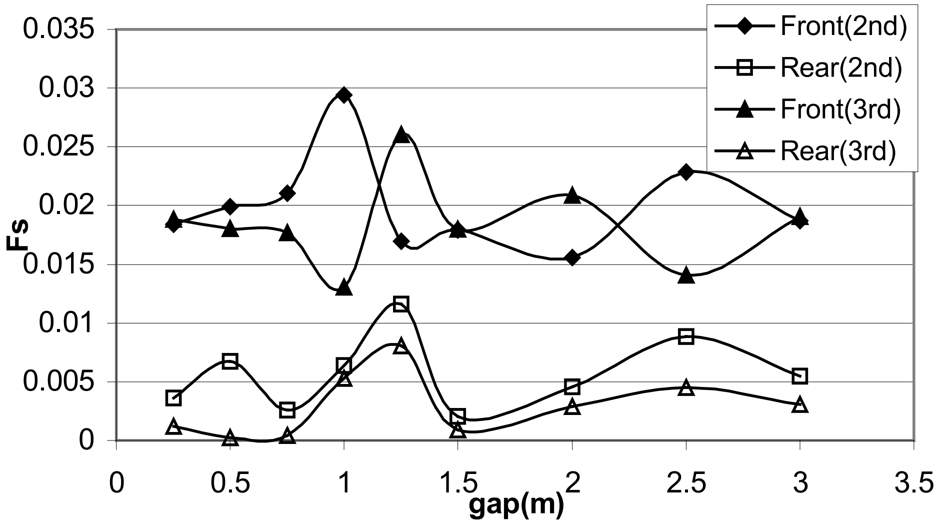

Figure 51. 2^{nd} and 3^{rd} harmonic sway force against various gaps (See Figure 50).

From Figure 52 and Figure 53, heave (vertical) force components are shown against various gaps. Compared to sway force components, 1^{st} order force of front body has maximum value when the gap equals to 1m or 2m, which is opposite to sway force (See Figure 50). Higher components of heave force are shown in the Figure 53. The magnitude of 3^{rd} order heave force is much smaller than that of 2^{nd} order, while the magnitude of 2^{nd} and 3^{rd} harmonic horizontal forces are of same order.

Figure 54 and Figure 55 show the plot of roll moment components. The fluctuation of 1^{st} order moment is similar to sway case, i.e. maximum values appeared when gap=1m or 2m. Compared with 1^{st} order moment, higher order components shown in Figure 55 are not significant. 2^{nd} order moment for front body is only 10% of 1^{st} order magnitude.

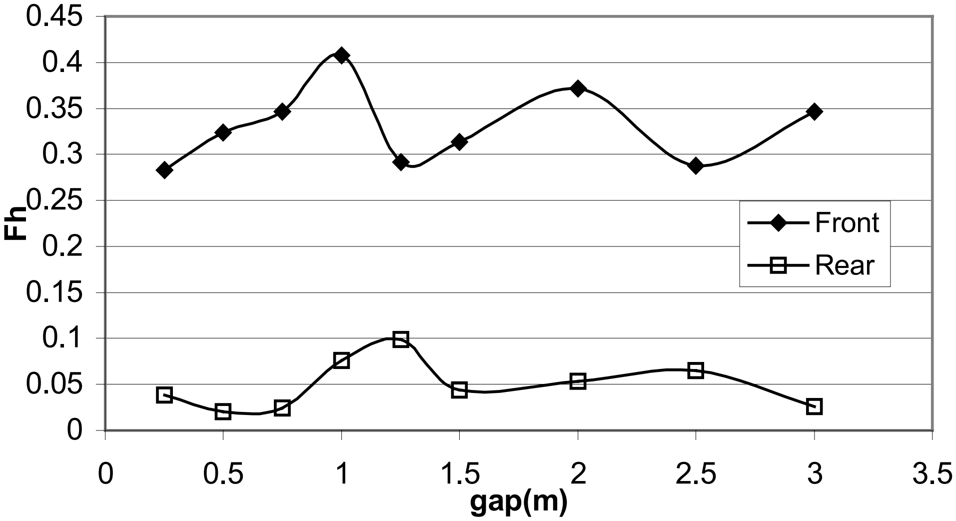

Figure 52. 1st harmonic heave force normalized by $\rho gLB(\frac{H}{2})$ with xsi=0.75 (L=2.09m) and H=0.07m.

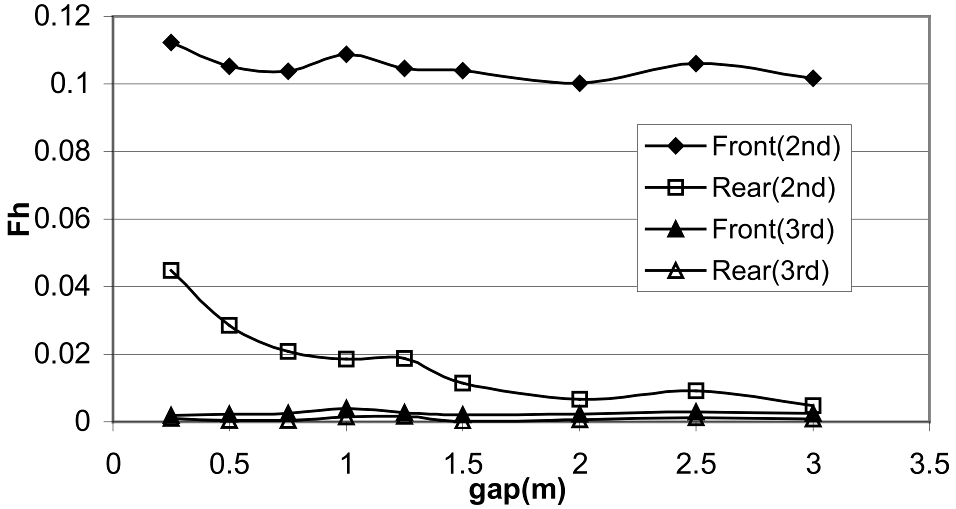

Figure 53. Second and third harmonic heave force (See Figure 52).

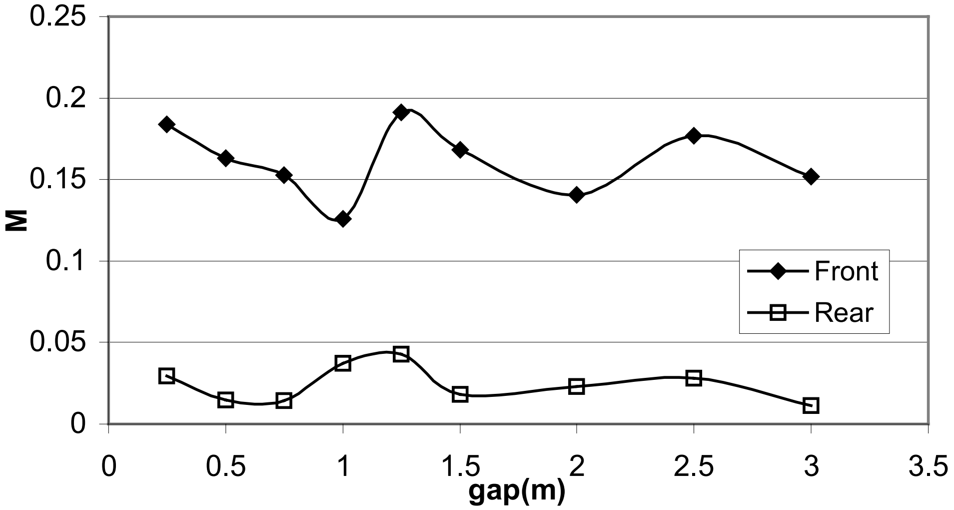

Figure 54. 1st harmonic moment against various gaps with xsi=0.75 (L=2.09m) and H=0.07m. M is normalized by $\rho gLBd(\frac{H}{2})$, where L=1 (for 2D).

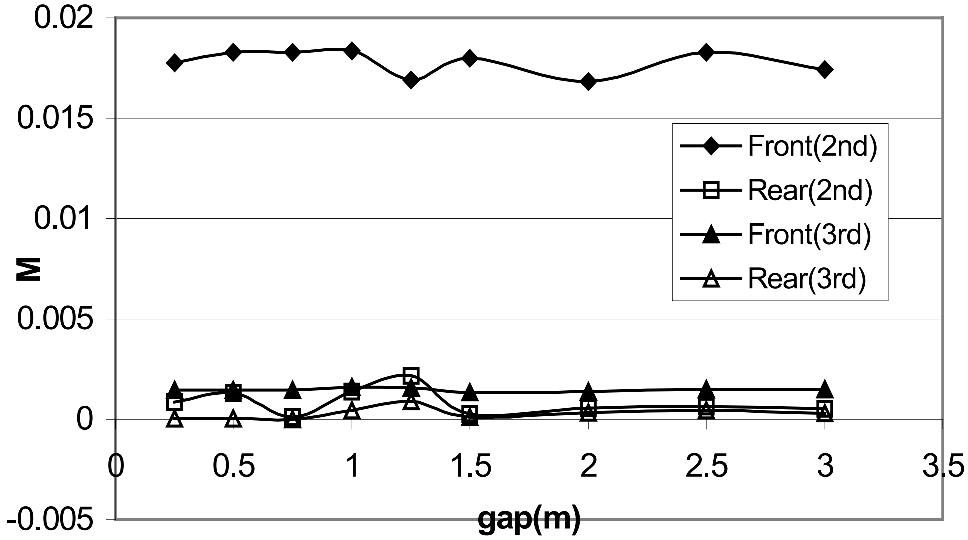

Figure 55. 2^{nd} and 3rd harmonic moment (See Figure 54).

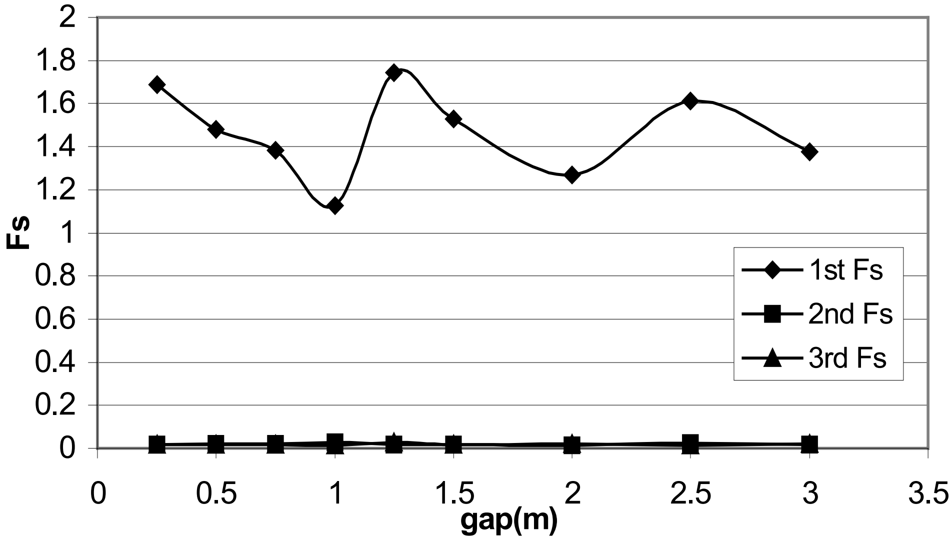

Figure 56. Sway force components of front barge (See Figure 50).

From Figure 56 to Figure 61, the magnitude comparison for each force component is plotted. For sway force of dual barge, the magnitude of 1^{st} order is much bigger than 2^{nd} and 3^{rd} harmonic forces. However, the magnitude of 2^{nd} order heave force is not small. In particular, 2^{nd} order heave force of front body is constant against various gap. It means that higher order heave force for front body is independent of gap variation. 2^{nd} order heave force of rear body is even bigger than 1^{st} order component at low frequency area. In the moment comparison, similar phenomenon is observed. 2^{nd} order moment of front body is constant and can not be neglected when compared with sway force component.

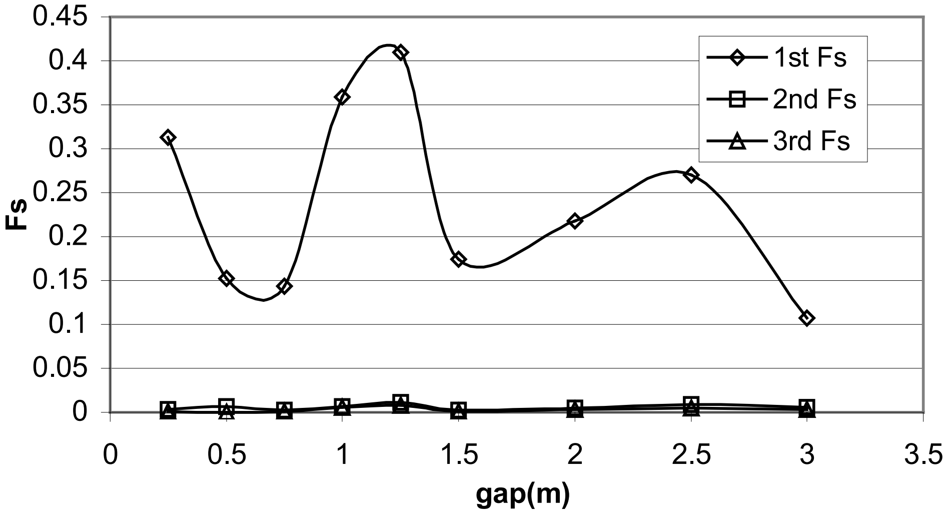

Figure 57. Sway force components of rear barge (See Figure 50).

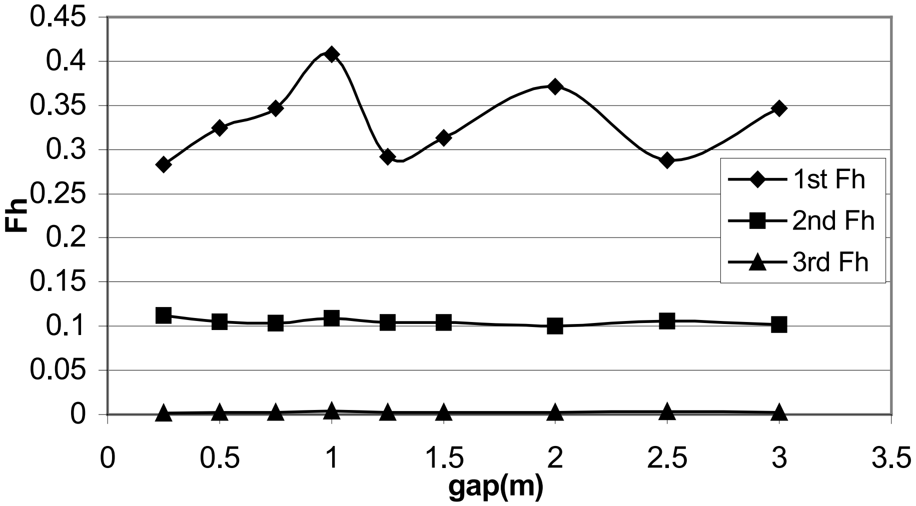

Figure 58. Heave force components of front barge (See Figure 52).

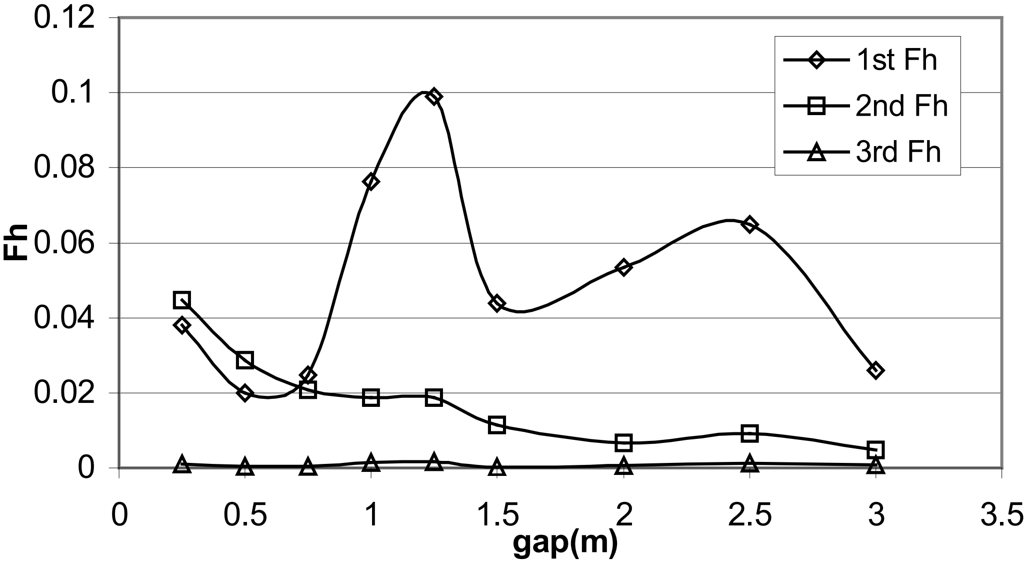

Figure 59. Heave force components of rear barge (See Figure 52).

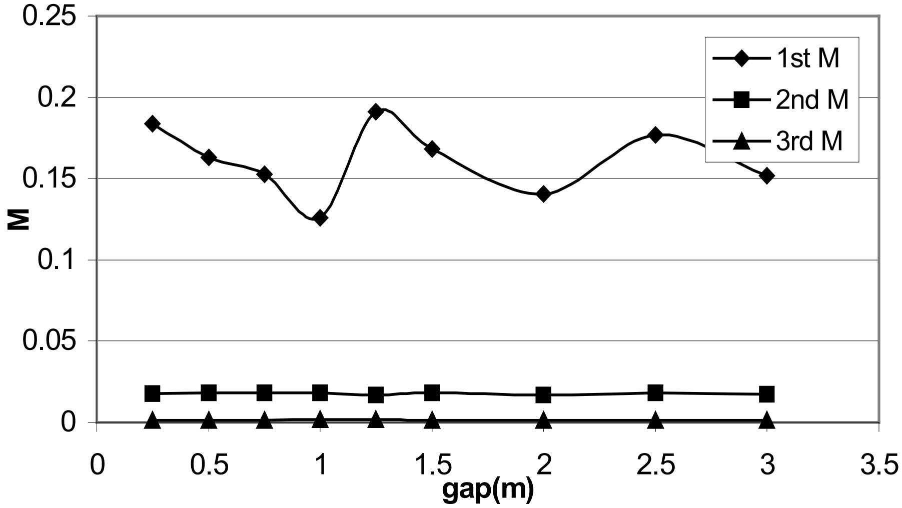

Figure 60. Roll moment components of front barge (See Figure 54).

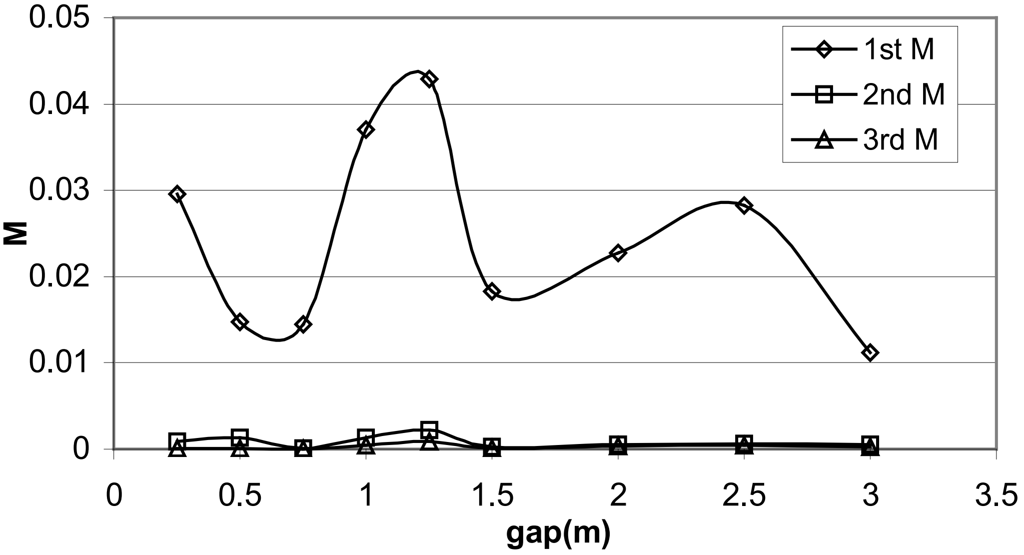

Figure 61. Roll moment components of rear barge (See Figure 54).

4.4. Wedge type wave maker by forced motion

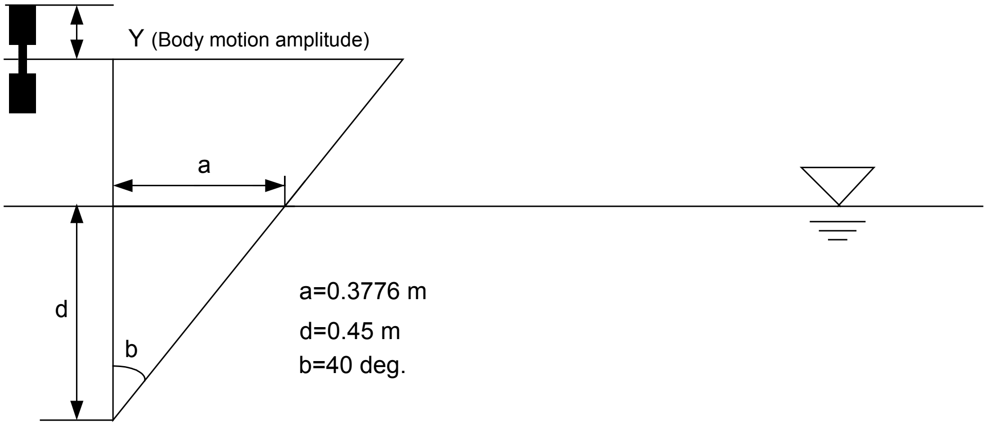

Figure 62. Sketch of wedge type wave maker by forced motion (prescribed motion).

4.4.1. Convergence test

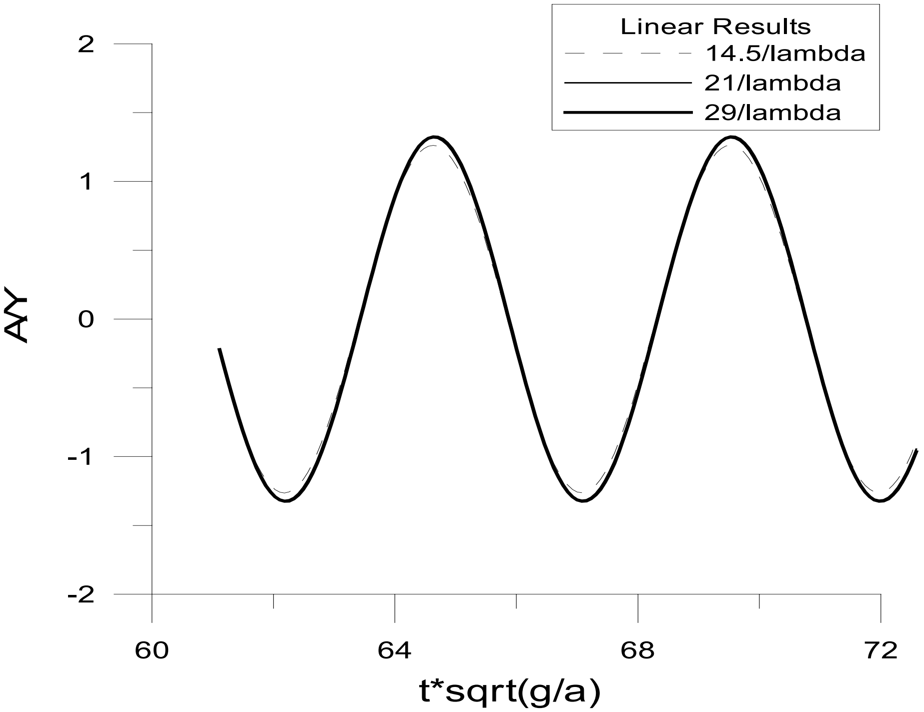

Figure 63. Comparison of linear wave elevation with different number of node per wavelength. Oscillation period (T/sqrt(g/a))=4.895 and amplitude (Y/a)=0.0988, A is wave amplitude.

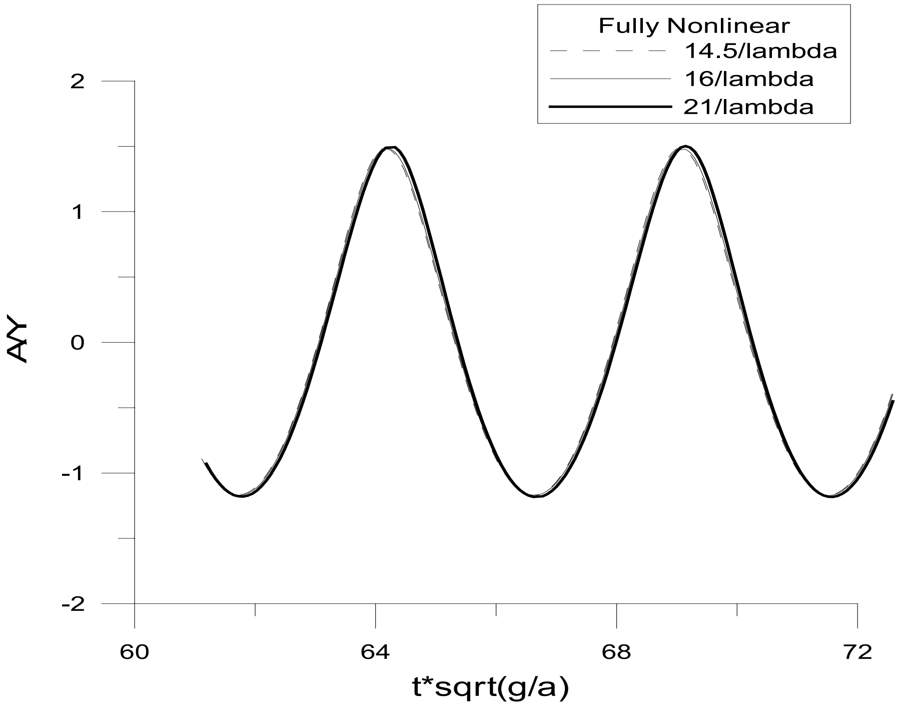

Figure 64. Comparison of nonlinear wave amplitude with different node number per one wavelength. Other conditions are same as Figure 63 .

This section gives the simulation of wedge type wave maker with forced motion. Figure 62 shows the sketch of this case and gives geometric information of wave maker. Convergence test for linear calculation of wave generation is shown in Figure 63 and Figure 64. From the convergence test, 21 node per wavelength is enough for this case. However, for fully nonlinear calculation with material node approach, due to the free surface node movement along with water particle velocity, convergent result is different. Even if the number of node is 14.5 per wavelength, the result is closely matched with 21 nodes per wavelength. By following water particle velocity, free surface node can be exactly represented for fully nonlinear simulation. Therefore, when the number of node per wavelength is more than 14.5, the numerical results converge appreciably. Note that this convergence test is only valid for the prescribed motion problem, which have relatively high frequency body motion. Convergence test can be carried out for each case. Other convergence test in case of freely floating body simulation will be shown in next section.

Acceleration potential method was utilized to calculate ϕ_t for prescribed motion of wave maker. For using mode decomposition method, q_B term in Equation (54) can be simplified as $\frac{\partial\phi}{\partial n}\frac{\partial^2\phi}{\partial s^2}$, where $k_n = 0$, $\omega = 0$, and $\frac{\partial}{\partial s}\left(\frac{\partial\phi}{\partial n}\right) = \frac{\partial}{\partial s}\left(\upsilon_z n_z\right) = 0$, because of straight body surface. Therefore, boundary condition of ϕ_t on body surface is $\frac{\partial\phi_t}{\partial n} = a_z n_z + \frac{\partial\phi}{\partial n}\left(\frac{\partial^2\phi}{\partial s^2}\right)$.

4.4.2. Comparison with experimental results

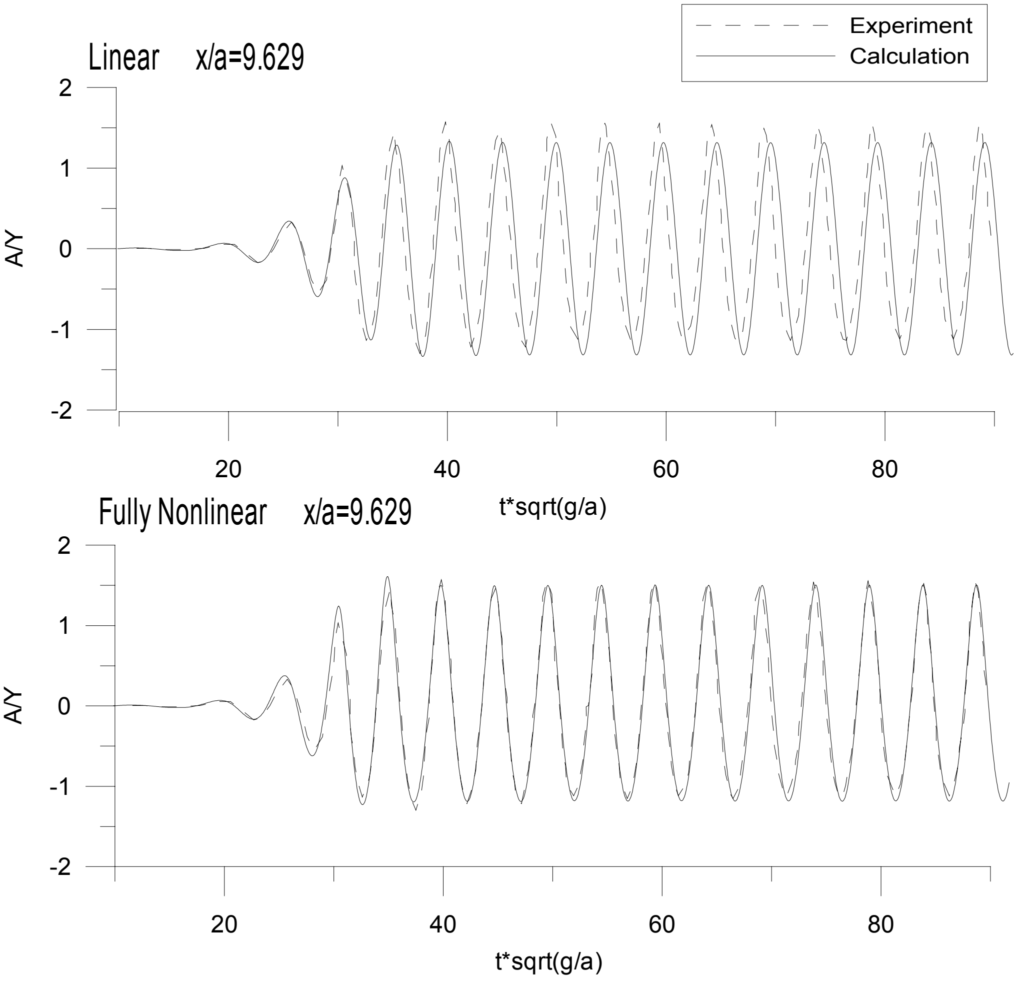

Figure 65. Comparison of surface elevation at x/a=9.629 with numerical and experimental results. Oscillation period (T/sqrt(g/a))=4.895 and amplitude (Y/a)=0.0988 (dt=T/64, 22 node per lambda).

Comparison of surface elevation of numerical calculation and experimental results of Kashiwagi (1996) are shown in the Figure 65 and Figure 66. There is a big deviation of wave elevation and phase between linear calculation and experimental results. The results of fully nonlinear calculation are in good agreement with experimental result both in surface elevation and phase. In this study, material node approach as a time marching scheme was used. For verification of different numerical scheme, material node approach and semi-lagrangian method are compared in the Figure 67.

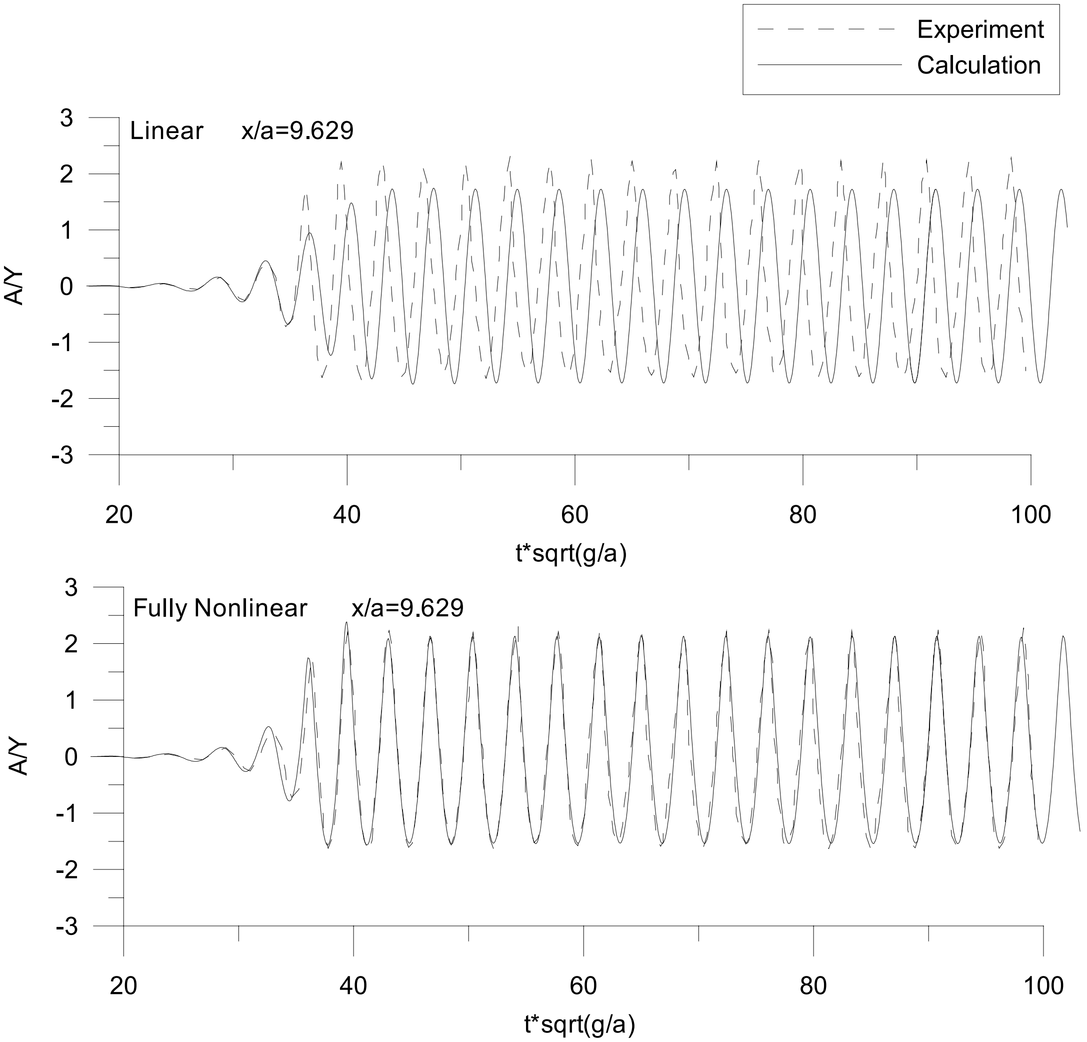

Figure 66. Comparison of surface elevation at x/a=9.629. Oscillation period is T/sqrt(g/a)=3.671 and amplitude Y/a=0.0525 (dt=T/64, 20 node per lambda).

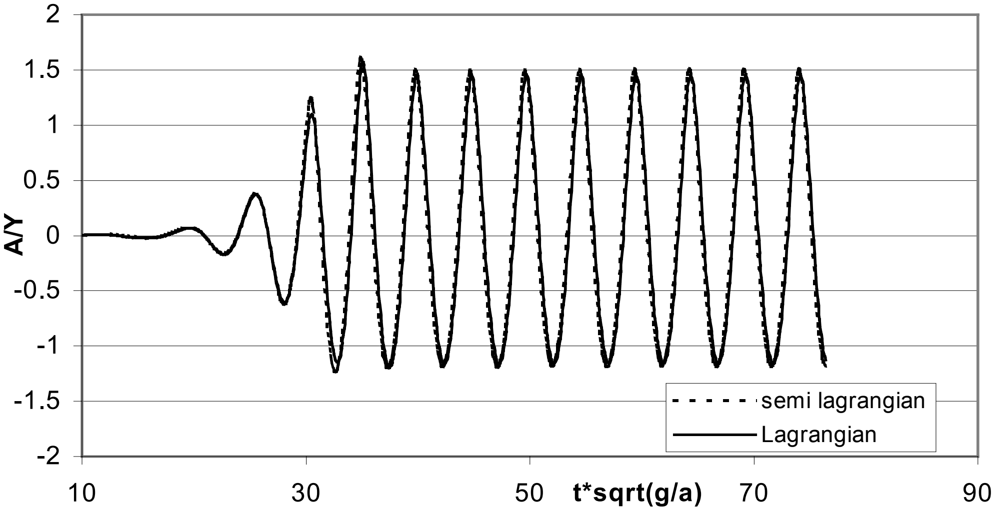

Figure 67. Comparison of surface elevation at x/a=9.629 with two different numerical schemes. Oscillation period is T/sqrt(g/a)=4.895 and amplitude Y/a=0.0988.

4.4.3. Comparison with benchmark test results

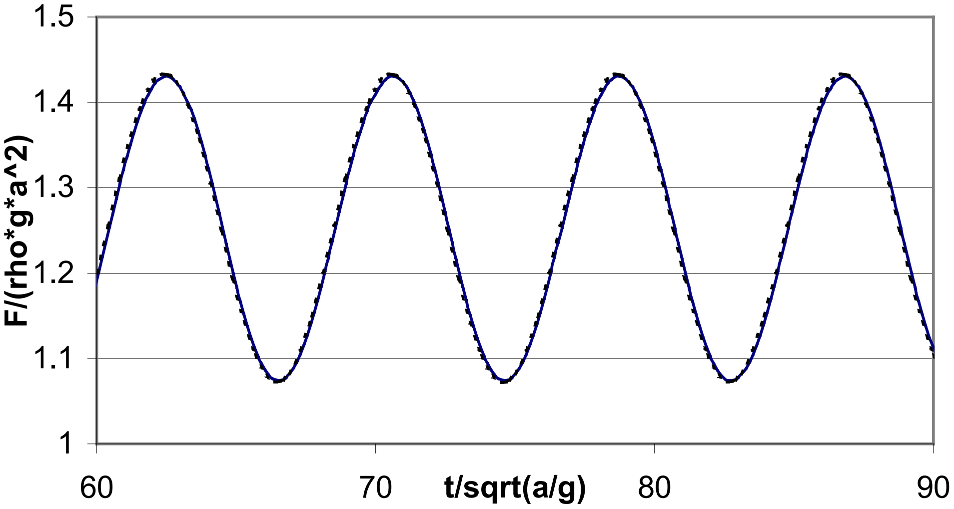

Figure 68. Comparison of wave force induced by heaving motion. Dashed line=tanizawa's benchmark results, solid line=present results. (A/a=0.2, w^2*a/g=0.6, where A=stroke amplitude).

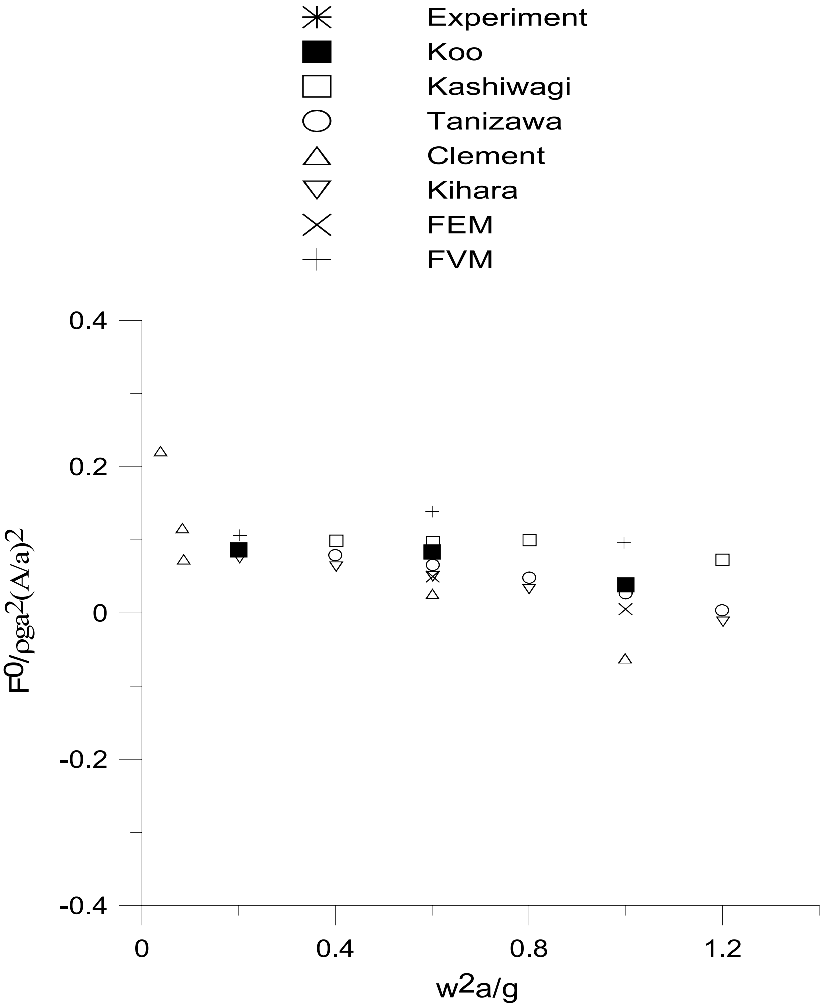

Figure 69. Mean body force on the wedge type wave maker (a/d=0.4) with heaving motion (A/a=0.2).

For verification of added mass and damping coefficient due to heave motion of wedge type wave maker, benchmark test (Tanizawa & Clement, 1999) achieved by many authors, can be used. To calculate added mass and radiation damping, time series of body (wave maker) force is utilized and compared with other numerical results. Both numerical results agree well each other in the Figure 68. From Figure 69 to Figure 73, mean force and a series of force components are plotted and compared with all benchmark results including experimental results. Present results are in good agreement with those benchmark results. Therefore, the numerical results for prescribed body motion has been successfully proved.

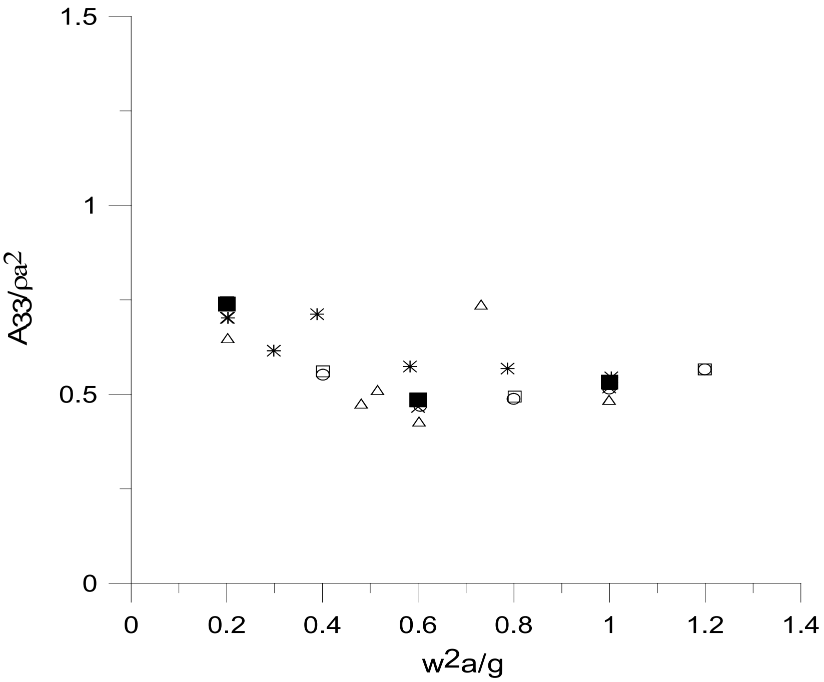

Figure 70. Added mass of wave maker with heaving motion (See Figure 69).

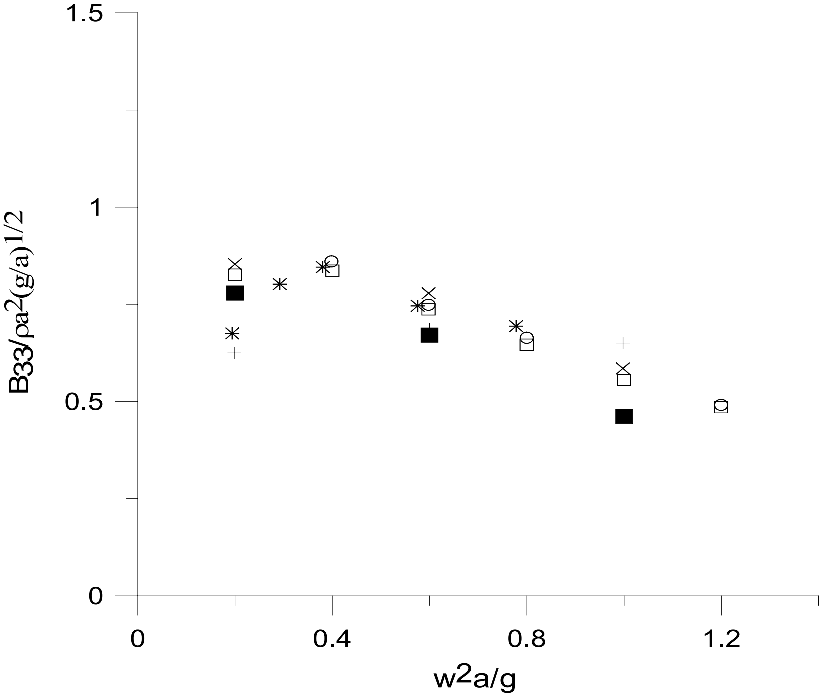

Figure 71. Damping coefficient of wave maker with heaving motion (See Figure 69).

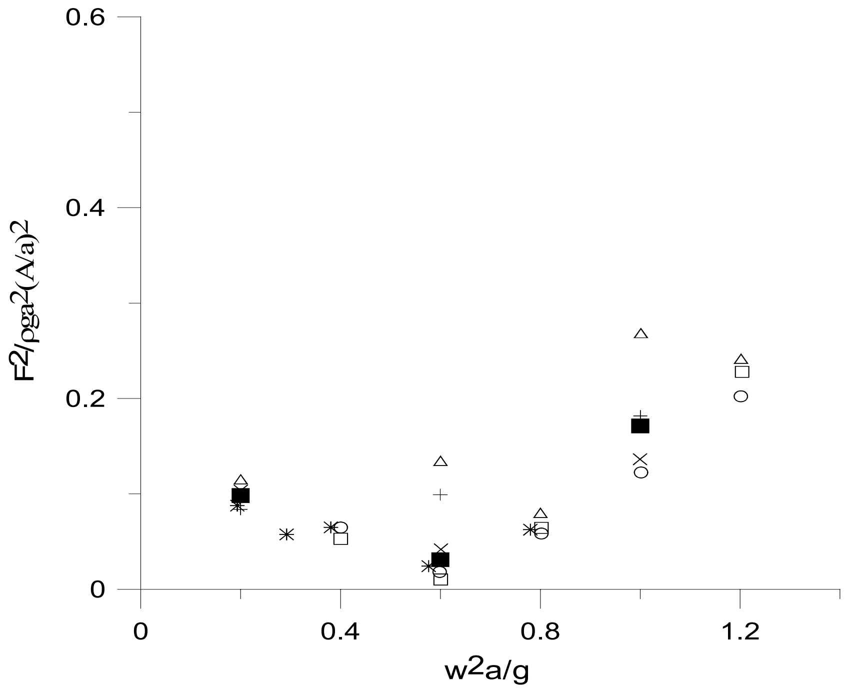

Figure 72. 2nd harmonic force on the wave maker (See Figure 69).

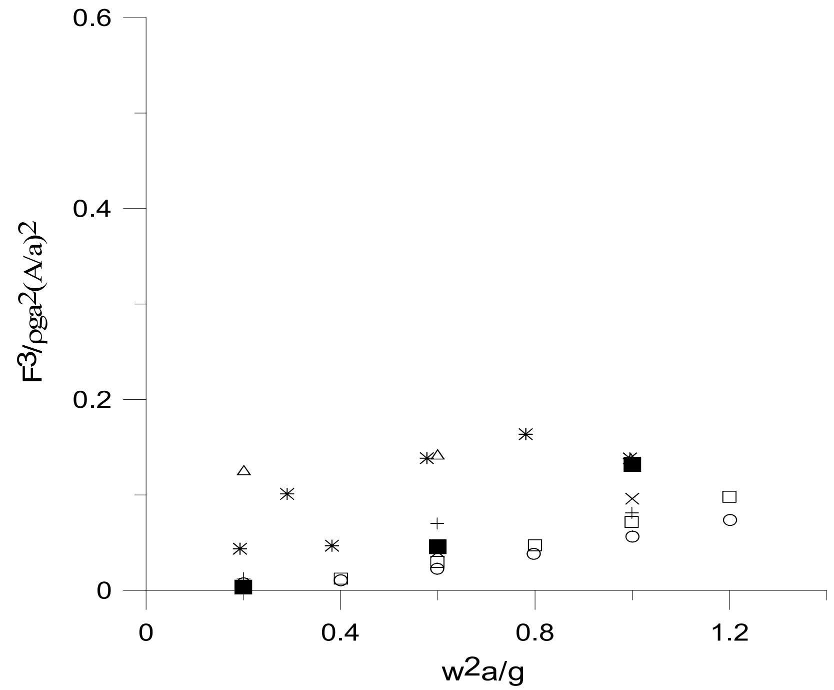

Figure 73. 3rd harmonic force on the wave maker (See Figure 69).

4.4.4. Comparison of different methods (body nonlinear)

In order to investigate the effect of nonlinear free surface elevation against the body, the results of fully nonlinear simulations can be compared with those of body nonlinear calculations. Body nonlinear simulation means that moving body boundary conditions are used with linear free surface boundary conditions, for instance, wedge type wave maker is moving with prescribed motion but free surface nodes are stationary assuming that the nodes on the free surface are placed on the mean position (SWL).

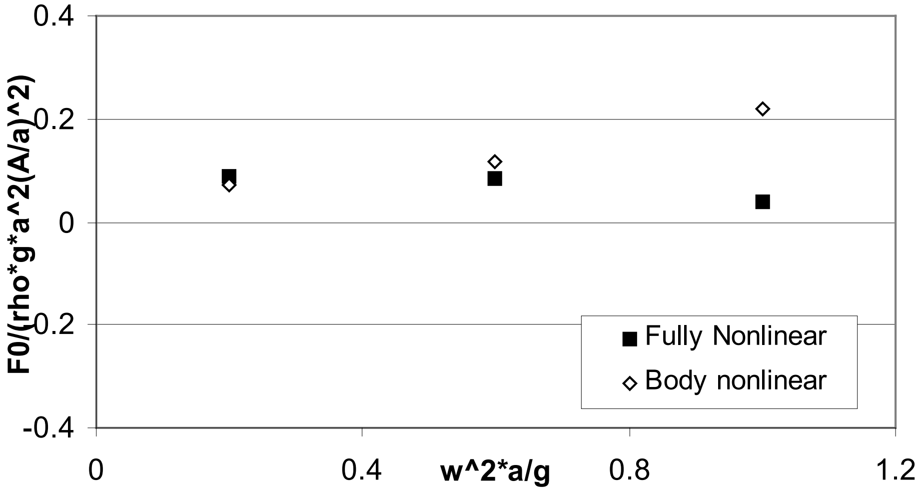

Figure 74. Mean drift force comparison with different methods. Calculation condition is same as Figure 69.

Figure 74 shows the comparison of mean drift force for fully nonlinear and body-nonlinear results. As the frequency of wave maker motion increases, the magnitude of body nonlinear mean force becomes larger as compared to fully nonlinear calculation. Fully nonlinear mean forces reduce slightly as the motion frequency increases. From Figure 74, it can be seen that body nonlinear calculation is not suitable for high frequency of body motion analysis, as the free surface movement has to be taken into account when body moves faster. This means that the update of free surface elevation becomes important for high frequency stroke motion. The comparison of added mass and radiation-damping coefficient for moving body is shown in Figure 75 and Figure 76. 1st order forces of fully nonlinear and body nonlinear methods are identical. 2nd harmonic force comparison shown in Figure 77, shows no big difference between both methods. However, in Figure 78, the comparison of 3rd harmonic force shows a significant deviation between two methods when the body has high frequency prescribed motion.

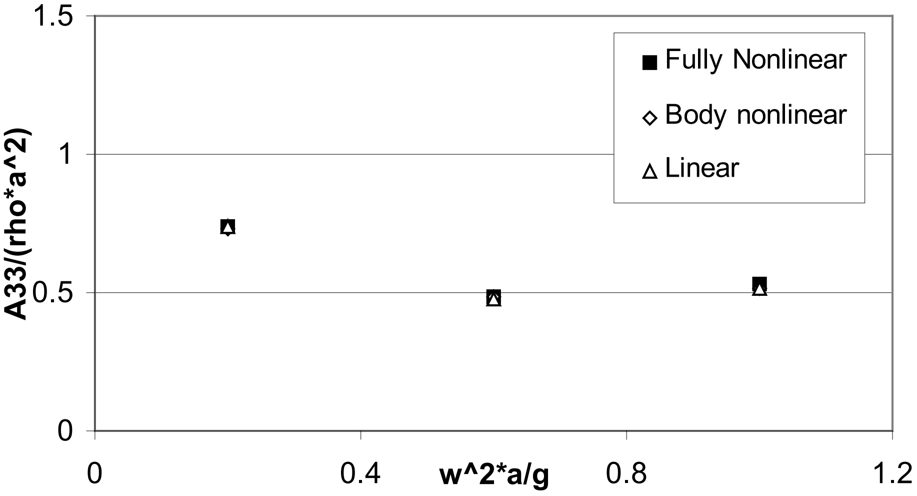

Figure 75. Added mass comparison with different methods. Calculation condition is same as Figure 69.

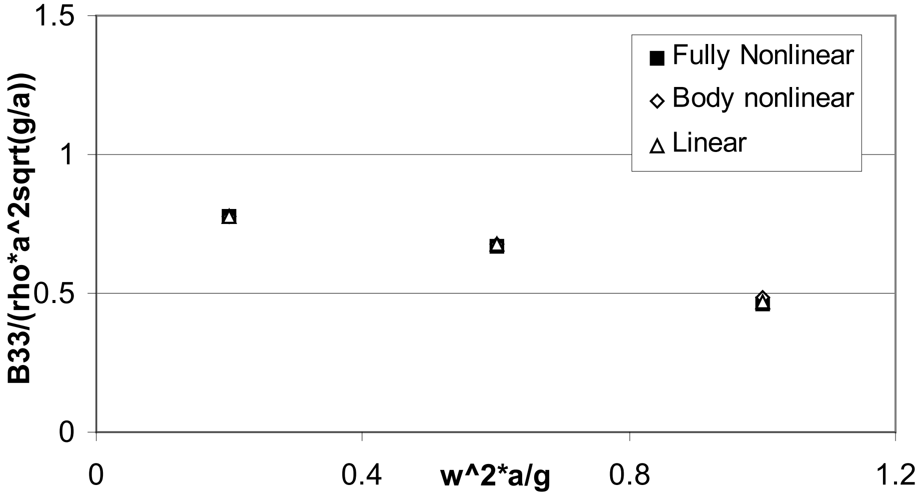

Figure 76. Damping coefficients comparison with different methods. Calculation condition is same as Figure 69.

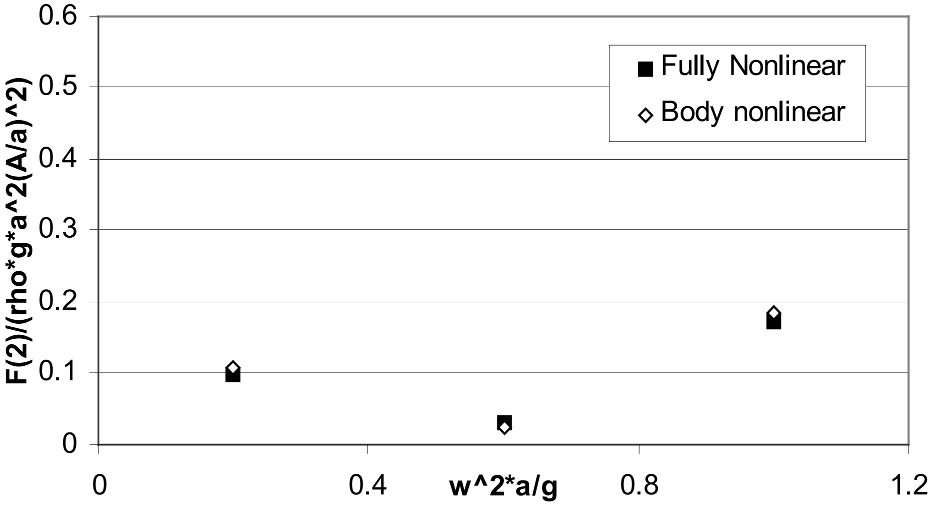

Figure 77. 2nd Harmonic force comparison with different methods. Calculation condition is same as Figure 69.

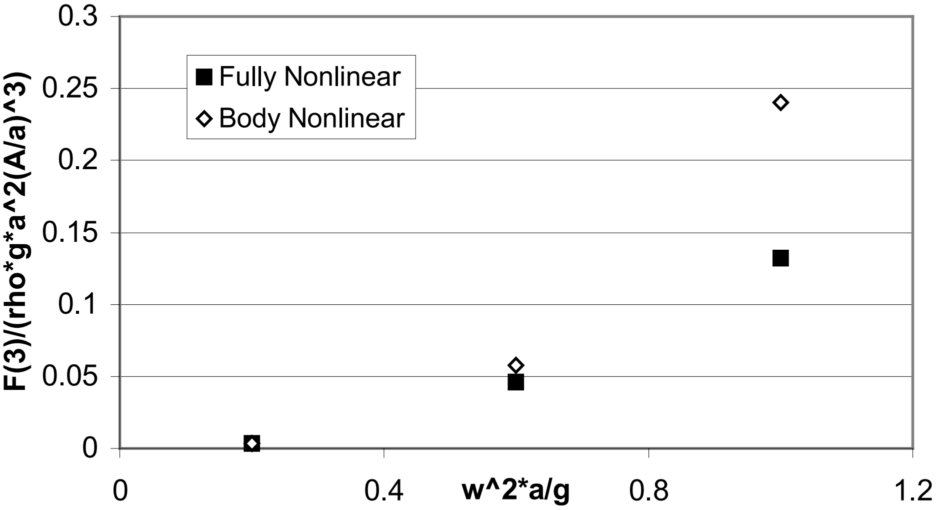

Figure 78. 3rd Harmonic force comparison with different methods. Calculation condition is same as Figure 69.

4.5. Freely floating body motions induced by waves

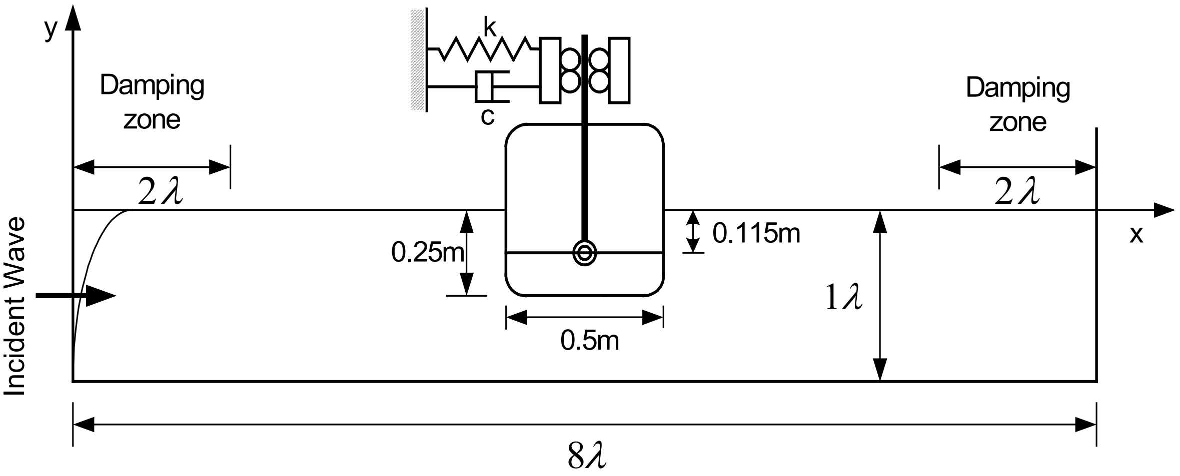

Figure 79. Sketch of freely floating barge motion with spring type mooring. Center of gravity=0.115m below SWL, spring constant=197.58N/m, damping coefficient=19.8 N/m/s, draft (d)=0.25m, width (B)=0.5m.

Freely floating body motion analysis is combined with diffraction and radiation problem. Before we consider floating body motion, we have already confirmed the results of diffraction problem of the surface piercing fixed body calculation, and radiation problem of the wedge-type wave maker analysis. Freely floating body motion analysis is the most difficult numerical problem and it is the final goal for the Numerical Wave Tank simulation. Without guaranty of each numerical scheme for various situations, we can't expect correct floating body motions and corresponding wave force. In this section, we confirm the method of time marching scheme, show the time series of each motion, and compare RAO for each motion with experiment and other numerical results, which were done by Tanizawa and Minami (1998). In addition, we investigate the floating body motion and wave force near the resonance frequency area. From the investigation, the effect of nonlinear waves against body motion can be clearly understood by the comparison of body nonlinear and fully nonlinear results. Figure 79 shows the sketch of freely floating barge simulations and gives geometric information of the body and NWT.

4.5.1. Convergence test for time step and various node distance

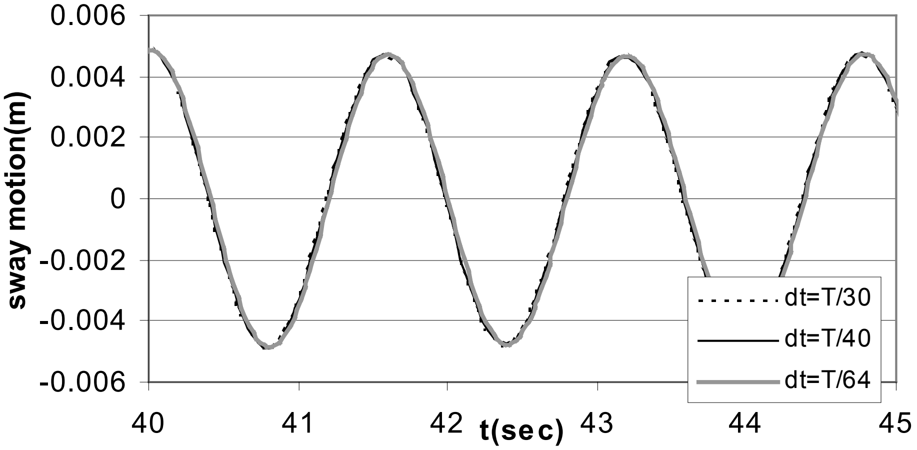

Figure 80. Comparison of different time step result for sway motion with wavelength=1.6m, T=1.5862, and H=0.07m.

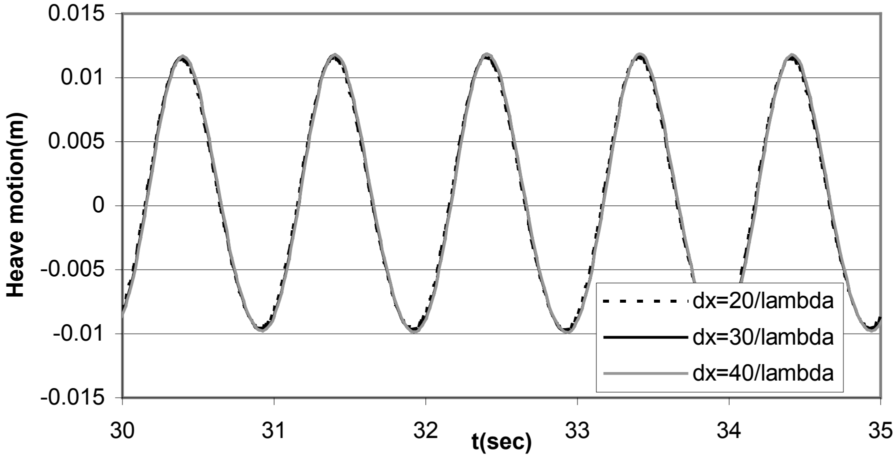

Figure 81. Comparison of various node distance results for heave motion with wavelength=1.6m, T=1.5862, H=0.07m and dt=T/40.

Figure 80 shows that present numerical results are independent of time step size smaller than dt=T/30. Runge-Kutta 4th order method used in the present study as a time marching scheme works well even in larger time step size (T/30). From this result, we usually use T/40 time step for all following numerical simulation. From Figure 81, we can see the different results with various node distances. All numerical results are close to one another even if a little difference can be observed at 20 nodes per wavelength. We can expect that convergence results can be satisfactory if we use more than 30 node per one wavelength. In this study, we usually use at least 30 nodes per one wavelength for all numerical calculations.

4.5.2. Comparison of different time marching scheme

1. Freezing geometry coefficients within one time step (roll angle)

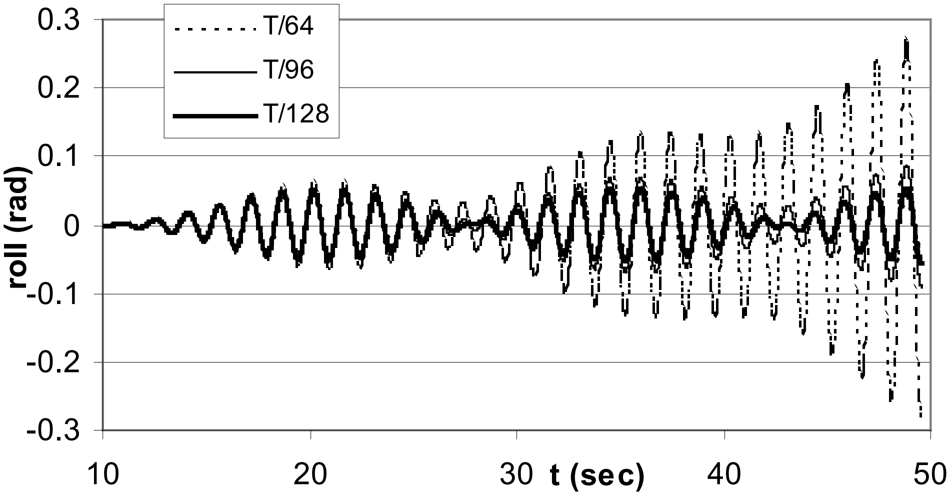

Figure 82. Comparison of roll angle for various time step results of freezing coefficients. L=1.6m, T=1.5862, and H=0.01m (See Figure 79).

2. Fully updated geometry coefficients within one time step (roll angle)

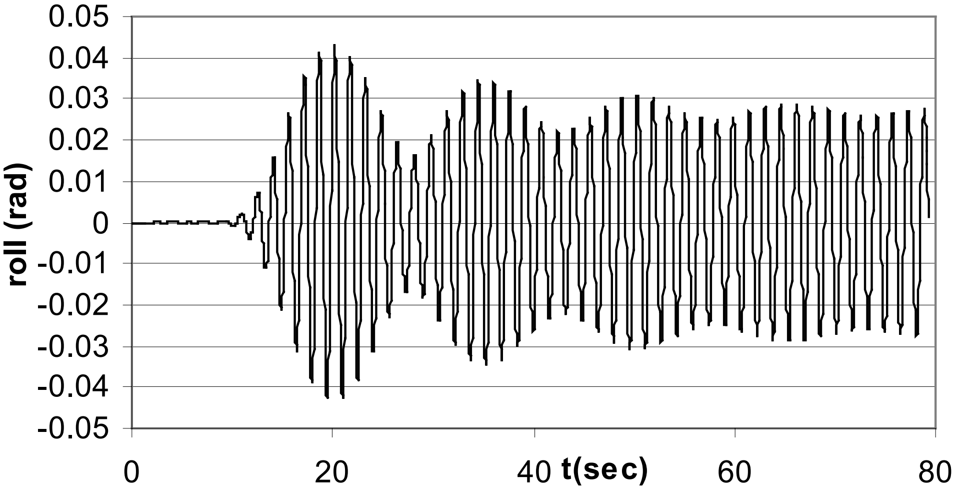

Figure 83. Roll angle results for fully updated Runge-Kutta time marching scheme, dt=T/40. Other conditions are same as Figure 79 and Figure 82.

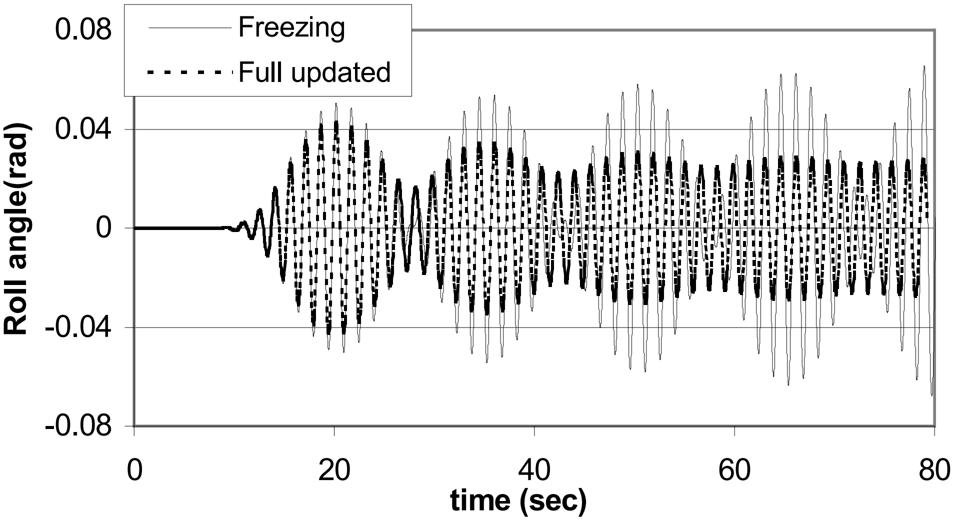

Figure 84. Comparison of different time marching scheme. Solid line=freezing coefficients (dt=T/128) and dotted line=fully updated RK scheme (T/40)

From Figure 82, the results of freezing coefficient scheme are compared with different time step. The numerical results do not reach the steady state, even if the time step is pretty small such as dt=T/128. The rate of divergence grows as time step increases. However, when we used fully updated RK scheme, which means that all geometric coefficients are updated even in the sub step of time marching scheme, the result reach steady state results (see Figure 83). In the Figure 84, two results are plotted and compared with each other.

4.5.3. Numerical results comparison

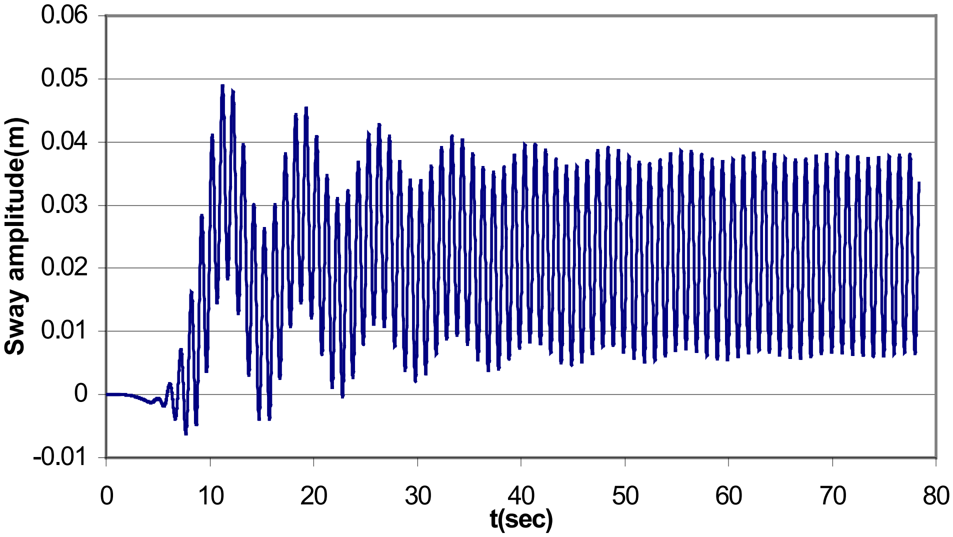

Figure 85. Time series of sway motion with xsi=0.75 (T=1.1584), H=7cm. Other conditions are same as Figure 79.

Modulation of the body motion, which is shown in Figure 85, may be created from the difference between incident wave frequency and body natural frequency. This transient modulation can also be decaying exponentially and the motion will be steady state. The period of peak modulation in Figure 85 is about 7 times of wave period, which is very close to $\frac{2\pi}{\omega - \omega_n}$, which means that the transient response at natural frequency interacts with the wave-frequency motion to generate the modulation.

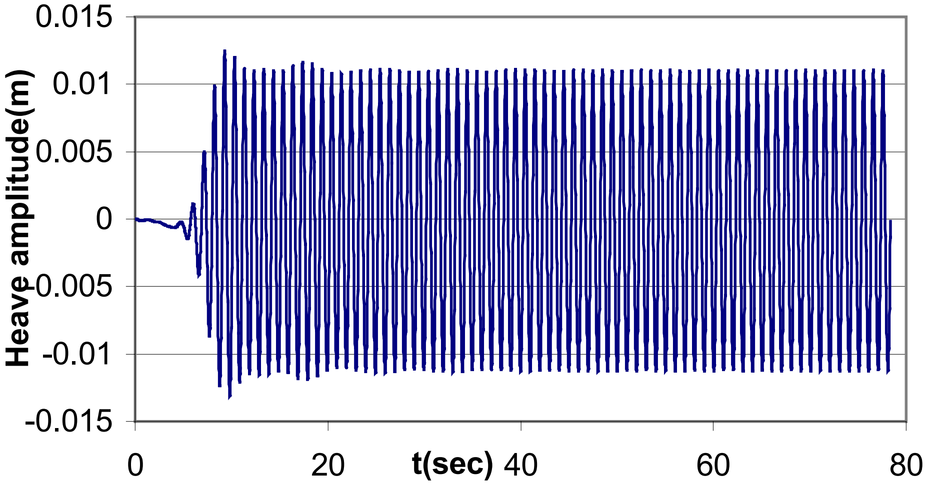

Figure 86. Time series of Heave motion with xsi=0.75 (T=1.1584), H=7cm. Other conditions are same as Figure 79.

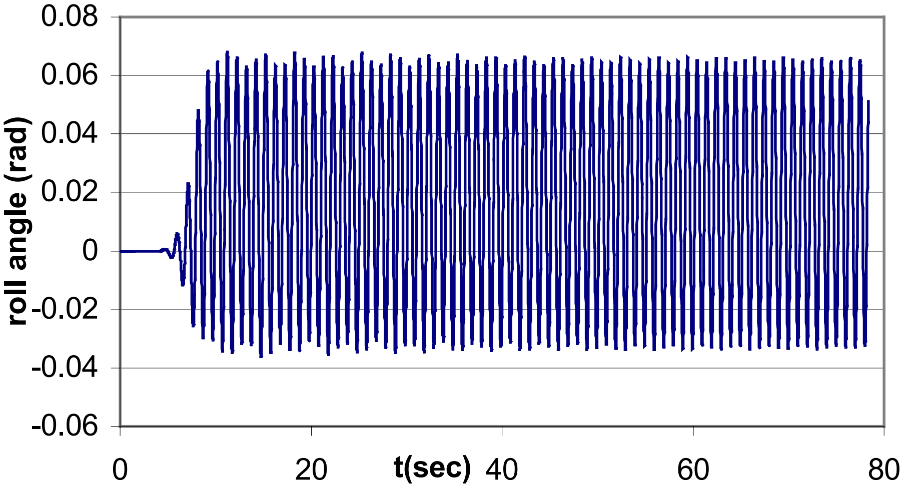

Figure 87. Time series of Roll angle with xsi=0.75 (T=1.1584), H=7cm. Other conditions are same as Figure 79.

From Figure 85 to Figure 88, all the time series results for sway, heave, roll motion and horizontal body force are shown in the steady-state. In particular, even if the time series of horizontal force are very good steady state, sway motions have the modulation. This is one of the difficulties for calculating freely floating body motions. A very little change of force calculation affects corresponding motions after twice time-integration of that force. RAO values can be obtained by using these steady state time series.

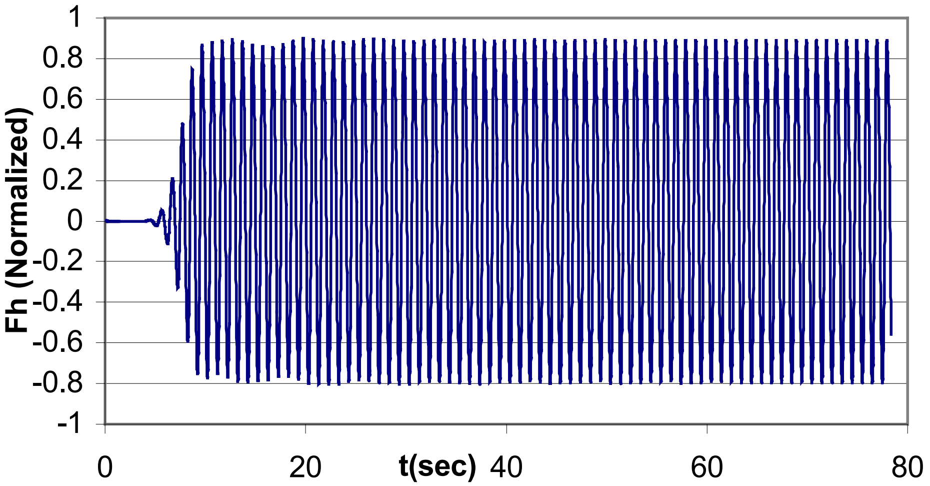

Figure 88. Time series of horizontal force normalized by rho*g*d*A. A is an initial wave amplitude (=0.035m), and xsi=0.75 (T=1.1584).

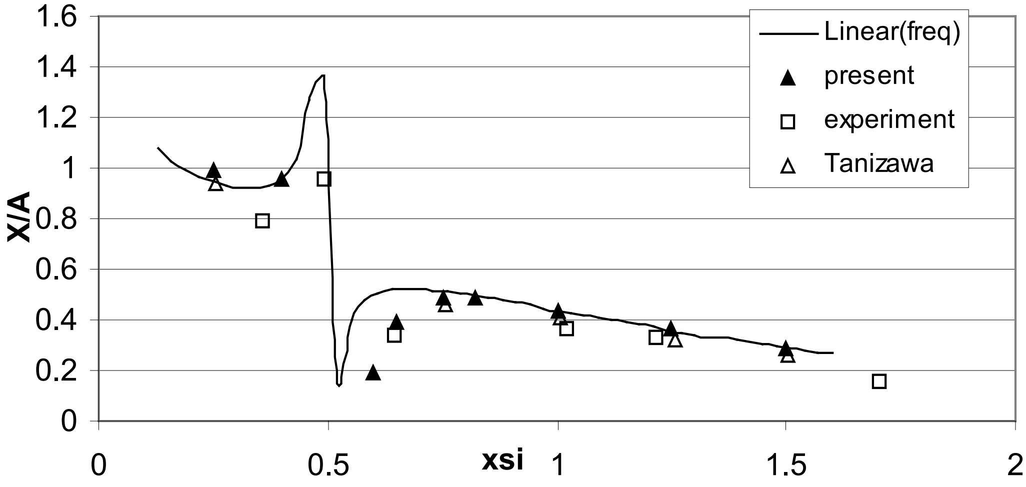

Figure 89. Comparison of sway RAO; solid line (linear frequency domain results), white rectangle (experiment, H=7cm), white triangle (Tanizawa, H=7cm), black triangle (present, H=7cm).

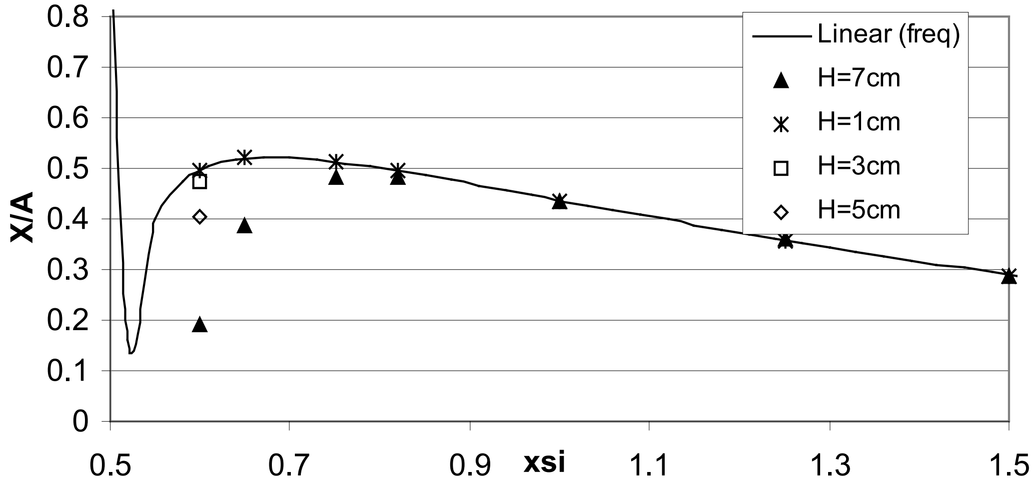

Figure 90. Comparison of numerical results (sway) with various wave heights. Other conditions are same as Figure 89.

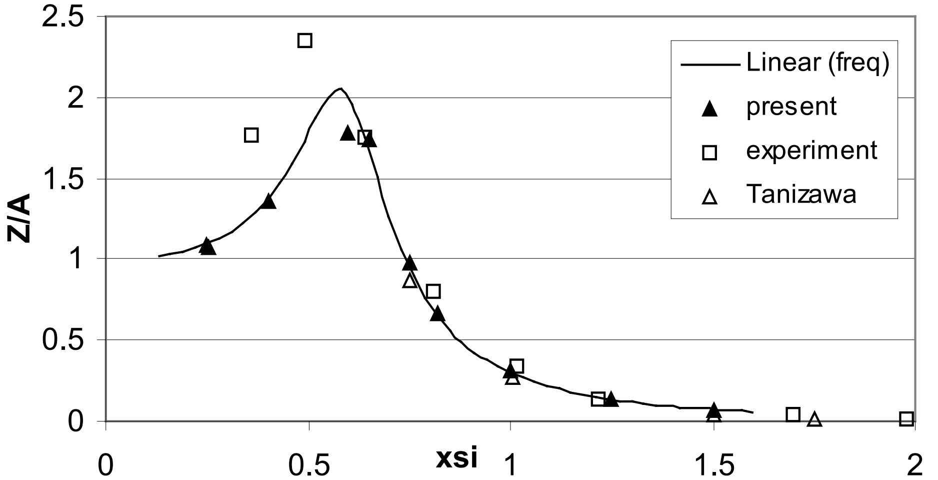

Figure 91. Comparison of Heave RAO. Other conditions are same as Figure 89.

Sway RAO comparison with experiment and other numerical results are shown in the Figure 89. Present numerical results are in good agreement with experimental results of Nojiri and Murayama (1975) and other numerical results of Tanizawa and Minami (1998). The difference of linear and fully nonlinear results is large near the resonance area (around xsi=0.6). When the frequency (xsi) is higher than 0.8 and lower than 0.4, linear results and nonlinear results agree well. From Figure 90, nonlinear results converge to the linear results near the resonance area as incident wave height decreases. Obviously, the difference of numerical calculations from linear results near the resonance area is mainly due to the input wave steepness. As input wave steepness is higher, nonlinear wave-body interactions may increase severely so that the sway motion has a big deviation from linear results.

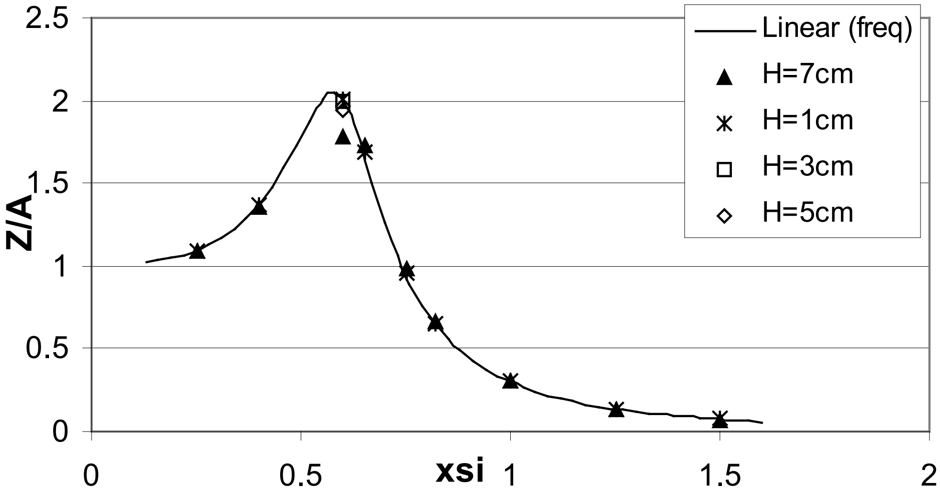

Figure 92. Comparison of heave results with various wave heights (See Figure 89).

Figure 91 and Figure 92 show the comparison of heave RAO. Experimental and numerical results are in good agreement on the entire frequency region except local deviation near the resonance area. When xsi is 0.6, fully nonlinear results are calculated and are smaller than linear frequency domain results. As the incident wave height decreases, the difference of both linear and nonlinear calculation decreases at xsi=0.6 as observed in sway case.

Roll RAO comparison is similar to sway and heave cases. A good agreement between numerical and experimental results was shown in the Figure 93, especially in the higher frequency region and a local deviation near the resonance area. In case xsi is 0.6, a big difference of roll angle between linear and nonlinear results was observed. When the incident wave height decreases (Figure 94), nonlinear results are close to the linear results, which can be seen in sway and heave cases.

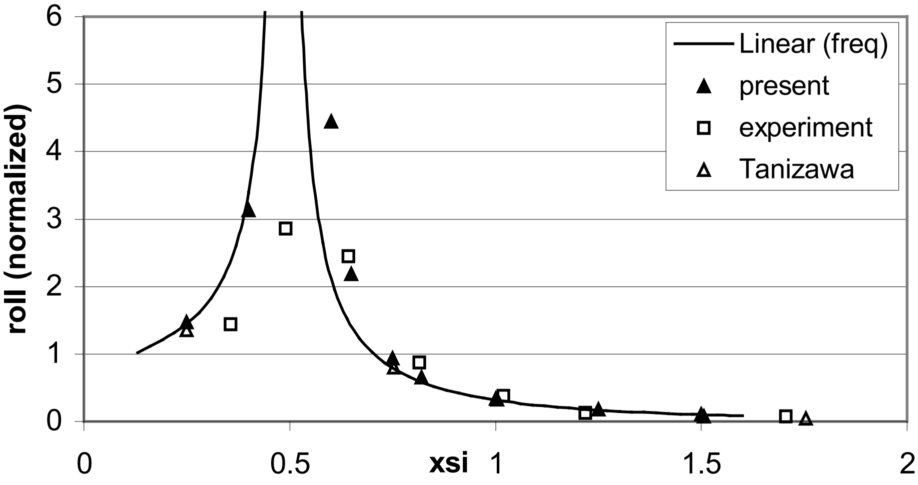

Figure 93. Comparison of roll angle (radian) RAO normalized by (w^2/g)A. Other conditions are same as Figure 89.

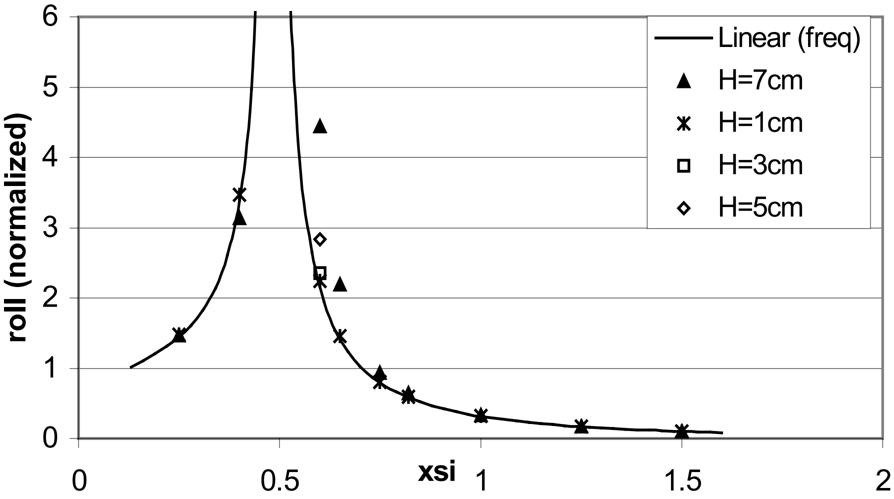

Figure 94. Comparison of roll angle with various wave heights (See Figure 89).

The comparison of drift forces with other results is shown in the Figure 95 and Figure 96. Present numerical results agree well with experimental result for values of xsi lower than 1.25 and higher than 0.75. In the high frequency area (xsi < 1.25), numerical calculations are larger than experimental results. Near the resonance area, the drift forces of present nonlinear calculations are pretty big as compared with theoretical results. As the incident wave height decreases, numerical results converge to the theoretical results (Figure 96). The deviation between numerical and experimental results in the high frequency region may be due to the effect of wave steepness. This observation is because the incident wave height is constant (H=7cm) on the entire frequency region and the wave steepness is increasing as the frequency increases. When the incident wave height is small, that is lower wave steepness, the drift force for nonlinear numerical calculation is close to the experimental results. From Figure 96, the difference between high and low wave steepness results will pronounce as wave frequency and drift force increase. At xsi=1 (L=1.57m), the difference of both wave steepness is minimum and increases toward both high and low frequency directions.

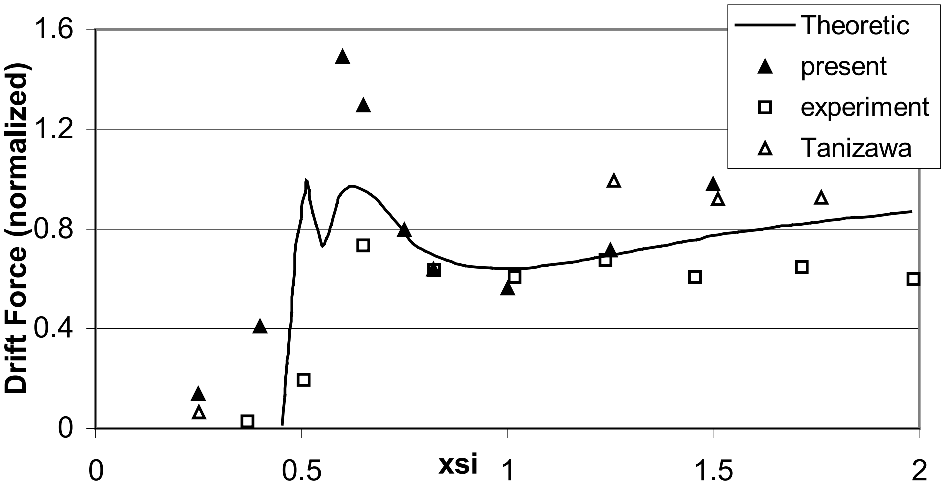

Figure 95. Comparison of drift force normalized by (1/2)rho*g*A^2. Forces are obtained by pressure integral on the body, theoretical results are 2nd order. Other conditions are same as Figure 89.

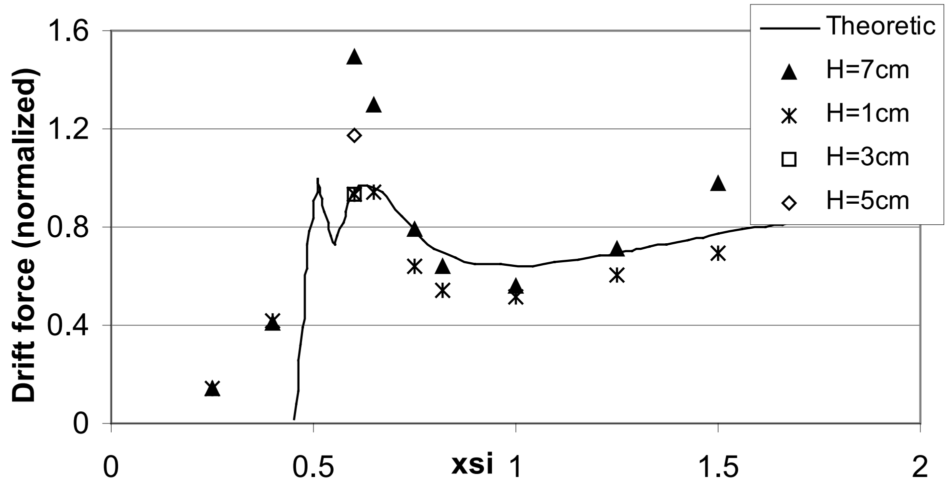

Figure 96. Comparison of drift force with various wave heights (See Figure 89).

4.5.4. Comparison of body nonlinear and fully nonlinear results

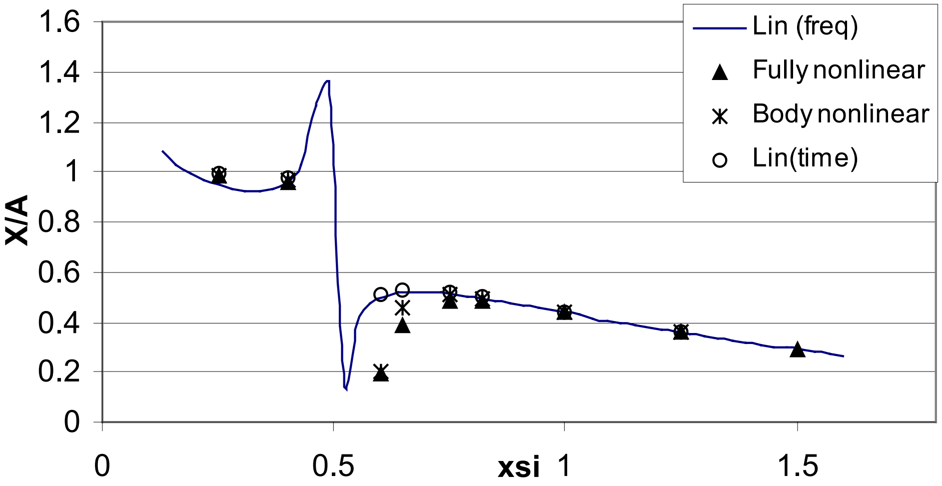

Figure 97. Comparison of sway motion for different simulation, H=0.07m. Other conditions are same as Figure 89.

Figure 97 through Figure 99 show that body nonlinear results are in between fully nonlinear results and linear results. Body nonlinear calculation can be a good alternative in the case of severe condition, which fully nonlinear method could not run in resonance area. Also, both linear time and frequency results agree well. From Figure 100, in the range of 0.25 < xsi < 0.70, drift forces of body nonlinear method are placed between fully nonlinear and linear results. As input wave frequencies increase (xsi >0.75), body nonlinear results from pressure integration have negative drift forces. Negative force area is observed when the input wave steepness is higher than 1/30. This negative drift force is growing as the input wave steepness increases.

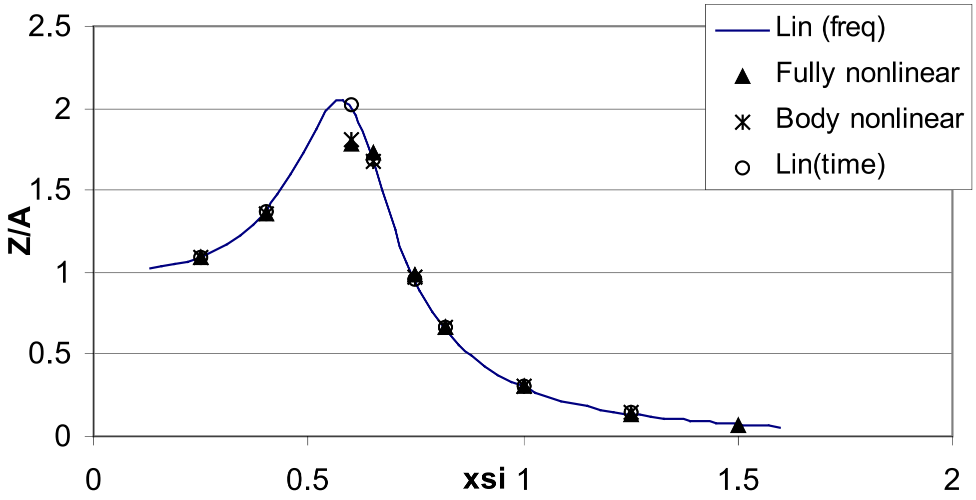

Figure 98. Comparison of heave motion for different simulation, H=0.07m. Other conditions are same as Figure 89.

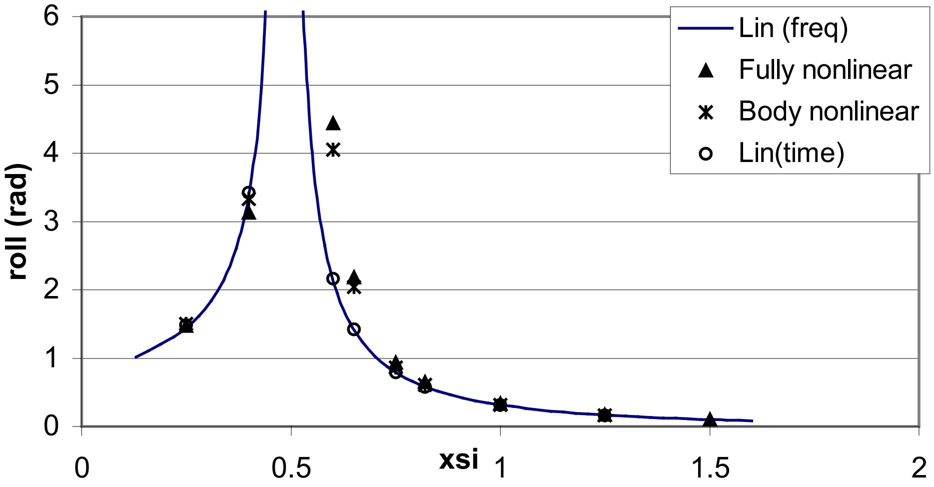

Figure 99. Comparison of roll angle for different simulation, H=0.07m, normalized by (w^2/g)A. Other conditions are same as Figure 89.

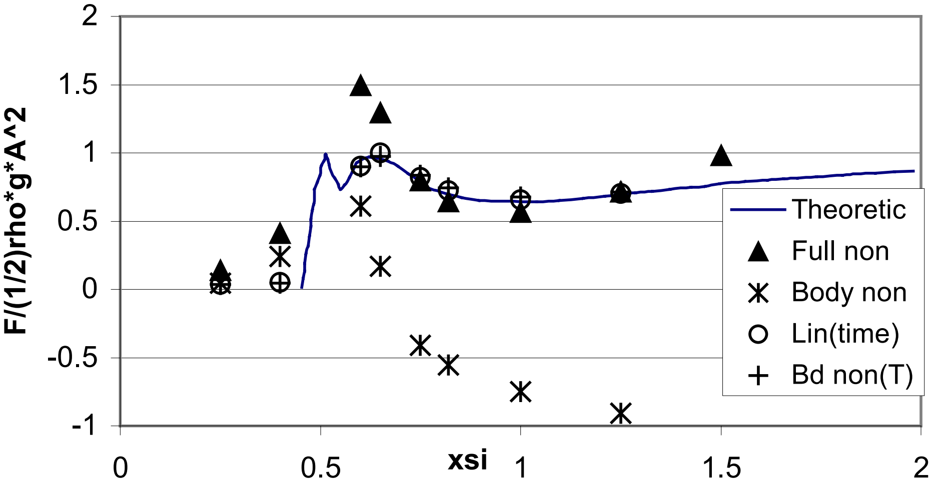

Figure 100. Comparison of drift forces for different simulation, H=0.07m, linear results and Bd non(T) results were obtained from transmitted waves (See Figure 95).

Negative drift force from pressure integral for body nonlinear simulation is mainly due to the relation of body motion and wave particle movement near the body. As the incident wave is steeper, the free surface elevation near the body has higher crest and flatter trough. When we use body nonlinear method, free surface node does not change and the node on the body follows along the body surface motion. Therefore, body force can be underestimated especially at higher wave steepness region. That's the reason drift force can be negative in that region. Judging from this example, we can conclude that the direct pressure integration method may not give reasonable mean-drift force results when the body-nonlinear approach is used.

Drift force can also be obtained by using transmitted waves (C.C. Mei, 1994). With this way, linear time domain results follow the theoretical results. Body nonlinear results from transmitted waves also follow the linear results. This is because body nonlinear simulation has been used with linear free surface boundary. Thus the overall wave fluctuation is not that different from linear elevation even if body has been moving during the simulation.

4.5.5. Investigation of barge motion near resonance area

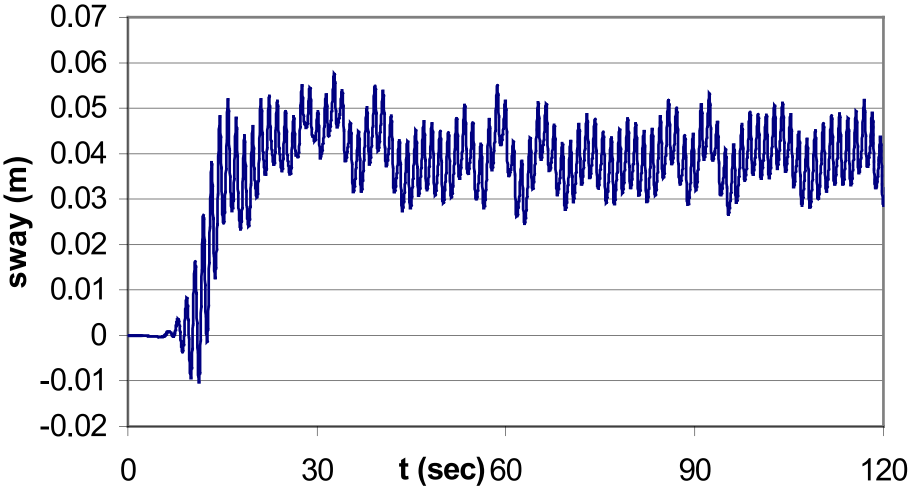

Figure 101. Time series of sway motion near the resonance area, xsi=0.6 (T=1.2951), H=7cm. Other conditions are same as Figure 79.

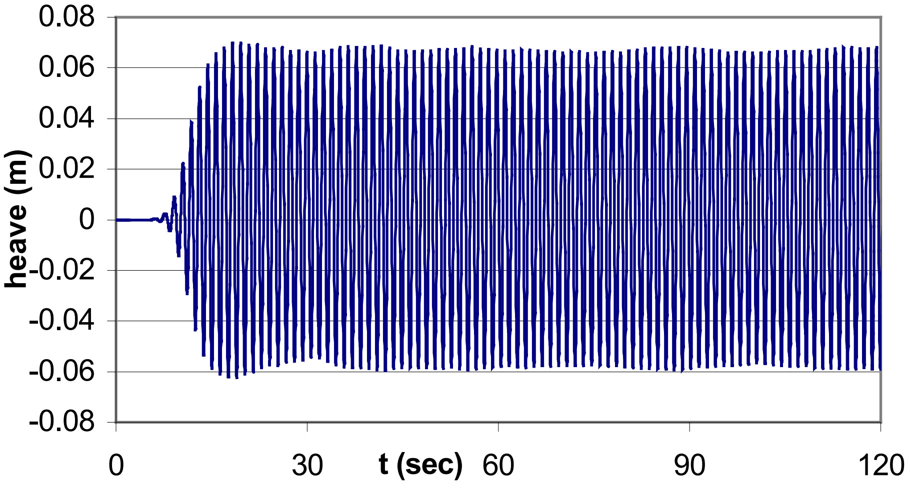

Figure 102. Time series of heave motion near the resonance area, xsi=0.6 (T=1.2951), H=7cm. Other conditions are same as Figure 79.

From Figure 101, sway motions of resonance area are quite different from other wave conditions such as xsi=0.75 etc. The results did not reach steady state, but parametric behavior did. Heave motions and roll angles are still reaching steady state after the certain range of transient time (Figure 102 and Figure 103).

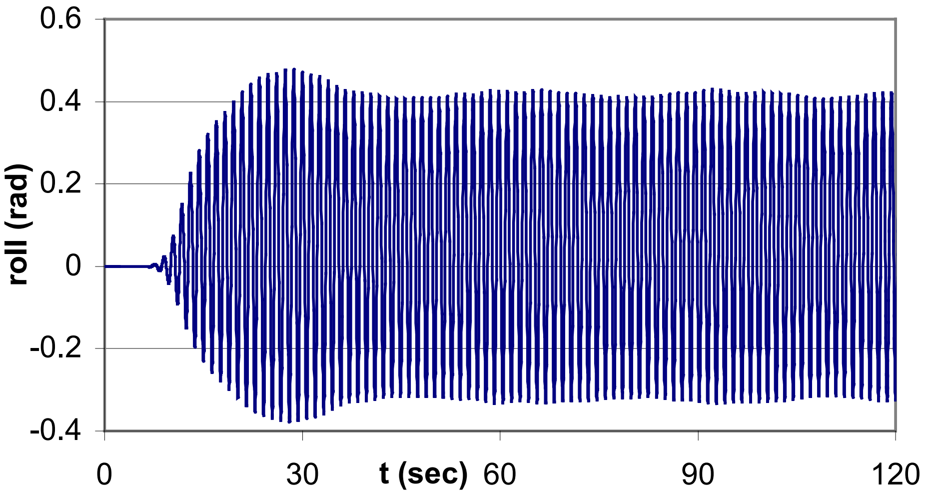

Figure 103. Time series of roll angle near the resonance area, xsi=0.6 (T=1.2951), H=7cm. Other conditions are same as Figure 79.

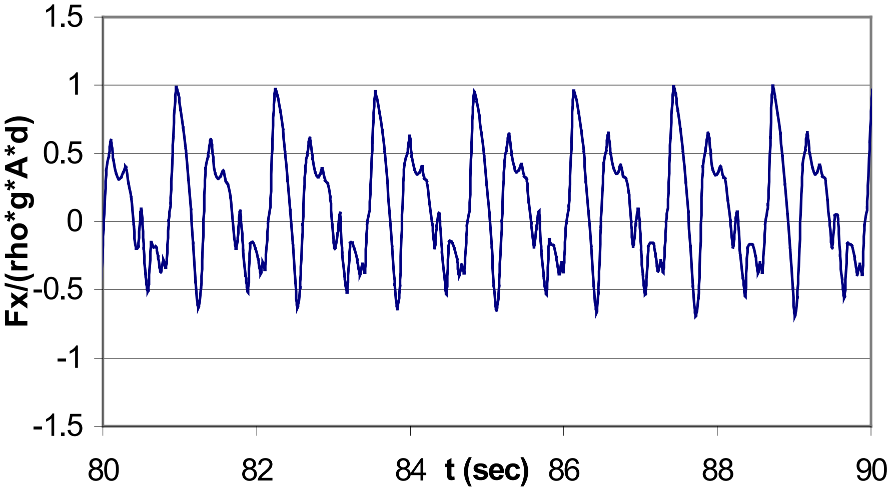

Figure 104. Time series of horizontal force on the barge with xsi=0.6 (T=1.2951), H=7cm. Other conditions are same as Figure 79.

Time series of horizontal, vertical forces, and roll moments are shown in Figure 104, through Figure 106. All results are shown to be in steady state during the simulation. In particular, the strength of nonlinearity for horizontal force is much stronger than that of vertical force and roll moment, even if all forces and moment contain nonlinear effect. Due to the strong nonlinearity of the horizontal force, sway motions did not show steady state, but parametric behaviors restrained in certain range of motion amplitude.

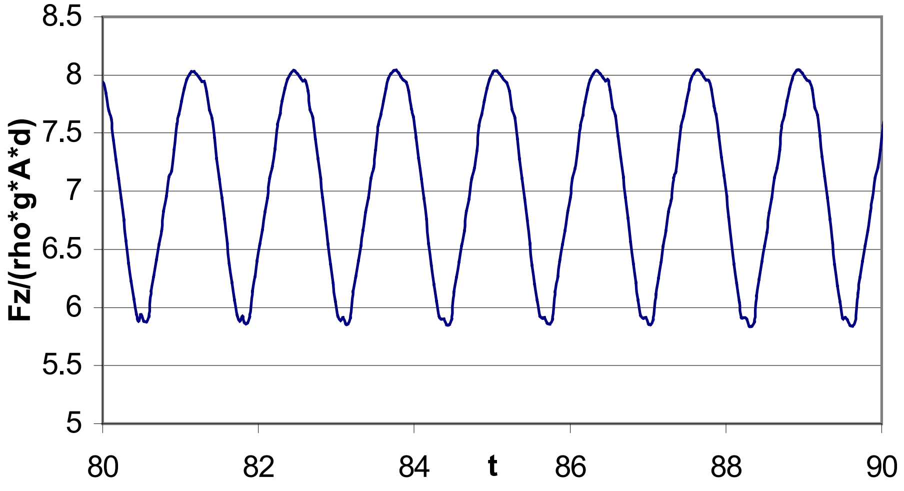

Figure 105. Time series of vertical force on the barge. Other conditions are same as Figure 79 and Figure 104.

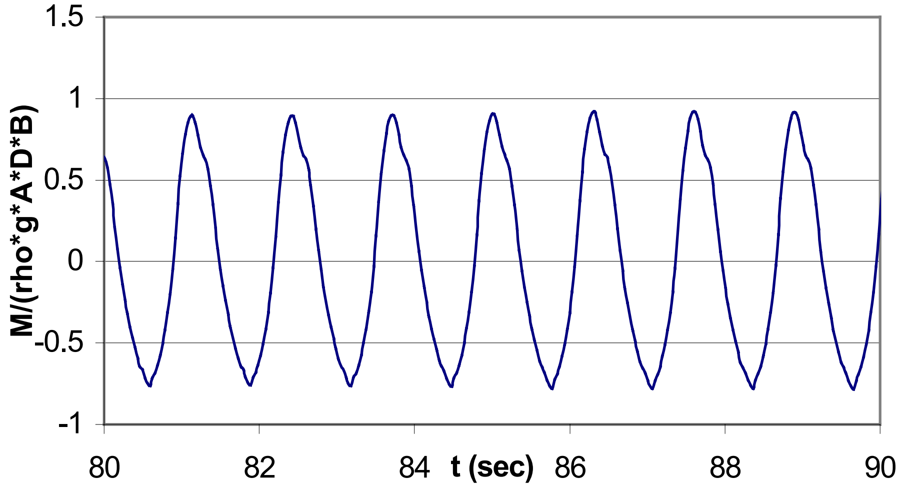

Figure 106. Time series of moment on the barge. Other conditions are same as Figure 79 and Figure 104.

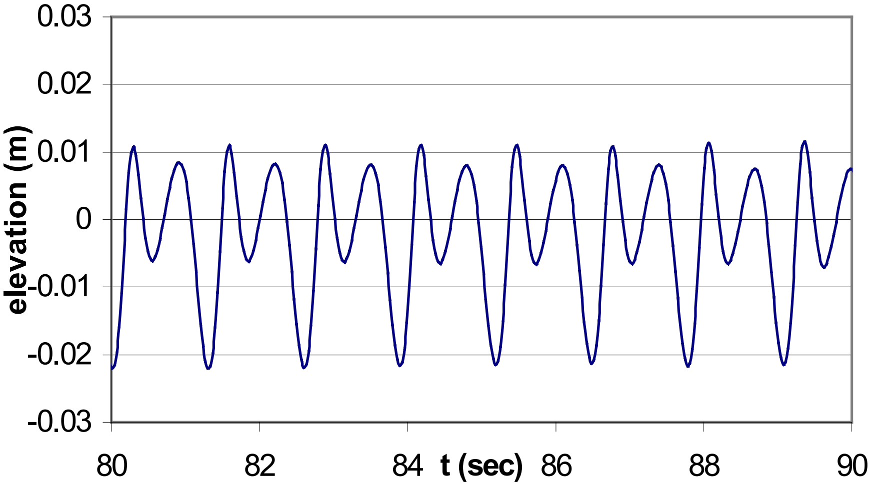

Figure 107. Time series of wave elevation at location 0.5 wavelength in front of the barge (weather side) with xsi=0.6 (T=1.2951), H=7cm.

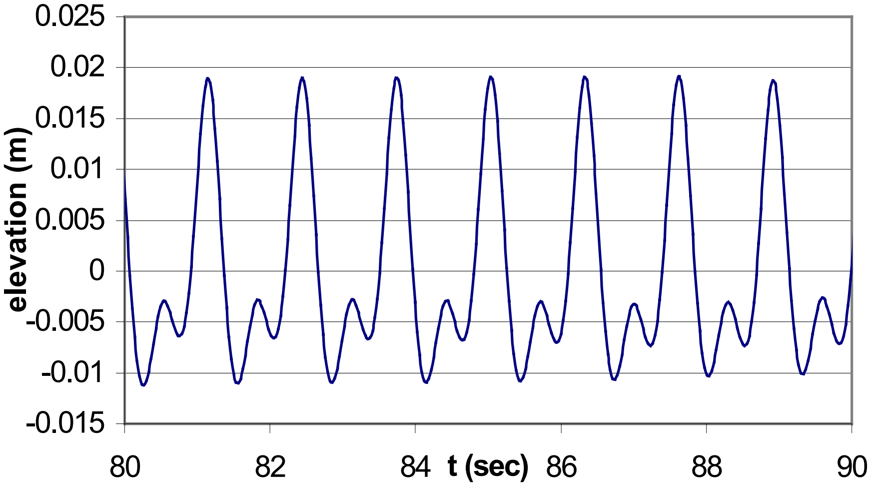

Figure 108. Time series of wave elevation at location 0.5 wavelength behind the barge (lee side).

The comparison of surface elevations for weather and lee side of the body is shown in Figure 107 and Figure 108. Surface elevations of the both sides have strong nonlinear waves. The elevation of weather side contained bigger higher-order waves than that of lee side.

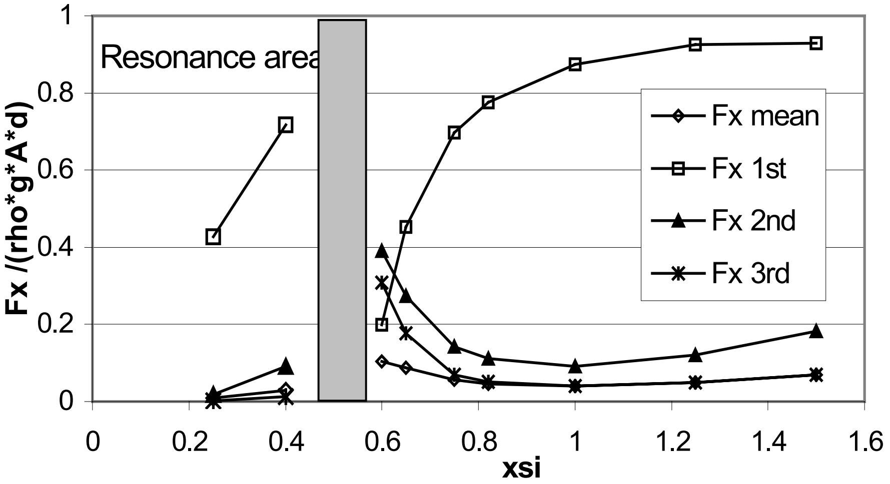

Figure 109. Comparison of horizontal force components, H=0.07m (See Figure 79).

Figure 109 shows the comparison of horizontal force components against various wave conditions. Near the resonance area (xsi=0.6), 2nd and 3rd order forces are greatly increasing and are bigger than 1st order force and mean force. As incident wavelength shortens (xsi increases), 1st harmonic force is increasing, while other components are decreasing until xsi is around 1 (wavelength=1.57m, T=1.0032). When the incident wavelength is shorter than 1.57m (xsi > 1) with same wave height (H=0.07), i.e. wave steepness increases, 1st harmonic force is reaching to certain values and other higher components are gradually increasing. Due to this phenomenon, drift force may be increasing when wavelength is shorter than 1.57m (H / λ=1/22) as we shown in Figure 95.

From Figure 110 and Figure 111, the maximum vertical force and roll moment components are observed near the resonance area. In both cases, higher order components do not exceed 1st order components as seen in horizontal force. However, 2nd order vertical force is gradually increasing and eventually becomes greater than 1st order force after xsi=1.5 (T=0.8191, H/L=1/15). All components of moment are gradually decreasing as wave frequency increases. Mean values in both vertical force and roll moment are always close to zero in the entire frequency range.

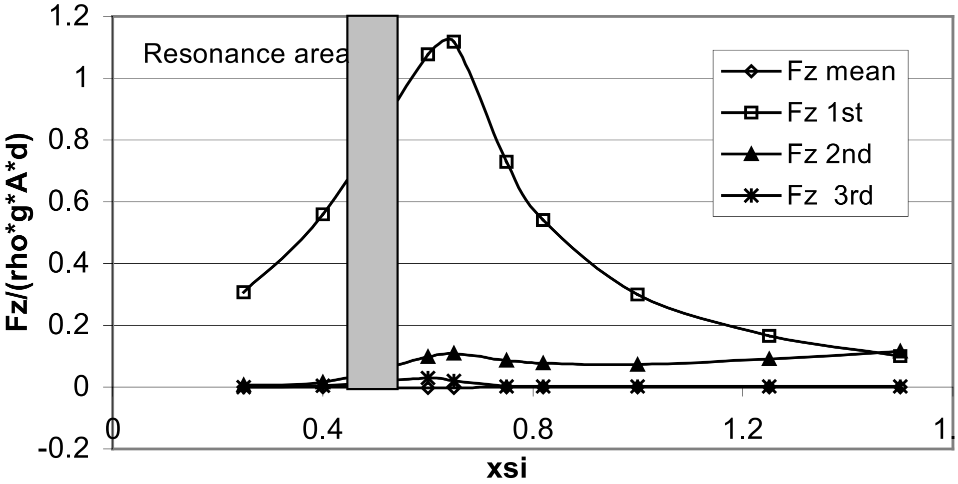

Figure 110. Comparison of vertical force components, H=0.07m (See Figure 79).

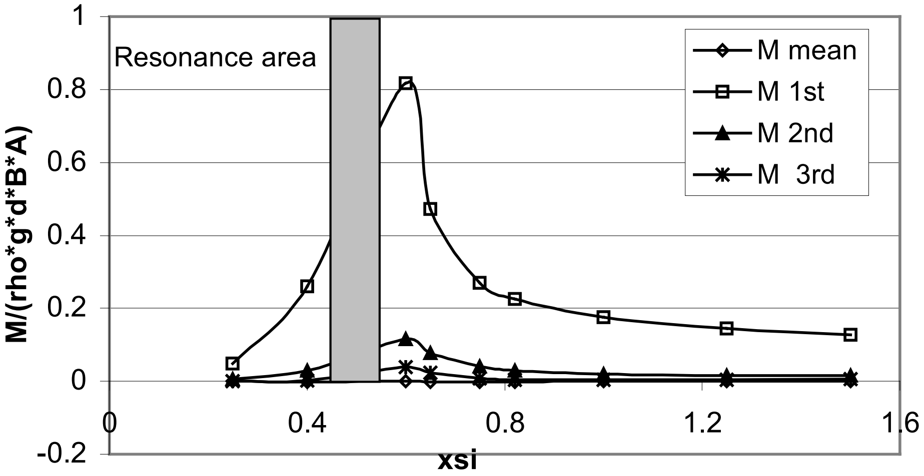

Figure 111. Comparison of moment components, H=0.07m (See Figure 79).

4.5.6. Comparison of indirect method

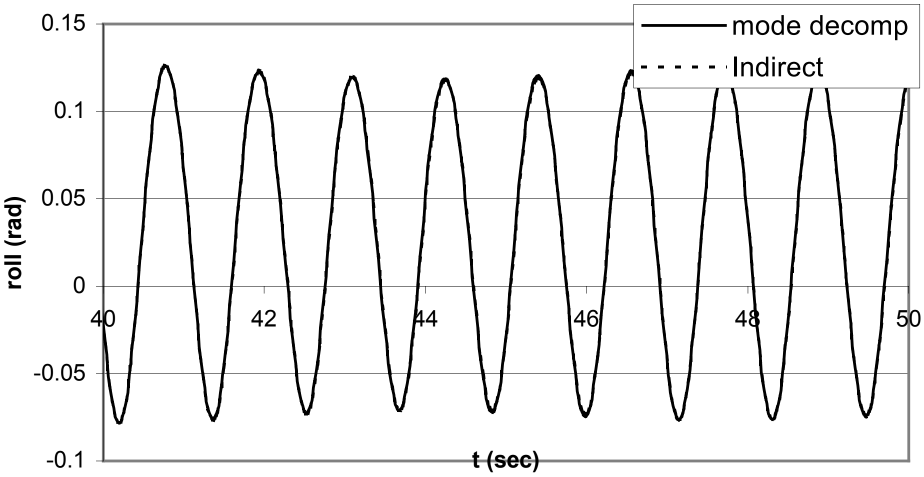

Figure 112. Roll angle comparison with mode decomposition and indirect method. xsi=0.75 (T=1.1584), H=7cm. Other conditions are same as Figure 79.

Figure 112 shows that there is no difference between mode decomposition method and indirect method. As mentioned in Chapter III, the indirect method is mathematically same as the mode decomposition method. Through the comparison of two different methods from Figure 112, the formulations and applications of mode decomposition method to analyze floating body simulations are proved.

4.6. Long wave generation due to land sliding

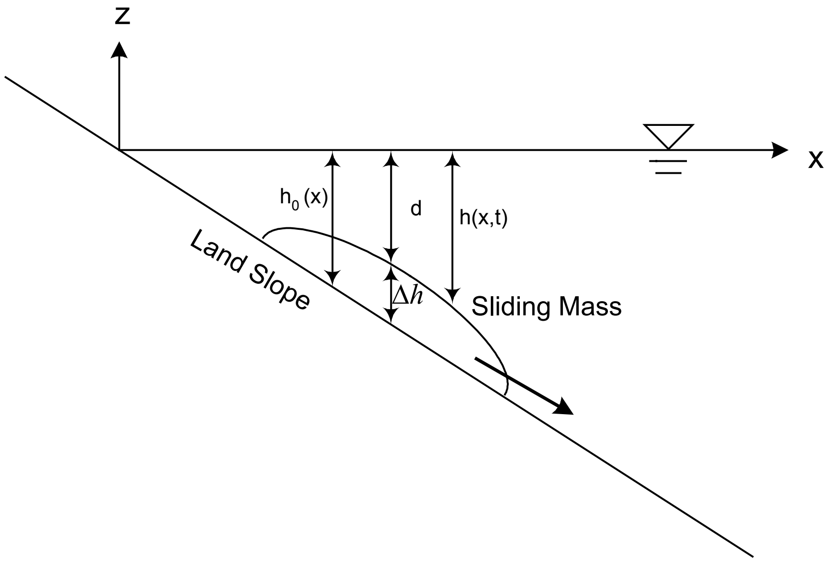

Figure 113. Sketch of land sliding problem (sliding-mass shape can be arbitrary).

Land-sliding motion simulation is one of the interesting applications, which NWT can do. Sliding mass is forced to move along the bottom slope. This case is similar to forced motion simulation such as wedge type wave maker. The shape of sliding mass is described by some mathematical formulation.

All of the land-sliding motion coefficients used in this study are identical to those employed by Grilli & Watts (1999). The time-history of the seafloor is described by

$$h(x,t) = h_0(x) - \frac{1}{4}\Delta h^* \left[1 + \tanh\left(\frac{x - x_i(t)}{S}\right)\right]\left[1 - \tanh\left(\frac{x - x_e(t)}{S}\right)\right] \tag{68}$$

where, Δh^* is the initial input for maximum vertical height of the sliding mass, x_i is the location of the tanh function inflection point of the left side of the mass, x_e is the location of the inflection point on the right side, and S is a shape function, which can control the steepness of the slide mass. Both side boundaries and steepness factor are given by

$$x_i(t) = x_c(t) - \frac{1}{2} b\cos(\theta), \quad x_e(t) = x_c(t) + \frac{1}{2} b\cos(\theta), \quad S = \frac{0.5}{\cos(\theta)} \tag{69}$$

where, x_c is the horizontal location of the center point of the slide mass, and is determined by slide mass motion equation. The angle of the bottom slope is given by θ (degree). With a specified depth above the initial center point of the slide mass, $d_0 = d(t=0)$, the initial horizontal center point, $x_c(t=0)$ can be found. In this study, the time series of x_c (t) is obtained by simple equation from Grilli & Watts (1999). The length along the slope between x_i and x_e is defined as b.

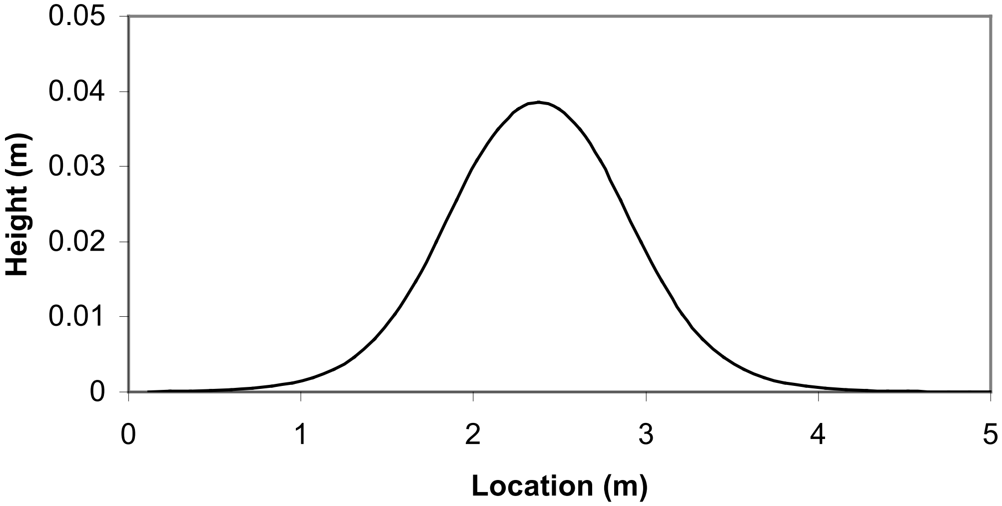

Figure 114. Initial location of sliding mass with respect to horizontal view. $\theta = 6^0$, $d_0^* = 0.2$, $\Delta h^* = 0.05$, **and b=1 , where** d_0^* **is initial input for** d_0; $\Delta h = 0.0386$, $d_0 = 0.2114$.

The motion of slide mass is given by approximate analytic solution (Watts, 1997 and Grilli & Watts, 1999).

$$s(t) = s_0 \ln\left(\cosh \frac{t}{t_0}\right) \tag{70}$$

where, s is an approximate mass center location along the slope, i.e. s=0 at t=0. The velocity and acceleration of mass center at times t > 0 follow from the derivatives of equation (70).

$$\frac{ds(t)}{dt} = u_t \tanh\frac{t}{t_0}, \qquad \frac{d^2s(t)}{dt^2} = a_0\left(\cosh\frac{t}{t_0}\right)^{-2} \tag{71}$$

where, the characteristic distance of sliding mass acceleration $s_0 \equiv u_t^2 / a_0$, and the duration of sliding mass acceleration $t_0 \equiv u_t / a_0$ are described by simple initial acceleration a_0 and terminal velocity u_t. The initial acceleration and terminal velocity of sliding mass are given by

$$a_0 = g\frac{\gamma - 1}{\gamma + C_m}\sin\theta \tag{72}$$

$$u_t = \sqrt{gb}\sqrt{\frac{\pi(\gamma - 1)}{2C_d}\sin\theta} \tag{73}$$

where, $\gamma = \rho_l / \rho_0$, C_m=1.0 and C_d=1.0 are an approximate added mass coefficient and drag coefficient. The added mass and drag coefficients are those of a circular cylinder. This is because Watts (1999) found that the motion of sliding mass with specific density $\gamma \approx 2$ is not sensitive to precise added mass and drag coefficients.

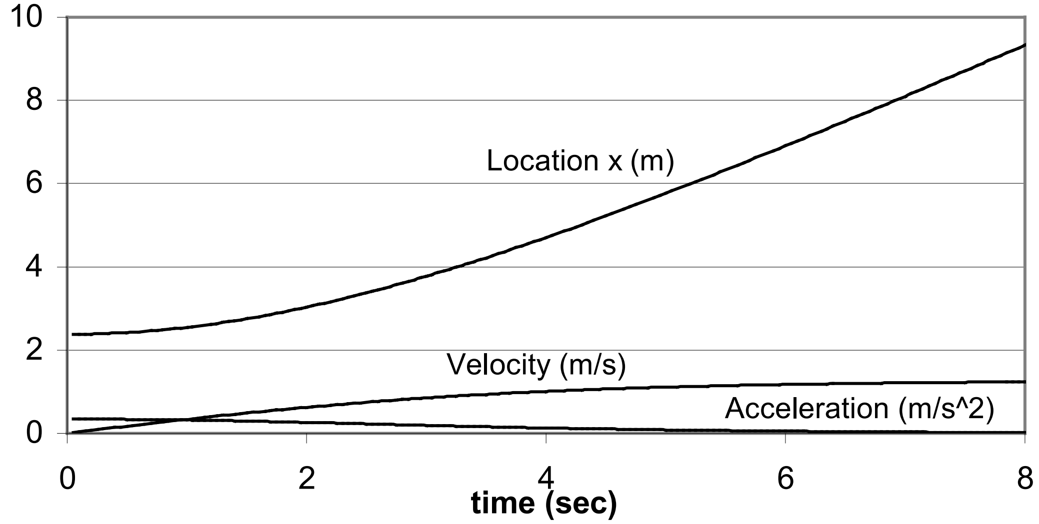

Figure 115. Location, velocity, and acceleration of sliding mass center. Same condition as Figure 114.

Figure 115 shows sliding mass location, velocity, and acceleration calculated by equations (70) and (71). These motions are similar to the characteristics of real land sliding for some cases.

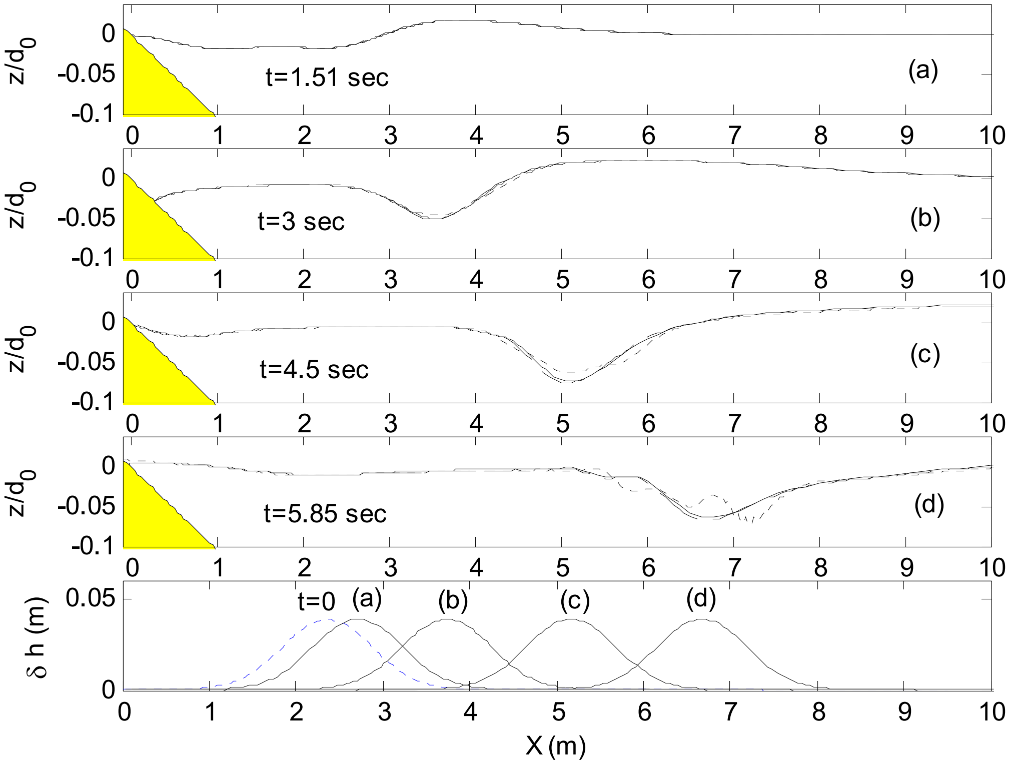

Figure 116. Comparison of free surface snapshots at $\theta = 6^0$, $d_0^* = 0.2$, $\Delta h^* = 0.05$, and b=1; present (dashed), BIEM (solid), and depth integrated (dotted).

In Figure 116, the comparison of free surface snapshots at several time steps is shown. Present results are in good agreement with BIEM results (Lynett & Liu, 2002). As sliding mass moves along the sea slope, the generated waves propagate toward deep water. The difference of free surface profile is observed at t=5.85 between present results and depth-integrated solutions (Lynett & Liu, 2002). The depth-integrated results are only good for shallow water region. This difference can increase when the wave propagates to deep water. Fifth graph of Figure 116 clearly shows that the location of sliding mass center matches with generated wave trough at each time shots. It may be found that the sliding mass pushes the water mass so that the pressure difference generates propagating waves.

Wave run-up and run-down are shown in Figure 117. On the coastline, water mass runs down initially and runs up later, as sliding mass moves along the slope.

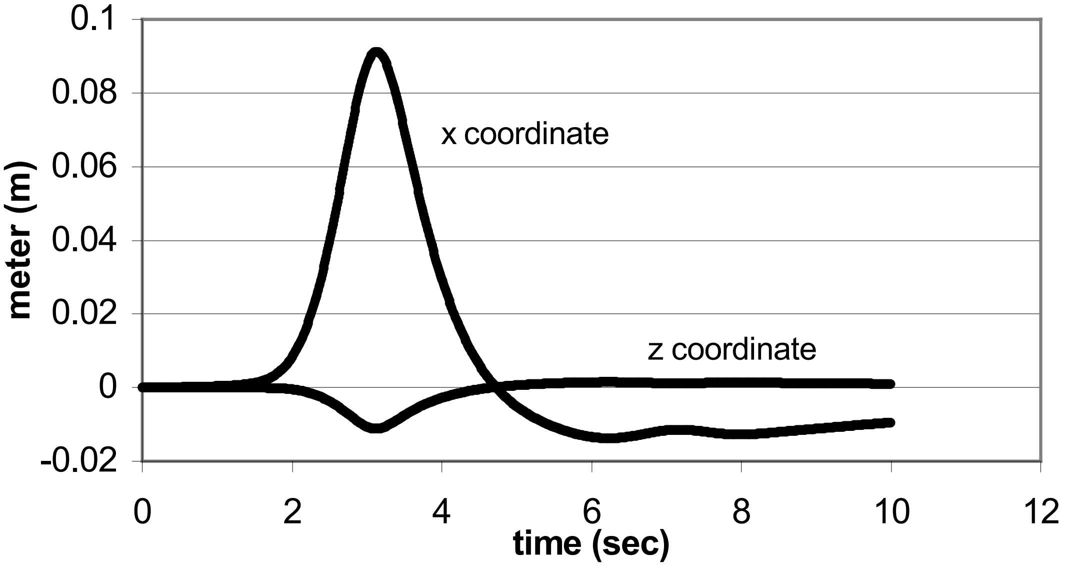

Figure 117. Wave run-up and run-down at the end of free surface due to land sliding. Same condition as Figure 116.

4.7. Sub-ariel land sliding

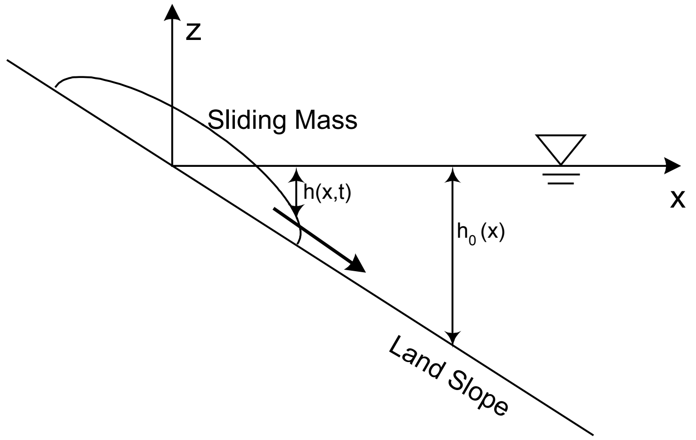

Figure 118. Sketch of sub-ariel land sliding (sliding-mass shape can be arbitrary).

After confirmation of free surface elevation for submerged land sliding, sub-ariel land sliding problem can be considered (see Figure 118). This situation may represent a part of iceberg sliding on the sea slope. From submerged land sliding, we found that sliding mass pushes the water mass thus long wave is generated. Obvious, sub-ariel land sliding has more impact on the water surface than submerged case. With a same condition as fully submerged case, the location of sliding mass center is set to origin initially.

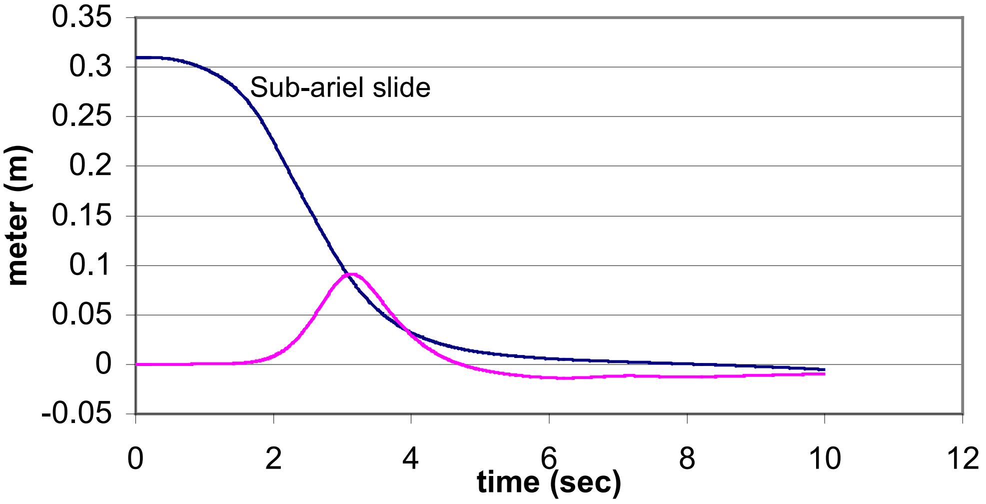

Figure 119. Comparison of horizontal location of waterfront due to sub-ariel and submerged land sliding (See Figure 116 and Figure 118).

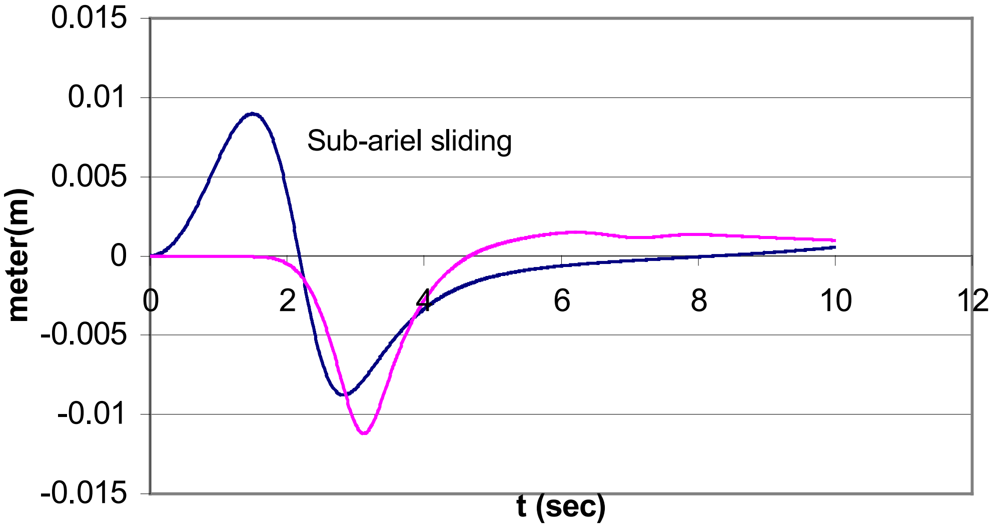

Figure 120. Comparison of vertical location of waterfront (See Figure 119).

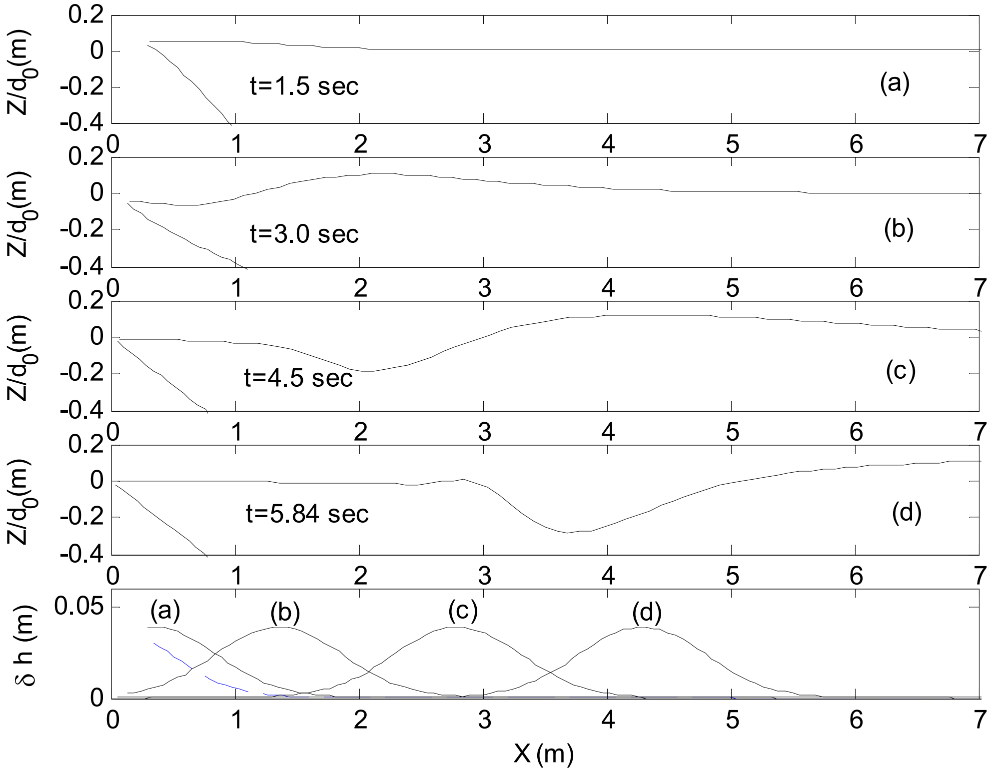

Figure 121. Comparison of free surface snapshots for sub-ariel land sliding.

In Figure 119 and

Figure 120, the magnitude of surface fluctuation at the coastline is much larger than fully submerged land sliding, especially within 5 seconds. Due to the shape of sliding mass on the free surface initially, horizontal location of wave front is not zero but is the thickness of sliding mass. Vertical wave front is up and down as the sliding mass moves into the water. After 5 seconds later, the case of sub-ariel sliding has a small free surface fluctuation compared to fully submerged sliding case. From Figure 121, the magnitude of free surface elevation on the entire area is about 4 times bigger than fully submerged case.

From these figures, it can be seen that sub-ariel land sliding has a big free surface fluctuation near the coastline initially because of shape of sliding mass. This sliding mass pushes water mass near free surface area efficiently so that the magnitude of free surface fluctuation is bigger. As water mass is forced to move by sliding mass, a large propagating wave is generated toward offshore area. As the time increases enough to generate the backward waves induced by main waves of free surface, i.e. about 6 seconds, the surface elevation at the coastline starts to increase. The elevation may be larger than that of fully submerged sliding case after 10 seconds.

4.8. Current interactions for floating body motions

Accurate predictions of wave loads and responses of floating structures in combination with wave and current are of practical importance in the design and operations in the natural environment. In many situations, the current velocity or the speed of drifting is small and the effects of flow separation are usually unimportant so that the problem can be considered within the framework of potential theory.

In this study, a steady uniform current is employed to the freely floating body problem. The body size (B=0.5m, d=0.25m) and other computational domain are the same as floating body case (Chapter 4.7). Current speed is 0.1m/sec and input wave height is 0.07m. Wave frequency is xsi=0.25 (T=2.0064) and wavelength is 6.28m. The incident wave velocity is around 3.13m/sec so that the current speed is about 3% of wave celerity.

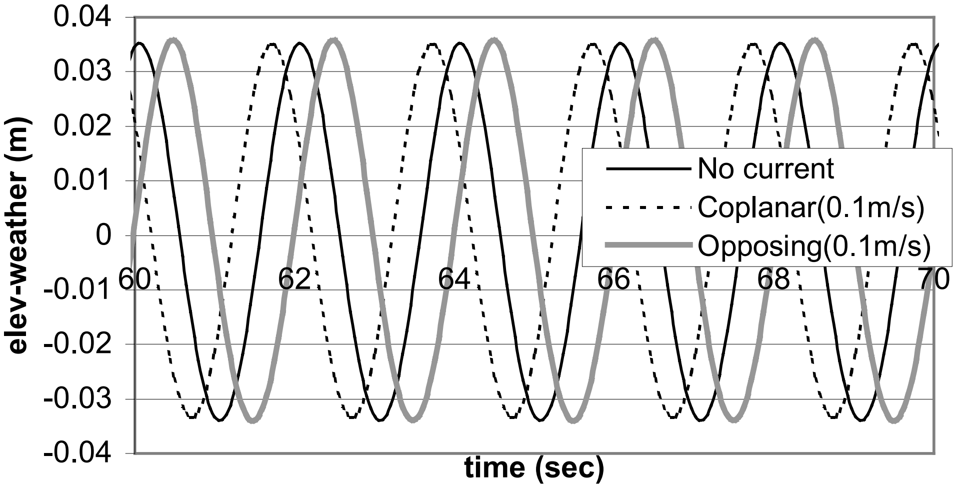

Figure 122. Comparison of elevation at location 1 wavelength in front of the body (weather side).

Figure 122 shows that comparison of wave elevation at location 1 wavelength in front of the body, i.e. weather side. Coplanar case has a lower wave crest due to the current effect, while opposing case has a higher wave crest. Figure 123 also shows the similar features that the crest of coplanar case is lower than that of opposing current case. The crest of no-current case is placed between coplanar and opposing cases.

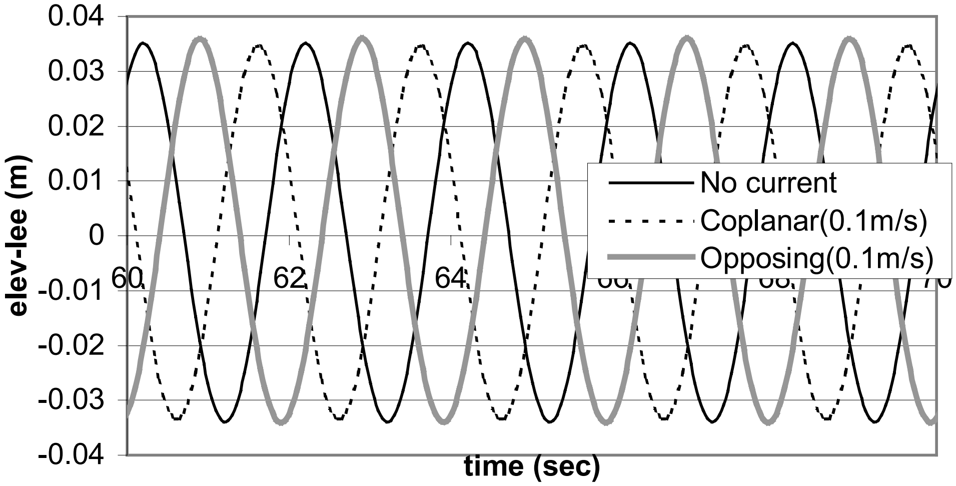

Figure 123. Comparison of elevation at location 1 wavelength behind the body (lee side).

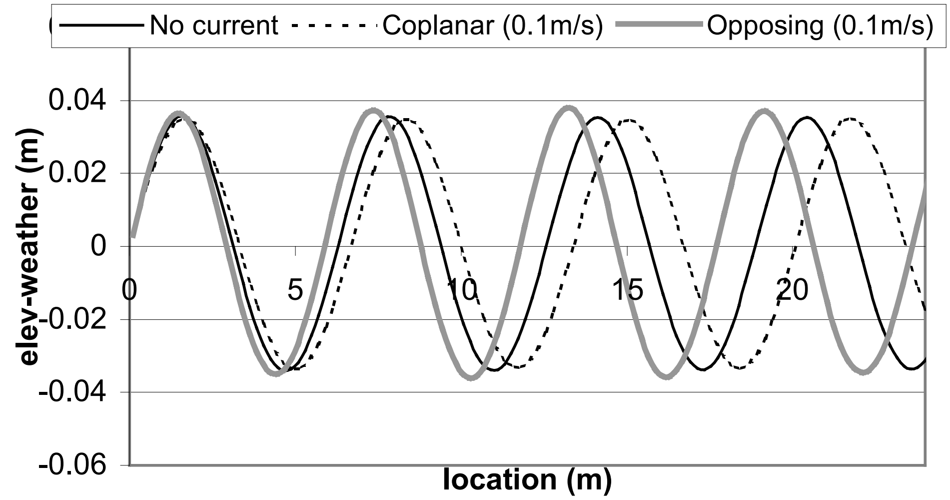

Figure 124. Comparison of wave snapshot at weather side.

From Figure 124 and Figure 125, we can clearly see that coplanar current case has longer wavelength, while opposing case has shorter wavelength. When the incident wave propagates toward the floating body with the current term employed on the entire free surface boundary, the difference of wave elongation becomes large as the location is farther. This phenomenon can be explained by constant current term employed on the free surface. The Current term is constant regardless of the location of free surface so that the propagating waves are globally affected by the current term.

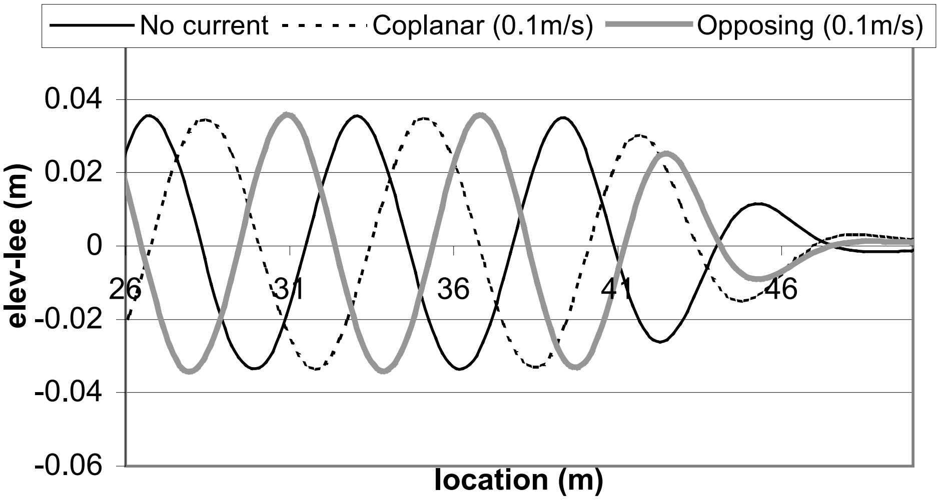

Figure 125. Comparison of wave snapshot at lee side.

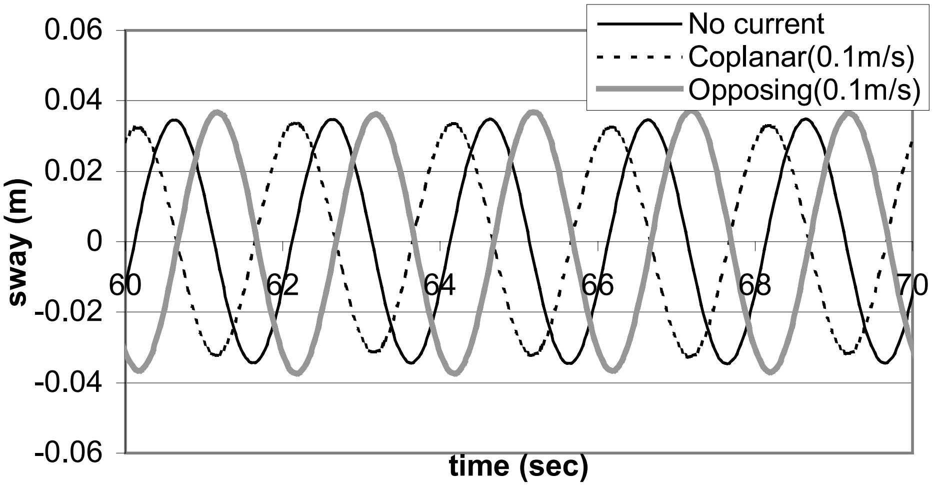

Figure 126. Comparison of sway motion with current cases.

The comparison of floating barge motions induced by wave and current is shown in Figure 126 through Figure 128. For all motions, the opposing-current case has the biggest motion, no-current case has comparatively less motion and coplanar case has the smallest motion. The change of wave amplitude and length as well as the shift of incident wave frequency by Doppler effect may explain these phenomena. With the same incident waves, coplanar current can increase wavelength, while the opposite is true for the opposing case. From the RAO graph (Figure 89 through Figure 93), as wavelength decreases, the response of all motions increases near xsi=0.25. From Figure 93, we can expect that roll response can increase sharply even with small change of wave frequency near xsi=0.25. Since the wave steepness considered is small H/L=0.011, the motion signal does not exhibit highly nonlinear features.

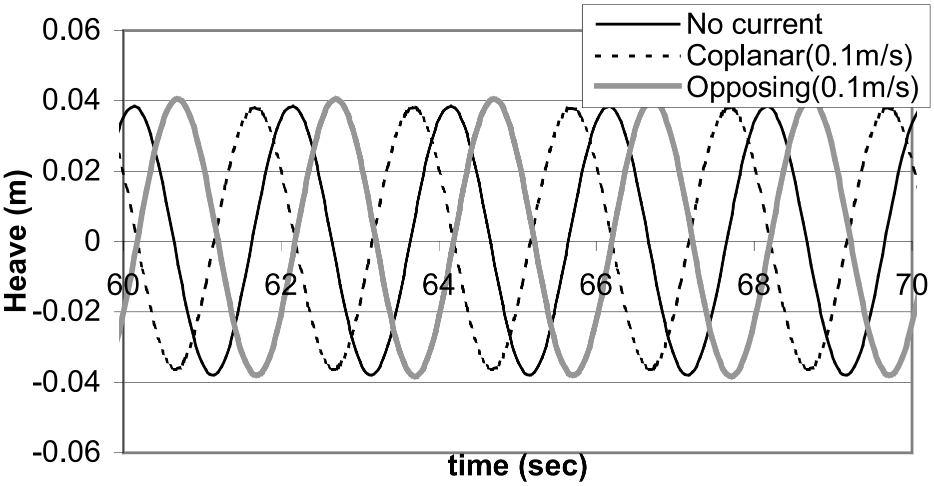

Figure 127. Comparison of heave motion with current cases.

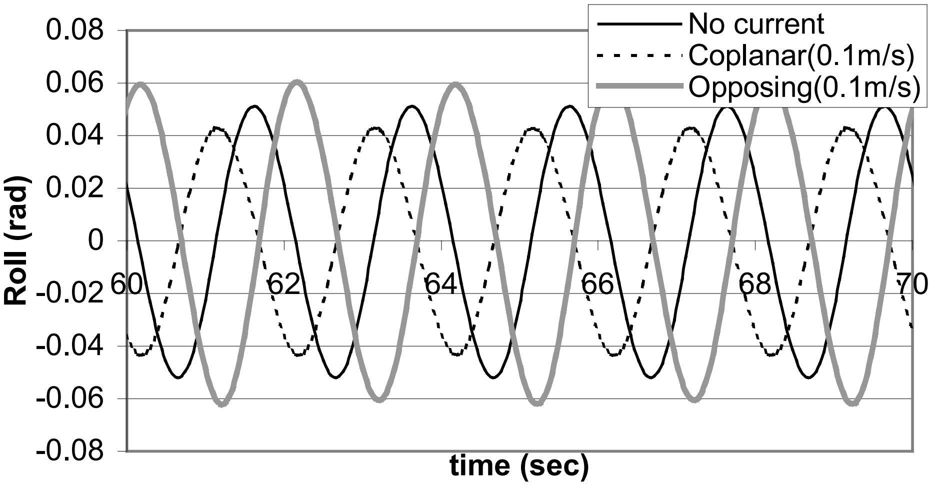

Figure 128. Comparison of roll angle (radian) with current cases.

The comparison of run up at the floating body is shown in Figure 129 and Figure 130. At the weather side, coplanar case has a bigger run up as compared with opposing case, as shown in Figure 129. From Figure 130, the run up value of opposing current at the lee side is larger than that of coplanar current. The current term can be applied to the entire free surface even near the body surface so that the current can affect the closest node near the body. Water particles riding on the coplanar current can ascend on the body surface when the body rotates at the weather side, while water particles will descend at the lee side. The opposing current will make the water particle not to climb on the body surface. Therefore, lower run up with opposing current can be observed at weather side, while higher value can be seen at lee side.

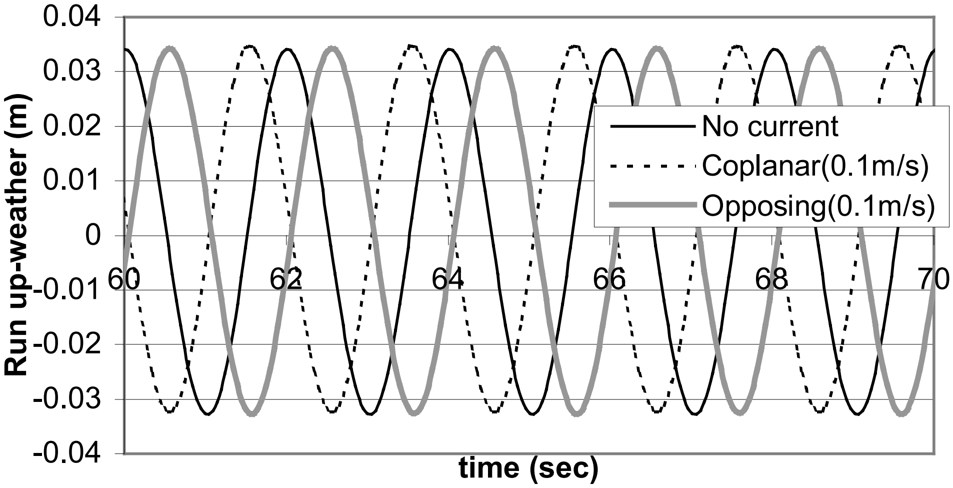

Figure 129. Comparison of run up at weather side.

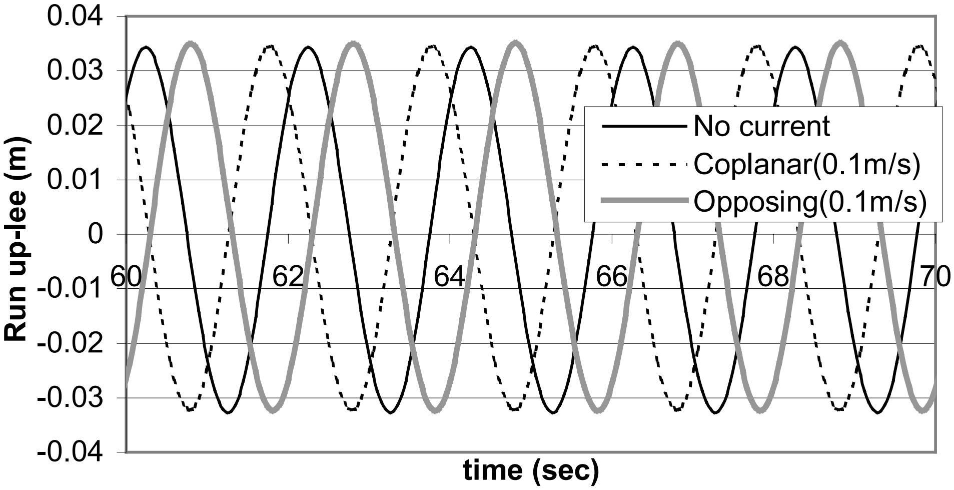

Figure 130. Comparison of run up at lee side.

CHAPTER V

CONCLUSIONS AND RECOMMENDATION

A 2D fully nonlinear Numerical Wave Tank (NWT) is developed based on the potential theory, mixed Eulerian-Lagrangian (MEL) time marching scheme, and boundary element method (BEM). For fully nonlinear time domain simulation, Runge-Kutta4th order (RK4) scheme as a time marching scheme is used. In order to calculate wave force on a floating body, acceleration potential method was used. Nonlinear wave deformation and wave forces on stationary and freely floating bodies are calculated using the NWT.

The wave kinematics of nonlinear NWT simulations are compared with the linear, Stokes second-order theory and experimental values. It is shown that the wave kinematics above mean water level can be significantly different from the perturbation-based prediction. It is also found that small mean positive or negative flows can be generated below mean water level depending on the water depth and wave condition.

For verification, the computed mean, 1st, 2nd, and 3rd order wave forces on a single submerged cylinder are compared with those of Chaplin's experiment, Ogilvie's 2nd-order theory, and another nonlinear computation called high-order spectral method. The noticeable discrepancy on the 1st-order wave forces for higher KC numbers is due to the viscous effect (clockwise circulation around the body), as speculated by Chaplin, which was also confirmed by an independently developed viscous-flow-based NWT.

Similar calculations for dual submerged cylinders with various gaps were also conducted. It is clearly seen that the interaction effects become of critical importance when the gap is small, and their magnitudes can be greatly amplified. This trend is more pronounced for the higher harmonic forces on the rear cylinder. The trend of the amplification of forces on dual submerged cylinders predicted by the present potential-NWT is qualitatively similar to that of the viscous-NWT results when KC=0.5.

The developed fully nonlinear NWT is also applied to the calculations of nonlinear pressure and force of surface piercing barge type structures and the obtained results agree well with experimental and theoretical results. For dual structures, the strength of wave-body interactions is varied depending on wavelength. The maximum interactions are observed when the incoming wavelength is about twice of total body width (front body to rear body). As wavelength comparing to body width decreases (2D Beam sea case), the front structure has been effected more by wave energy than rear structure so that higher order wave forces are pronounced in the front body.

Nonlinear waves generated by prescribed body motions, such as wedge type wave maker or land sliding in the coastal slope area, can also be simulated by the NWT. The generated waves are in good agreement with published experimental and numerical results. Added mass and damping coefficient can also be calculated from the simulation in time domain. It is found that body nonlinear simulation is not good for high frequency prescribed motion simulations because of not accounting for free surface nonlinearity.

For the simulation of freely floating barge-type structure, only fully nonlinear time-stepping scheme can accurately produce nonlinear body motions with large floating body simulations. The acceleration potential method, which was developed by Tanizawa (1996), is known to be the most accurate, consistent and stable. Using acceleration potential method, in the present study, the series of motions and drift forces were calculated over a wide range of incident wave frequencies including resonance region. Severe nonlinear phenomena for surface elevation and forces due to large motions near resonance area were found and investigated.

In order to clearly compare the nonlinear contribution of free-surface and body-boundary conditions, the body-nonlinear-only case with linearized free-surface condition is separately simulated. The drift force from pressure integration for body nonlinear simulation has been observed for negative trends as incident wave steepness increases. 2nd and 3rd harmonic horizontal forces near the resonance are bigger than 1st and mean forces so that the sway motions have parametric behavior. All other fully nonlinear results for motions and force are in good agreement with experimental results.

Finally, the NWT is extended to fully nonlinear wave-body-current interactions of freely floating bodies, which has not been published in the open literature until now. Current effects on the free surface boundary were demonstrated and resulting floating body motions were presented. Higher crest waves can be propagated in case of opposing current, while lower crest waves in case of coplanar case. Riding on coplanar current, the propagating waves have enlarged wavelength, while opposing current can shorten their wavelength.

So far, we have developed the 2D fully nonlinear NWT completely. By using the NWT, there are many valuable applications, which were not considered yet. For instance, multi-body floating structure motions can be simulated in near future. This issue becomes popular because many engineering designs have to be taken into account for multi body situation such as FPSO/FSO. A capsizing barge induced by resonance frequency can also be simulated when minor numerical instability near the body surface is overcome. A 3D fully nonlinear NWT is the final goal of numerical calculations. For complete 3D simulation with fully nonlinear boundary conditions, still there are a lot of numerical problems to be solved. This is the reason for this study to be continued.

REFERENCES

Brebbia, C. & Dominguez, J. 1992 *Boundary elements: an introductory course.* Computatinal Mechanics Publications, Southampton, U.K. McGraw-Hill.

Cao, Y., Beck, R. & Schultz, W. 1994 Nonlinear motions of floating bodies in incident waves. *9th Workshop on Water Waves and Floating Bodies*, *Kuju, Oita*, *Japan*, pp. 33-37.

Chaplin, J. 1984 Nonlinear forces on a horizontal cylinder beneath waves. *J. Fluid Mech.* **147**, 449-464.

Choi, H., Cox, D., Kim, M. & Ryu, S. 2001 Laboratory investigation of nonlinear irregular wave kinematics. *Proc. 4th Int. Symp. on Ocean Wave Measurement and Analysis, WAVES 2001, ASCE, San Francisco, CA,* **2**, 1685-1694.

Cointe, R., Geyer, P., King, B., Molin, B. & Tramoni, M. 1990 Nonlinear and linear motions of a rectangular barge in a perfect fluid. *Proc. 18th Symp. on Naval Hydrodynamics* pp. 85-99.

Contento, G. 1996 Nonlinear phenomena in the motions of unrestrained bodies in a numerical wave tank. *Proc. 6th Int. Offshore and Polar Eng. Conference, ISOPE, Los Angeles*, *CA*, **3**, 18-22.

Ferrant, P. 1998 Run-up on a cylinder due to waves and currents: potential flow solution with fully nonlinear boundary conditions. *Proc. 8th Int. Offshore and Polar Eng. Conference, ISOPE, Montreal*, **3**, 332-339.

Goda, Y. 1998 Perturbation analysis of nonlinear wave interactions in relatively shallow Water. *Proc. 3rd Int. Conf. on Hydrodynamics, Seoul, Korea*, pp. 33-51.

Grill, S. T. & Watts, P. 1999 Modeling of waves generated by a moving submerged body. Applications to underwater landslides. *Engng Analysis Bound. Elem.* **23**, 645-656.

Kashiwagi, M. 1996 Full-nonlinear simulations of hydrodynamic forces on a heaving tow-dimensional body. *J. Soc. Nav. Arch. Japan* **180**, 373-381.

Kashiwagi, M. Momoda, T. & Inada, M. 1998 A time-domain nonlinear simulation method for wave-induced motions of a floating body. *J. Soc. Nav. Arch. Japan* **84**, 143-152.

Kim, C., Clement, A. & Tanizawa, K. 1999 Recent research and development of numerical wave tanks-a review. *Int. J. Offshore and Polar Eng.* **9**, 241-256.

Koo, W. & Kim, M. 2001 Fully nonlinear waves and their kinematics: NWT simulation vs experiment. *Proc. 4th Int. Symp. on Ocean Wave Measurement and Analysis, Waves 2001, ASCE*, *San Francisco*, *CA*, **2**, 1092-1101.

Koo, W. & Kim, M. 2003 Fully nonlinear wave interactions with stationary and moving bodies. *Proc. 13th Int. Offshore and Polar Eng. Conference, ISOPE, Honolulu, HI [CD-ROM].*

Liu, Y., Dommermuth, D. & Yue, D. K. P. 1992 A high-order spectral method for nonlinear wave-body interactions. *J. Fluid Mech.* **245**, 115-136.

Longuet-Higgins, M., & Cokelet, E. D. 1976 The deformation of steep surface waves on water: I. a numerical method of computation. *Proc. R. Soc. Lond.* **A 350**, 1-26.

Lynett, P. & Liu, P. L.-P. 2002 A numerical study of submarine-landslide-generated waves and run-up. *Proc. R. Soc. Lond.* **A 458**, 2885-2910.

Maruo, H. 1960 On the increase of the resistance of a ship in rough seas. *J. Zosen Kiokai*, **108**.

Mei, C. C. 1994 The applied dynamics of ocean surface waves. *World Scientific*, *Singapore*, **1**, 365.

Nojiri, N. & Murayama, K. 1975 A study on the drift force on two-dimensional floating body in regular waves. *Trans. West-Japan Soc. Nav. Arch.* **51,** 131-152.

Ogilvie, T. F. 1963 First- and second-order forces on a cylinder submerged under a free Surface. *J. Fluid Mech.* **16**, 451-472.

Sen, D 1993 Numerical simulation of motions of two-dimensional floating bodies. *J. Ship Research* **37,** 4, 307-330.

Sung, H. G. 1999 A Numerical Analysis of Nonlinear Diffraction Problem in Three Dimensions by Using Higher-Order Boundary Element Method. Ph.D. thesis, Seoul National University.

Tanizawa, K. 1995 A nonlinear simulation method of 3-D body motions in waves (1st Report). *J. Soc. Nav. Arch. Japan*, **178**, 179-191.

Tanizawa, K. 1996 Nonlinear simulation of floating body motions. *Proc. 6th Int. Offshore and Polar Eng. Conference, ISOPE, Los Angeles*, *CA*, **3**, 414-420.

Tanizawa, K. & Clement, A. H. 1999 Benchmark test cases of radiation problem. *2nd Workshop of ISOPE Numerical Wave Tank Group, Brest, France*.

Tanizawa, K. & Minami, M. 1998 On the accuracy of NWT for radiation and diffraction problem. *Abstact for the 6th Symp. on Nonlinear and Free-surface Flow.*

Tanizawa, K. & Naito, S. 1997 A study on parametric roll motions by fully nonlinear numerical wave tank. *Proc. 7th Int. Offshore and Polar Eng. Conference*, *ISOPE, Honolulu*, *HI,* **3**, 69-75.

Tanizawa, K. & Sawada, H. 1990 A numerical method for nonlinear simulation of 2-D body motions in waves by means of BEM. *J. Soc. Nav. Arch. Japan* **168**, 223-228.

Tavassoli, A. & Kim, M. H. 2001 Interactions of fully nonlinear waves with submerged bodies by a 2D viscous NWT. *Proc. 11th Int. Offshore and Polar Eng. Conference*, *ISOPE*, *Stavanger*, *Norway,* **3**, 348-354.

Vinji, T. & Brevig, P. 1981 Numerical simulation of breaking wave. *Proc. 3rd Int. Conf. Finite Elemnts in Water Resources,* University of Mississippi, Oxford, **5**, 196-210.

Watts, P. 1997 Water waves generated by underwater landslides. Ph.D. thesis, California Institute of Technology.

Wu, G. & Eatock Taylor, R. 1996 Transient motion of a floating body in steep water waves. *Proc. 11th Int. Workshop on Water and floating Bodies*, *Hamburg, Germany*.

APPENDIX A

Runge-Kutta-Nystrom 4th order scheme

$$
\begin{aligned}
&y'' = f(x, y, y') \\
&k_1 = \frac{1}{2} h f(x_n, y_n, y'_n) \\
&k_2 = \frac{1}{2} h f(x_n + \frac{1}{2} h, y_n + K, y'_n + k_1) \\
&k_3 = \frac{1}{2} h f(x_n + \frac{1}{2} h, y_n + K, y'_n + k_2) \\
&k_4 = \frac{1}{2} h f(x_n + h, y_n + L, y'_n + 2k_3) \\
&where,\ K = \frac{1}{2} h(y'_n + \frac{1}{2} k_1) \text{ and } L = h(y'_n + k_3)
\end{aligned}
\tag{A.1}
$$

$$
\begin{aligned}
&x_{n+1} = x_n + h \\
&y_{n+1} = y_n + h(y'_n + \frac{1}{3}(k_1 + k_2 + k_3)) \\
&y'_{n+1} = y'_n + \frac{1}{3}(k_1 + 2k_2 + 2k_3 + k_4)
\end{aligned}
\tag{A.2}
$$

APPENDIX B

Application to time domain floating body simulation

$$
\begin{aligned}
x'' &= (F - Cx)/m \\
k_1 &= \frac{1}{2}\Delta t(F_1(t_0) - Cx)/m \\
k_2 &= \frac{1}{2}\Delta t\left(F_2(t_0 + \frac{\Delta t}{2}) - C(x+K) \right)/m \\
k_3 &= \frac{1}{2}\Delta t\left(F_3(t_0 + \frac{\Delta t}{2}) - C(x+K) \right)/m \\
k_4 &= \frac{1}{2}\Delta t\left(F_4(t_0 + \Delta t) - C(x+L) \right)/m
\end{aligned}
\tag{B.1}
$$

where, C is spring constant for additional stiffness, m is body mass

$K = \frac{1}{2}\Delta t(x' + \frac{1}{2}k_1)$ and $L = \Delta t(x' + k_3)$

$$
\begin{aligned}
x_{n+1} &= x_n + \Delta t(x'_n + \frac{1}{3}(k_1 + k_2 + k_3)) \\
x'_{n+1} &= x'_n + \frac{1}{3}(k_1 + 2k_2 + 2k_3 + k_4)
\end{aligned}
\tag{B.2}
$$

$$
F_2 \text{ from } \begin{cases} \text{IWBC} & \dfrac{\partial \phi}{\partial \text{n}}\left(\text{t=t}_0 + \dfrac{\Delta t}{2} \right) \\ \text{FSBC} & x = x_0 + \dfrac{1}{2}\Delta t \phi_{\text{x}},\ y{=}y_0 + \dfrac{1}{2}\Delta t \phi_{\text{z}} \\ \text{BBC} & (\upsilon + k_1)\cdot n \end{cases}
\tag{B.3}
$$

$$F_3 \text{ from } \begin{cases} \text{IWBC} & \dfrac{\partial \phi}{\partial \text{n}}\left(\text{t=t}_0 + \dfrac{\Delta t}{2}\right) \\ \text{FSBC} & x = x_0 + \dfrac{1}{2}\Delta t \phi_{\text{x}},\ y\text{=}y_0 + \dfrac{1}{2}\Delta t \phi_{\text{z}} \\ \text{BBC} & (\upsilon + k_2)\cdot n \end{cases} \quad \text{(B.4)}$$

$$F_4 \text{ from } \begin{cases} \text{IWBC} & \dfrac{\partial \phi}{\partial \text{n}}\left(\text{t=t}_0 + \Delta t\right) \\ \text{FSBC} & x = x_0 + \Delta t \phi_{\text{x}},\ y\text{=}y_0 + \Delta t \phi_{\text{z}} \\ \text{BBC} & (\upsilon + 2k_3)\cdot n \end{cases} \quad \text{(B.5)}$$

where,

IWBC : Input Wave Boundary Condition

FSBC : Free Surface Boundary Condition

BBC : Body Boundary Condition

APPENDIX C

Chebyshev 5-pts. smoothing scheme

$\bar{f}_j = a_0$

where, $\bar{f}_j$ is the value along the smoothed curve at jth node

$$
\begin{aligned}
a_0 = {} & \frac{-\Delta x_{j-1}\Delta x_{j+1}}{2\Delta x_{j-2}(\Delta x_{j+2}-\Delta x_{j-2})} f_{j-2} + \frac{-\Delta x_{j+1}}{2(\Delta x_{j-1}-\Delta x_{j+1})} f_{j-1} + \left(\frac{\Delta x_{j-1}\Delta x_{j+1}}{2\Delta x_{j-2}\Delta x_{j+2}} + \frac{1}{2}\right) f_j \\
& + \frac{\Delta x_{j-1}}{2(\Delta x_{j-1}-\Delta x_{j+1})} f_{j+1} + \frac{\Delta x_{j-1}\Delta x_{j+1}}{2\Delta x_{j+2}(\Delta x_{j+2}-\Delta x_{j-2})} f_{j+2}
\end{aligned}
$$

$$
\begin{aligned}
a_1 = {} & \frac{\Delta x_{j+2}+\Delta x_{j+1}+\Delta x_{j-1}}{2\Delta x_{j-2}(\Delta x_{j+2}-\Delta x_{j-2})} f_{j-2} + \frac{-1}{2(\Delta x_{j+1}-\Delta x_{j-1})} f_{j-1} - \frac{\Delta x_{j-2}+\Delta x_{j-1}+\Delta x_{j+1}+\Delta x_{j+2}}{2\Delta x_{j-2}\Delta x_{j+2}} f_j \\
& + \frac{1}{2(\Delta x_{j+1}-\Delta x_{j-1})} f_{j+1} - \frac{\Delta x_{j+1}+\Delta x_{j-1}+\Delta x_{j-2}}{2\Delta x_{j+2}(\Delta x_{j+2}-\Delta x_{j-2})} f_{j+2}
\end{aligned}
$$

$$
a_2 = \frac{-1}{\Delta x_{j-2}(\Delta x_{j+2}-\Delta x_{j-2})} f_{j-2} + \frac{1}{\Delta x_{j-2}\Delta x_{j+2}} f_j + \frac{1}{\Delta x_{j+2}(\Delta x_{j+2}-\Delta x_{j-2})} f_{j+2}
$$

where, f_j is the value at jth node before smoothing

$$\Delta x_{j-2} = x_{j-2} - x_j$$

$$\Delta x_{j-1} = x_{j-1} - x_j$$

$$\Delta x_{j+1} = x_{j+1} - x_j$$

$$\Delta x_{j+2} = x_{j+2} - x_j$$

At the end point,

$$\bar{f}_0 = a_0 + a_1\Delta x_0 + a_2\Delta x_0^2$$

$$\bar{f}_1 = a_0 + a_1\Delta x_1 + a_2\Delta x_1^2 \quad (\Delta x_k = x_k - x_2)$$

$$\bar{f}_{N-1} = a_0 + a_1\Delta x_{N-1} + a_2\Delta x_{N-1}^2$$

$$\bar{f}_N = a_0 + a_1\Delta x_N + a_2\Delta x_N^2 \quad (\Delta x_k = x_k - x_{N-2})$$

VITA

Weoncheol Koo, son of Tea-Seo Koo, was born on November 7, 1969, in Kun-San, Chun-Buk, South Korea. He graduated from Seoul National University with a Bachelor of Science degree in Oceanography in February 1996. In August 1997, he started his graduate study in the ocean engineering program at Texas A&M University and received a Master of Science degree in May 1999 and a Ph.D in August 2003. He married Dawoon Jung in January 1997 and has a son Samuel (Chang-hyun) and a daughter Lydia (Ja-hyun).

His electronic mailing address is:

kwc@tamu.edu

kwc1969@yahoo.com

and his permanent address is:

290-6 Dongsehak-Dong Kersan Apt.101-1302, Chon-Ju, Chun-Buk, S. Korea.